

# Overview: On the transport and transformation of pollutants in the outflow of major population centres - observational data from the EMeRGe European intensive operational period in summer 2017

M. Dolores Andrés Hernández<sup>1</sup>, Andreas Hilboll<sup>2,†</sup>, Helmut Ziereis<sup>3</sup>, Eric Förster<sup>4</sup>, Ovid O. Krüger<sup>5</sup>, Katharina Kaiser<sup>6,7</sup>, Johannes Schneider<sup>7</sup>, Francesca Barnaba<sup>8</sup>, Mihalis Vrekoussis<sup>2,18</sup>, Jörg Schmidt<sup>9</sup>, Heidi Huntrieser<sup>3</sup>, Anne-Marlene Blechschmidt<sup>1</sup>, Midhun George<sup>1</sup>, Vladyslav Nenakhov<sup>1,\*</sup>, Theresa Harlass<sup>3</sup>, Bruna A. Holanda<sup>5</sup>, Jennifer Wolf<sup>3</sup>, Lisa Eirenschmalz<sup>3</sup>, Marc Krebsbach<sup>10</sup>, Mira L. Pöhlker<sup>5,\*\*</sup>, Anna Beata K. Hedegaard<sup>3,2</sup>, Linlu Mei<sup>1</sup>, Klaus Pfeilsticker<sup>11</sup>, Yangzhuoran Liu<sup>1</sup>, Ralf Koppmann<sup>10</sup>, Hans Schlager<sup>3</sup>, Birger Bohn<sup>12</sup>, Ulrich Schumann<sup>3</sup>, Andreas Richter<sup>1</sup>, Benjamin Schreiner<sup>11</sup>, Daniel Sauer<sup>3</sup>, Robert Baumann<sup>3</sup>, Mariano Mertens<sup>3</sup>, Patrick Jöckel<sup>3</sup>, Markus Kilian<sup>3</sup>, Greta Stratmann<sup>3,\*\*\*</sup>, Christopher Pöhlker<sup>5</sup>, Monica Campanelli<sup>8</sup>, Marco Pandolfi<sup>13</sup>, Michael Sicard<sup>14,15</sup>, José L. Gómez-Amo<sup>16</sup>, Manuel Pujadas<sup>17</sup>, Katja Bigge<sup>11</sup>, Flora Kluge<sup>11</sup>, Anja Schwarz<sup>9</sup>, Nikos Daskalakis<sup>2</sup>, David Walter<sup>5</sup>, Andreas Zahn<sup>4</sup>, Ulrich Pöschl<sup>5</sup>, Harald Bönisch<sup>4</sup>, Stephan Borrmann<sup>6,7</sup>, Ulrich Platt<sup>11</sup>, and John Phillip Burrows<sup>1</sup>.

<sup>1</sup>Institute of Environmental Physics, University of Bremen, Bremen, Germany

<sup>2</sup>Laboratory for Modeling and Observation of the Earth System, Institute of Environmental Physics, Bremen, Germany.

<sup>3</sup>Deutsches Zentrum für Luft- und Raumfahrt (DLR), Institut für Physik der Atmosphäre, Oberpfaffenhofen, Germany

<sup>4</sup>Karlsruhe Institute of Technology, Institute of Meteorology and Climate Research, Karlsruhe, Germany

<sup>5</sup>Multiphase Chemistry Department, Max Planck Institute for Chemistry, Mainz, Germany

<sup>6</sup>Institute for Atmospheric Physics, Johannes Gutenberg University, Mainz, Germany

<sup>7</sup>Particle Chemistry Department, Max Planck Institute for Chemistry, Mainz, Germany

<sup>8</sup>National Research Council of Italy, Institute of Atmospheric Sciences and Climate (CNR-ISAC), Roma, Italy

<sup>9</sup>Leipzig Institute for Meteorology, Leipzig University, Leipzig, Germany

<sup>10</sup>Institute for Atmospheric and Environmental Research, University of Wuppertal, Wuppertal, Germany

<sup>11</sup>Institute for Environmental Physics, University of Heidelberg, Heidelberg, Germany

<sup>12</sup>Institute of Energy and Climate Research IEK-8, Forschungszentrum Jülich, Jülich, Germany

<sup>13</sup>Institute of Environmental Assessment and Water Research, Barcelona, Spain

<sup>14</sup>CommSensLab, Dept. of Signal Theory and Communications, Universitat Politècnica de Catalunya, Barcelona, Spain

<sup>15</sup>Ciències i Tecnologies de l'Espai-Centre de Recerca de l'Aeronàutica i de l'Espai/Institut d'Estudis Espacials de Catalunya), Universitat Politècnica de Catalunya Barcelona, Spain

<sup>16</sup>Dept. Earth Physics and Thermodynamics, University of Valencia, Burjassot, Spain

<sup>17</sup>Centro de Investigaciones Energéticas, Medioambientales y Tecnológicas (CIEMAT), Madrid, Spain

<sup>18</sup>Climate and Atmosphere Research Center (CARE-C), The Cyprus Institute, Nicosia, Cyprus

\*now at Flight Experiments, Deutsches Zentrum für Luft- und Raumfahrt (DLR), Oberpfaffenhofen, Germany

\*\* now at Faculty of Physics and Earth Sciences, Leipzig Institute for Meteorology, University of Leipzig/

Experimental Aerosol and Cloud Microphysics Department, Leibniz Institute for Tropospheric Research, Leipzig, Germany

\*\*\*now at Deutsches Elektronen-Synchrotron DESY, Notkestr. 85, 22607 Hamburg, Germany

† deceased

Correspondence to: M.D. Andrés Hernández (lola@iup.physik.uni-bremen.de)

**Abstract.** Megacities and other major population centers (MPCs) worldwide are major sources of air pollution, both locally as well as downwind. The overall assessment and prediction of the impact of MPC pollution on tropospheric chemistry are challenging. The present work provides an overview of the highlights of a major new contribution to the understanding of this issue based on the data and analysis of the EMeRGe (Effect of

**M**egacities on the transport and transformation of pollutants on the **R**egional to **G**lobal scales) international project. EMeRGe focuses on atmospheric chemistry, dynamics and transport of local and regional pollution originating in MPCs. Airborne measurements, taking advantage of the long range capabilities of the High altitude and long range research aircraft (HALO, [www.halo-spp.de](http://www.halo-spp.de)), are a central part of the project. The synergistic use and consistent interpretation of observational data sets of different spatial and temporal resolution (e.g. from ground-based networks, airborne campaigns, and satellite measurements) supported by modelling within EMeRGe, provides a unique insight to test the current understanding of MPC pollution outflows.

In order to provide an adequate set of measurements at different spatial scales, two field experiments were positioned in time and space to contrast situations when the photochemical transformation of plumes emerging from MPCs is large. These experiments were conducted in summer 2017 over Europe and in the inter-monsoon period over Asia in spring 2018. The intensive observational periods (IOP) involved HALO airborne measurements of ozone and its precursors, volatile organic compounds, aerosol particles and related species as well as coordinated ground-based ancillary observations at different sites. Perfluorocarbon (PFC) tracer releases and model forecasts supported the flight planning, the identification of pollution plumes, and the analysis of chemical transformations during transport.

This paper describes the experimental deployment and scientific questions of the IOP in Europe. The MPC targets London (Great Britain), Benelux/Ruhr area (Belgium, The Netherlands, Luxembourg and Germany), Paris (France), Rome and Po Valley (Italy), Madrid and Barcelona (Spain) were investigated during 7 HALO research flights with aircraft base in Germany for a total of 53 flight hours. An in-flight comparison of HALO with the collaborating UK-airborne platform FAAM took place to assure accuracy and comparability of the instrumentation on-board.

Overall, EMeRGe unites measurements of near- and far-field emissions, and hence deals with complex air masses of local and distant sources. Regional transport of several European MPC outflows was successfully identified and measured. Chemical processing of the MPC emissions was inferred from airborne observations of primary and secondary pollutants and the ratios between species having different chemical lifetimes. Photochemical processing of aerosol and secondary formation of organic acids was evident during the transport of MPC plumes. Urban plumes mix efficiently with natural sources as mineral dust and with biomass burning emissions from vegetation and forest fires. This confirms the importance of wildland fire emissions in Europe and indicates an important but discontinuous contribution to the European emission budget that might be of relevance in the design of efficient mitigation strategies.

The present work provides an overview of the most salient results in the European context, these being addressed in more detail within additional dedicated EMeRGe studies. The deployment and results obtained in Asia will be the subject of separate publications.

## **1 Introduction**

In recent decades, the number and size of major population centres (MPCs) have increased dramatically. The term MPC describes a single metropolitan area or converging urban conurbations with a population exceeding 10 million inhabitants. In 1950, New York and Tokyo were the only two megacities in the world (Gardi, 2017) whereas for 2018 the United Nations reported 33 megacities and 48 urban agglomerations of 5 to 10 million

inhabitants (UN, 2019). One cause of the recent growth of the number of MPCs is the rapid industrialisation of some parts of the world, in particular East Asia.

The economic consequences of urbanisation, the spatial growth of MPCs, and, in particular, the environmental and economical sustainability of megacities, have been a focus of recent discussion (ESPAS, 2018; Melchiorri et al., 2018; Hoole et al., 2019; Odendahl et al., 2019). The MPC has occasionally been presented as a favourable urban model because the concentration of resources and services and the development of more effective mitigation strategies make it potentially less harmful for the environment than other more dispersed population distributions (Grimm, 2008; Dodman, 2009). Nevertheless, the agglomeration of emissions from fossil fuel combustion for transport, industrial and domestic purposes, makes MPCs a growing and globally significant emission source of trace gases and aerosol particles for the troposphere. The current knowledge on local and regional impacts of MPC pollution outflows is still limited. Decoupling the pollutant input upwind from the MPC emissions remains essential to establish accurate source-receptor relationships and effective control and mitigation policies.

The EMeRGe (Effect of Megacities on the transport and transformation of pollutants on the Regional to Global scales) project has as an overarching objective the improvement of the current understanding of photochemical and heterogeneous processing of MPC plumes along expected transport pathways. EMeRGe began in 2016 in the framework of the Priority Program of the German Research Foundation (DFG: Deutsche Forschungsgemeinschaft, [www.halo-spp.de](http://www.halo-spp.de)) to exploit the High Altitude and Long range research aircraft (HALO) for atmospheric science.

EMeRGe has a focus on airborne measurements and fostered cooperation with an international research partnership (hereinafter referred to as EMeRGe international) to facilitate the delivery and comprehensive analysis of a unique set of data from aircraft-, ground- and satellite-based sensors. The institutions currently involved in EMeRGe and EMeRGe international are listed in the supplementary information (see S1 and S2).

Europe and Asia are regions of the world with a differing heritage of pollution control strategies and notable differences in the number, size and proximity of MPCs as well as in the nature of emissions. For this reason, two field experiments were designed in EMeRGe to investigate the transport and transformation processes of pollution plumes originating from European and Asian MPCs. The first intensive observational period (IOP) was carried out in Europe from 10 to 28 July 2017 with special focus on the study of active plume processing close to emission sources. The second IOP aimed at the investigation of long-range transport (LRT) of MPC outflows from the Asian continent to the Pacific during the spring inter-monsoon period and took place with HALO base in Taiwan from 10 March to 9 April 2018.

The present article describes the experimental design and specific objectives of the IOP of EMeRGe in Europe. It highlights key research questions and some of the scientific results, which are further explored in dedicated publications.

## 2 Background

High levels of urbanisation are associated with severe air pollution events which lead to adverse effects on human health (Lelieveld et al., 2015, 2020). The effects of pollution originating from MPCs and the development of adequate control strategies are receiving growing attention as the public concern about air quality and the interaction of pollution and climate on a warming planet increases (e.g., Jacob and Winner,

2009). In that respect, the MPC emissions of environmental interest are aerosol particles, which contain sulphate ( $\text{SO}_4^{2-}$ ) and nitrate ( $\text{NO}_3^-$ ), particulate organic matter (POM), black carbon (BC), and ammonium ( $\text{NH}_4^+$ ), carbon monoxide (CO) and long-lived greenhouse gases (GHG) such as carbon dioxide ( $\text{CO}_2$ ) and methane ( $\text{CH}_4$ ). The net radiative effect of the aerosol particles largely depends on the size and chemical composition which determine their scattering and absorption capabilities (e.g., Haywood and Boucher, 2000). As cloud condensation nuclei (CCN) they have an additional effect on the optical properties and lifetime of clouds (e.g. Andreae and Rosenfeld, 2008; Campos Braga et al., 2017; Rosenfeld et al., 2008). Short-lived constituents of smog, such as nitrogen oxides ( $\text{NO}_x$ , i.e., NO and  $\text{NO}_2$ ), volatile organic compounds (VOC), and sulphur dioxide ( $\text{SO}_2$ ), react to produce ozone ( $\text{O}_3$ ) and secondary aerosol particles and also have a climatic effect (UNEP, 2011; Mar, 2021).

Primary MPC emissions are transported and transformed into secondary pollutants such as  $\text{O}_3$  or secondary aerosols (organic and inorganic) and lead to smog episodes downwind of the source. Modelling studies using artificial aerosol tracers and estimations of deposition potentials, indicate that about 50% of MPC emitted particles with diameter  $\leq 2.5 \mu\text{m}$  ( $\text{PM}_{2.5}$ ) deposit more than 1000 km from their source (Kunkel et al., 2012). Chemical and physical processing of MPC emitted pollutants can in turn be affected by mixing with natural, biogenic and other anthropogenic emissions from regional sources or long-range transported from other areas (Lawrence et al., 2007, Monks et al., 2009, Lawrence and Lelieveld, 2010, and references therein).

The specific impact of the plumes from MPCs, therefore, depends not only on the type of emission sources (e.g. industry, transportation, domestic heating, and generation of electricity) but also on the variability of trace constituent emissions, the local meteorology and topography. Modelling studies indicate significant latitudinal differences in regional to hemispheric dispersion characteristics (Lawrence et al., 2007 and references therein; Cassiani et al., 2013). Transport and transformation of MPC outflows are affected by the general weather patterns such as frontal passages and the frequency and duration of stagnation episodes, which are important for pollutant ventilation. In the last decades, improved monitoring and modelling capabilities and a growing number of measurements campaigns have provided essential information about the impact of MPC pollution on the atmospheric composition (see review by Zhu et al., 2012). However, capturing the combined influence of emissions, chemistry and dynamics for specific locations is still a big challenge. In particular, inconsistencies in local and regional MPC inventories (e.g. Denier van der Gon et al.; 2011, Mayer et al., 2000; Butler and Lawrence, 2009), and limitations in the prediction capabilities of pollution transport patterns and cumulative pollution events in downwind regions of MPCs (Zhang et al., 2007; Kunkel et al., 2012) require ongoing attention. Furthermore, controlling policies, changes in land cover and climate continue to evolve and ~~is~~are expected to substantially modify the relation between anthropogenic emissions and both natural aerosol and trace gases, as predicted by e.g., Butler et al., (2012), and recently reported for East Asia (Fu et al., 2016; Silver et al., 2018 and references herein; Leung et al., 2018).

In Europe, the level of urbanisation is presently ~ 74% and is expected to further increase by 10% up to the middle of this century (UN, 2019). Large urban conurbations are more abundant in Europe than megacities, of which there are a few. According to the European Environment Agency (EEA), the emission of air pollutants and precursors has decreased across Europe from the year 2000 to the present, partly as a result of the EU air quality legislation. Emissions of CO, BC,  $\text{NO}_x$  and non-methane VOCs have been reduced by around 30% and those of sulphur oxide ( $\text{SO}_x$ , primarily  $\text{SO}_2$ ) up to 77%. Nevertheless, the daily and annual  $\text{O}_3$  and PM limit concentrations for protection of human health are often exceeded in several areas of the continent (EEA, 2019).

Significant differences in pollution and photochemical episodes between Northern and Central Europe and the Mediterranean region are regularly observed, in particular due to the differences in solar actinic radiation (Kanakidou et al., 2011).

European air quality is frequently influenced by LRT of North American pollution as captured by airborne measurements and investigated in several model studies (e.g. Stohl et al., 2003; Huntrieser and Schlager, 2004; Huntrieser et al., 2005). Some evidence of LRT of Asian pollution to the Mediterranean has also been documented (Lawrence and Lelieveld, 2010; Lelieveld et al., 2002). The chemical signatures of LRT of pollutants vary depending on pollutant lifetime and mixing. Some recent modelling studies infer that the impact of non-European pollution on the European surface O<sub>3</sub> annual average is larger than previously expected (Jonson et al., 2018).

In recent years, large European projects such as MEGAPOLI (<http://megapoli.dmi.dk>) and CityZen (Megacity-Zoom for the Environment; <http://www.cityzen-project.eu>), provided comprehensive theoretical and experimental data about MPCs in Europe. The MEGAPOLI field campaign was conducted in Paris in summer 2009 and winter 2010 (Beekmann et al., 2015) and investigated source apportionment and photochemical processing of emitted gaseous and particulate substances using several ground-based stations and measurement vehicles (Crippa et al., 2013; Freutel et al., 2013; von der Weiden-Reinmüller et al., 2014). Beekmann et al., (2015) estimated the impact of the urban emissions from the Paris megacity to be relatively low in comparison to other external industrial sources of pollution. Aircraft measurements were restricted to the near-field outflow (up to 200 km) in the boundary layer below 700 m asl (Brands et al., 2011; Freney et al., 2014). In comparison, EMerge focuses on the impact of different MPCs in Central and Southern Europe and investigates atmospheric pollution plumes over much larger geographical extent.

CityZen (2008-2011) studied air pollution in and around selected megacities and emission hotspots by using in-situ and satellite observations (Hilboll et al., 2013; Vrekoussis et al., 2013) as well as a series of different scale models (Colette et al., 2011; Im et al., 2012). The project focused on selected MPCs such as the Eastern Mediterranean, the Po Valley, the Benelux region, and the Pearl River Delta for intensive case studies but, in contrast to EMerge, did not conduct measurements of the photochemical evolution in the outflow of the studied regions.

The above studies focused on trace gases linked to air quality and provided relatively sparse information on GHGs. Long-lived greenhouse gases such as CH<sub>4</sub> and CO<sub>2</sub> emitted from individual European urban areas have been investigated in airborne and ground-based studies, e.g. for London (O'Shea et al., 2014; Helfter et al., 2016; Pitt et al., 2019), Paris (Bréon et al., 2015; Lian et al., 2019), Cracow (Kuc et al., 2003; Zimnoch et al., 2019), Berlin (Klausner et al., 2020) and Rome (Gioli et al., 2014). Collectively, they report on inconsistencies between the current emission inventories and measurements. This indicates the need for further experimental investigation of the GHG budget in Europe.

Overall, the proximity of most European MPCs results in the mixing of different pollution plumes during their transport. This hampers the identification of the air mass origin. The impact of biomass burning (BB) and mineral dust events on the total European burden of atmospheric aerosol and trace gases is, moreover, variable. Particularly in Southern Europe, BB and mineral dust plumes occur frequently and can significantly affect the chemical processing of MPC pollution plumes. BB events from agriculture or wildland fires have a strong seasonal pattern and related impacts in Europe (Barnaba et al., 2011). Wildfires emit similar to MPC large amounts of pollutants, e.g. PM, NO<sub>x</sub>, CO, VOC and PAH (Andreae, 2019). The number and severity of wildfires

are expected to increase in Europe under warmer and drier conditions as a co-effect of climate change (Forzieri et al., 2017; Guerreiro et al., 2018; Turco et al., 2018). Desert dust episodes of different intensity originating in North Africa frequently affect air mass composition and atmospheric stratification over the Mediterranean particularly in spring and summer (e.g. Barnaba and Gobbi, 2004; Kalivitis et al., 2007; Gkikas et al., 2013; Pey et al., 2013; Pikridas et al., 2018).

### 3 Specific scientific questions and characteristics of the EMeRGe IOP in Europe

#### 3.1 Specific scientific questions

EMeRGe in Europe focuses on three primary scientific goals addressing a series of related specific questions:

##### I. Identification of emission signatures in MPC plumes over Europe

- Are there individual MPC emission signatures identifiable in pollution plumes measured over Europe?
- Is it possible to unambiguously identify MPC plumes after transport times of hours or days by tagging the air masses in the source regions with passive tracers released at the surface and using airborne sensors downwind?
- Can the effect of plumes from different emission sources (e.g., anthropogenic, BB, and/or a mixture of them) on the oxidation potential of the atmosphere be inferred from changes in the NO/NO<sub>y</sub> and NO/VOC ratios in airborne measurements?
- Can airborne measurements detect signatures of urban and other emission sources of CH<sub>4</sub> in Europe adequately?
- How abundant are organic acids in European MPC plumes relative to inorganic acids and what are their main sources?
- Are satellite measurements of aerosol and trace gases capable of supporting the identification of MPC plumes and dominant transport paths?

##### II. Investigation and assessment of chemical processing in MPC pollution outflows

- Is the photochemical activity of MPC plumes readily related to changes in concentrations of radicals and their precursors measured by the HALO sensors?
- Is the photochemical ageing of MPC plumes well described by the chemical clocks inferred from the airborne measurements of trace gases and aerosol particles?
- Can the O<sub>3</sub> production efficiency and NO<sub>x</sub>-and VOC-sensitive regimes in MPC plumes be determined? How do these change with respect to the plume age and mixing with background air?
- Can the importance of the role of formaldehyde (HCHO) as an intermediate product in the oxidation of VOCs, and glyoxal (C<sub>2</sub>H<sub>2</sub>O<sub>2</sub>) and methylglyoxal (C<sub>3</sub>H<sub>4</sub>O<sub>2</sub>) in secondary aerosol formation be inferred from their airborne measurement in MPC pollution plumes?
- Which processes control the heterogeneous formation of HONO in polluted air masses of MPC origin in the BL and lower troposphere over Europe?

##### III. Assessment of the relative importance of MPCs as sources of pollution over Europe

- How important are BB and dust emissions to MPC plume photochemistry over Europe in the summer 2017?
- How do the regional CH<sub>4</sub> urban emission distributions in Europe compare with previous observations in the same areas?

- Is it possible to assess the relative role of primary and secondary pollutants in the proximity and in the outflow of MPCs?
- Are state-of-the-art chemical models capable of adequately simulating transport and transformation of European MPC outflows?

### 3.2 Selection of MPC targets and measurement strategy

The dominant source of  $\text{NO}_x$  and CO in the planetary boundary layer (PBL) in Europe is anthropogenic activity, primarily fossil fuel combustion and BB. Cloud free monthly average tropospheric composites of  $\text{NO}_2$  columns retrieved from GOME2-B and OMI instruments on-board the MetOp-B and Aura satellites were used to identify the major MPCs in Europe during July in the EMerGe study. Due to its short lifetime,  $\text{NO}_2$  is a good indicator of the origin of emission sources. The tropospheric  $\text{NO}_2$  columns retrieved in July 2016 during the campaign preparation showed enhanced  $\text{NO}_2$  concentrations over the megacities London, Moscow and Paris, over large urban agglomerations such as the Benelux/Ruhr metropolitan area in Central Europe and the Po Valley in Northern Italy, and over the conurbations in Southern Europe such as Rome, Naples, Madrid and Barcelona. The satellite observations during the EMerGe IOP in 2017 confirmed the  $\text{NO}_2$  hot spots identified (Fig. 1).

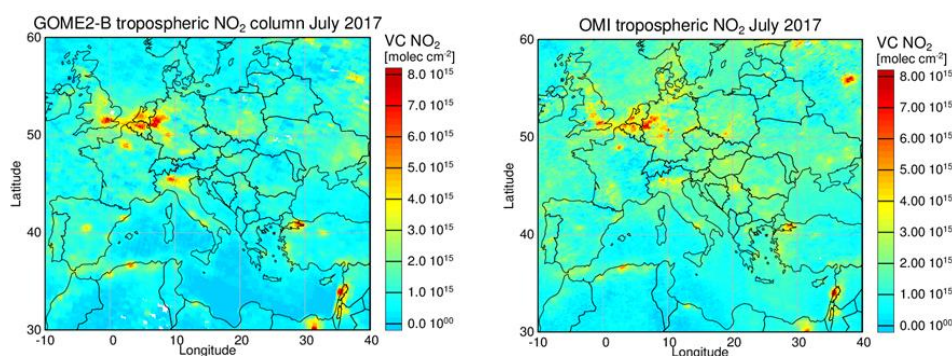


**Figure 1:** Satellite tropospheric  $\text{NO}_2$  columns retrieved from GOME2-B (left panel, overpass at 9:30 h local time), and OMI (right panel, overpass at 13:45 h local time) instruments for the IOP period in July 2017.

CO was used in dispersion calculations to identify anthropogenic pollution from combustion. CO is a suitable tracer for transport pathways due to its relatively long atmospheric lifetime which is primarily determined by the reaction with the OH radical and varies between a few weeks and a few months. To address the EMerGe scientific objectives, the day-to-day flight planning focused on the identification of the location of the plumes from the targeted MPC outflows during potential flights. For this, the following forecast tools were exploited:

- ECMWF (European Centre for Medium-Range Weather Forecasts, <https://www.ecmwf.int/>) and NCEP (National Center for Environmental Prediction, <https://www.ncep.noaa.gov/>) weather forecasts,
- NOAA (National Oceanic and Atmospheric Association) HYSPLIT (Hybrid Single Particle Lagrangian Integrated Trajectories, <https://www.arl.noaa.gov/hysplit/>) model for forward dispersion calculations using CO as a tracer of pollution. These forecasts, carried out by DLR (Deutsches Zentrum für Luft- und Raumfahrt), assume MPCs to be continuous emission sources and provide snap shots as well as horizontal and vertical cross sections of the selected outflows at certain times.

Formatiert: Schriftart:

Formatiert: Ebene 2, Nicht vom nächsten Absatz trennen, Diesen Absatz zusammenhalten

Formatiert: Schriftart:

iii) Tailor-made CO and stratospheric ozone tracer simulations provided by CAMS (Copernicus Atmosphere Monitoring Service, <http://atmosphere.copernicus.eu>) through its field campaign support (see also Flemming et al., 2019).

A list of model simulations and satellite observations used for flight planning is given in Tables 1a and 1b. These are described in more detail in the supplement (see S3). The dedicated mission support tool (MSS, Mission Support System; Rautenhaus et al., 2012) provided additional assistance in the flight planning.

**Table 1a:** Model simulations used for flight planning during EMeRGe in Europe

Name	Type	Resolution of model output	Institution
CAMS-global (CIFS-TM5)	CTM	0.4° x 0.4°; 60 vertical levels	ECMWF
CAMS-regional ensemble	Median of 7 regional CTMs	0.1° x 0.1°; surface, 50, 250, 500, 1000, 2000, 3000, 5000 km	ECMWF
EMEP	regional CTM	0.25° E x 0.125° N; 20 vertical levels	Norwegian Meteorological Institute
HYSPLIT	Lagrangian trajectory model	0.1° x 0.1°; 20 vertical levels	NOAA/DLR
FLEXPART	Lagrangian trajectory model	1min /10 days back ECMWF-ERA5; 0.25° horizontal	NILU

**Table 1b:** Satellite observations used during EMeRGe in Europe. LT: local time

Sensor name	Satellite	Equator crossing time	Footprint	Institution
GOME-2	MetOp-B	<del>1009</del> :30 LT	40 x 80 km <sup>2</sup>	IUP Uni-Bremen
OMI	EOS-Aura	13: <del>30-45</del> LT	13 x 24 km <sup>2</sup>	IUP Uni-Bremen
SEVIRI	MSG	Geostationary	3 x 3 km <sup>2</sup>	ICARE

The flight track and patterns available to HALO were constrained by a) flight restrictions from the air traffic authorities and special military used airspaces (SUA), and b) the unstable meteorological conditions dominating in Central Europe during the measurement period (see Sect. 3.4). Flight tracks to investigate the plumes from the MPC targets, London (Great Britain), Benelux/Ruhr area (Benelux countries and Germany, hereinafter referred to as BNL/Ruhr), Paris (France), Rome and Po Valley (Italy), and Madrid and Barcelona (Spain) were selected. It was possible to fly these flight tracks under favourable conditions typically more than once during the EMeRGe IOP, improving somewhat the representativeness of the measurements.



The HYSPLIT dispersion forecast indicated that the MPC pollution plumes targeted by EMeRGe resided predominantly below 3000 m. Consequently, the flights over Europe made use of the HALO long-endurance capabilities to fly in the PBL and incorporated vertical shuttles. Shuttles are defined here as a descent or climb pattern between holding altitudes. Typically, three flight levels (FL), upwind or downwind of the target MPCs were part of the shuttle. Some of the MPC outflows were tagged by a coordinated release of a perfluorocarbon (PFC) tracer at the ground (see S5). Details about flight tracks and flight regions are provided in Sect. 3.6.

### 3.3 EMeRGe instrumentation

A key element of the EMeRGe data are the airborne measurements made on-board HALO, a Gulfstream G550 business jet modified and specifically equipped for scientific research (see [www.halo.dlr.de](http://www.halo.dlr.de)). The HALO payload for EMeRGe comprises a set of state-of-the-art instrumentation for the measurement of trace gases and aerosol particles. Table 2 summarises target species and parameters measured by the instruments installed on-board HALO, which are complemented by the HALO ancillary measurements (BAHAMAS, see S4 in the supplement) during the EMeRGe campaign in Europe. The pollutant measurements made aboard HALO were enhanced with tracer experiments using perfluorocarbon compounds (PFCs). Details are provided in the supplement (see S5).

During the preparation and execution phases of the EMeRGe IOP in Europe, the EMeRGe international cooperation provided additional coordinated aircraft-, satellite- and ground-based observations and modelling studies ~~during the preparation and execution phases of the EMeRGe IOP in Europe~~, as described in the supplement (see S6). To assure the accuracy and comparability of the instrumentation on-board, one research flight on 13 July 2017 was dedicated to common and simultaneous measurements of HALO and the Facility for Airborne Atmospheric Measurements (FAAM, [www.faam.ac.uk](http://www.faam.ac.uk)) from the UK Natural Environment Research Council in a so-called blind intercomparison exercise (see S7 in supplement).

**Table 2:** HALO instrumental payload for EMeRGe: PeRCA: Peroxy Radical Chemical Amplification; CRDS: Cavity Ring-Down Spectroscopy; HVS: High Volume Sampler; GC-C-IRMS: Gas Chromatography Combustion Isotope Ratio Mass Spectrometry; PTR-MS: Proton-Transfer-Reaction Mass Spectrometer; CI-ITMS: Chemical Ionisation Ion Trap Mass Spectrometry; GC-MS: Gas chromatography-mass spectrometry analysis; PAN: Peroxyacetyl nitrate;  $\delta^{13}\text{C}(\text{CH}_4)$ : Isotopic signature of methane; PFC: Perfluorinated carbon ~~chemicals~~compounds; DOAS: Differential Optical Absorption Spectrometry; AT-BS: Adsorption Tube and Bag air Sampler; TD-GC-MS: Thermal Desorption Gas Chromatography and Mass Spectrometry; ToF-AMS: Time of Flight- Aerosol Mass Spectrometry; SP2: Single Particle Soot Photometer; CCNC: Cloud Condensation Nuclei Counter; MI: Multi Impactor for aerosol off-line analysis; CPC: Condensation Particle Counter; DMA: Differential Mobility Analyser; OPC: Optical Particle Counter; PSAP: Particle Soot Absorption Photometer. See details and HALO ancillary measurements in the supplement. The instrument details are given in the quoted literature.

Trace gas-in situ measurements				
Species/parameters	Acronym	Institution	Technique/Instrument	Reference
$\text{RO}_2^* = \text{HO}_2 + \sum \text{RO}_2$	PeRCEAS	Univ. Bremen	PeRCA + CRDS	George et al., 2020
VOC/C isotope ratios	MIRAH	Univ. Wuppertal	HVS/GC-C-IRMS	Wintel et al., 2013
OVOC	HKMS	KIT Karlsruhe	PTR-MS	Brito and Zahn, 2011
$\text{O}_3$	FAIRO	KIT Karlsruhe	UV-Photometry/ Chemiluminescence	Zahn et al., 2012
$\text{O}_3$ , CO	AMTEX	DLR-IPA	UV-Photometry/ VUV-Fluorimetry	Gerbig et al., 1996
NO, $\text{NO}_y$	AENEAS	DLR-IPA	Chemiluminescence/ Gold converter	Ziereis et al., 2004
$\text{SO}_2$ , HCOOH	CI-ITMS	DLR-IPA	CI-ITMS	Speidel et al., 2007
a) $\text{CO}_2$ and $\text{CH}_4$	CATS	DLR-IPA	a) CRDS	Chen et al., 2010
b) PAN			b) GC-MS	Volz-Thomas et al., 2001
c) $\delta^{13}\text{C}(\text{CH}_4)$			c) GC-IRMS	Fisher et al., 2006
PFC tracer	PERTRAS	DLR-IPA	AT-BS/TD-GC-MS	Ren et al., 2015
Trace gas- remote sensing measurements				
Species/parameters	Acronym	Institution	Technique/Instrument	Reference
$\text{NO}_2$ , HONO, BrO, $\text{CH}_2\text{O}$ , $\text{C}_2\text{H}_2\text{O}_2$ , $\text{C}_3\text{H}_4\text{O}_2$ , $\text{SO}_2$ , IO	mini-DOAS	Univ. Heidelberg	DOAS / UV-nIR: 2D optical spectrometer	Hüneke et al., 2017
$\text{NO}_2$ , $\text{CH}_2\text{O}$ , $\text{C}_2\text{H}_2\text{O}_2$ , $\text{H}_2\text{O}$ , $\text{SO}_2$ , BrO, $\text{O}_3$	HAIDI	Univ. Heidelberg	DOAS / 3x2D-imaging spectrometers	General et al., 2014
Aerosol measurements				
Species/parameters	Acronym	Institution	Technique/Instrument	Reference
Particle composition	C-ToF-AMS	MPIC Mainz & Univ. Mainz	ToF-AMS	Schulz et al., 2018
BC, CCN, microscopic properties	CCN-Rack	MPIC Mainz	SP2 CCNC, MI	Holanda et al., 2020 Wendisch et al., 2016
Particle size distribution/number concentration	AMETYST	DLR-IPA	CPC, OPC, PSAP, DMA	Andreae et al., 2018
Other parameters				
Species/parameters	Acronym	Institution	Technique/Instrument	Reference
Spectral actinic flux density (up/down) Photolysis frequencies	HALO-SR	FZ Jülich	CCD spectro- radiometry	Bohn and Lohse, 2017
Basic aircraft data	BAHAMAS	DLR -FX	various	Mallaun et al., 2015

333

334

### 3.4 Meteorological conditions

In this subsection, a brief overview of the general meteorological situation over Europe is given. A summary of the meteorological conditions during individual flights is provided later in Sect. 3.6.

The EMeRGe IOP in Europe took place from 10 July 2017 to 28 July 2017. The month of July was selected for the EMeRGe investigation because the summer period in Europe usually offers frequent events of high temperature and high insolation, which result in active photochemical processing of the air masses.

The monthly average weather conditions of July 2017 were evaluated by comparing 500 hPa geopotential height, temperature, wind and precipitable water with a 30-year (1981-2010) reference climatology using NCEP reanalysis data (Kalnay et al., 1996). As shown in Fig. 2, stagnation events, high temperatures and insolation dominated Southern Europe similar to the average of the 30-year climatology. At the ground, the summer 2017 was characterised by a number of heatwaves, which contributed to the propagation of frequent fire events especially on the Iberian Peninsula (EEA, 2018). Several EMeRGe flights were affected by such fires in the southern Mediterranean area as summarized later in Sect. 3.6. Furthermore, in Sect. 4.4 more details are given on how the emissions from these fires frequently interacted with anthropogenic and other natural emissions. In contrast, during the EMeRGe period Northern Europe was influenced by a pronounced negative upper-level pressure and temperature anomaly. The polar front was positioned further southwards than usually and accompanied with anomalously high upper-level wind speeds over Central Europe. These conditions favoured the passage of upper-level troughs associated with mid-latitude cyclones and enhanced precipitation over Central Europe. A cut-off low located over Great Britain during approximately the last ten days of the campaign led to a pronounced deviation of the average weather conditions in July. Thunderstorms frequently developed near the Alps over Southern Germany and Northern Italy. Due to the various meteorological conditions in Central and Southern Europe, the photochemical processing of the investigated polluted air masses proceeded highly differently as described in more detail in Sect. 4.5.

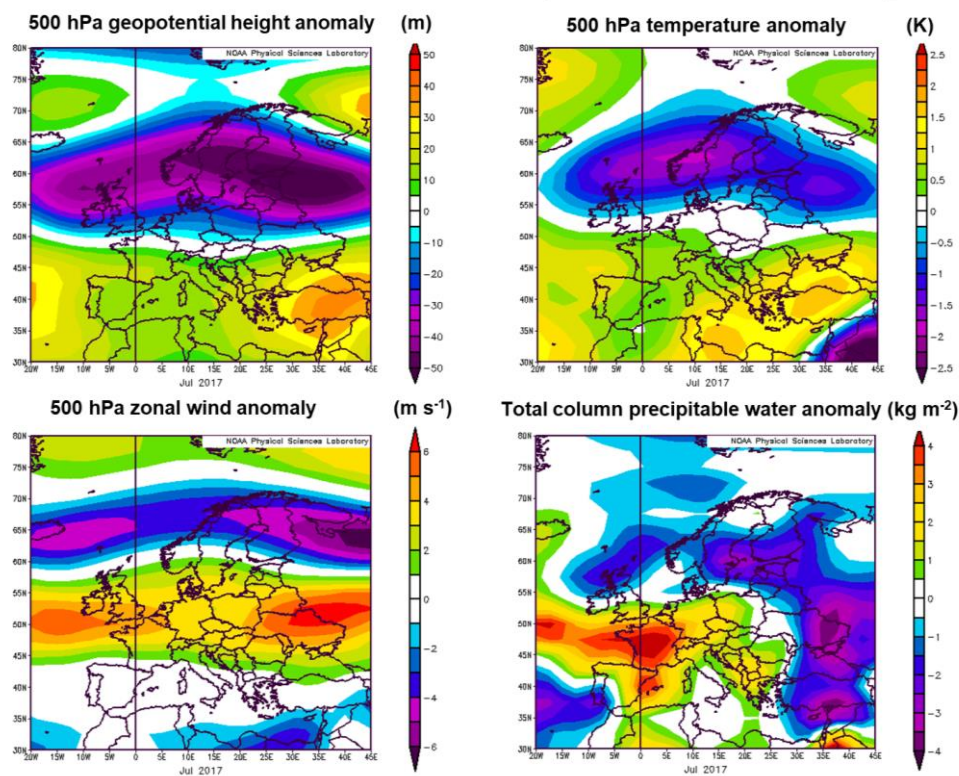


**Figure 2:** Mean anomalies of the 500 hPa geopotential height (top left-panel), temperature (top right), zonal wind (bottom left) and total column precipitable water (bottom right) for July 2017 with respect to a 1981-2010 July climatology based on NCEP reanalysis data (Kalnay et al. 1996). Total column precipitable water is the amount of water potentially available in the atmosphere for precipitation from the surface to the upper edge of the troposphere. NCEP reanalysis data and images provided by the NOAA/ESRL Physical Sciences Laboratory, Boulder Colorado (<http://psl.noaa.gov/>).

### 3.5 Aerosol optical depth

The aerosol load in the target regions during the EMerGe IOP in July 2017 was investigated. Monthly averages of aerosol optical depths (AODs) measured in July 2017 at 17 AERONET sites (AERONET, 2020) covering the EMerGe target regions were compared to the relevant climatology (i.e., the 19-year “July AOD mean” between 2001 and 2019). These AERONET level 2.0 AOD climatological data (Giles et al., 2019) are visualized in Figure 3, referring to 500 nm wavelength. The results show that in July 2017 the aerosol load was generally lower than the relevant climatological value in each target region. For the BNL/Ruhr area (Brussels, Cabauw, Lille, Jülich), Rome (Rome La Sapienza, Rome Tor Vergata), Paris (Palaiseau, Paris), and the Po Valley (Ispra, Modena, Sirmione) the relative deviations of the AODs from the mean values are similar and of the order of -30%. In Rome and the Po Valley the July-2017 AOD is outside the range of the climatological mean and standard deviations. For Eastern Spain (Barcelona, Burjassot, Montsec, Palma) and Southern Great Britain (Bayfordbury, Chilbolton), the aerosol load is closer to the relevant climatology, with relative deviations of 7% and 15%, respectively.

Formatiert: Überschrift 2

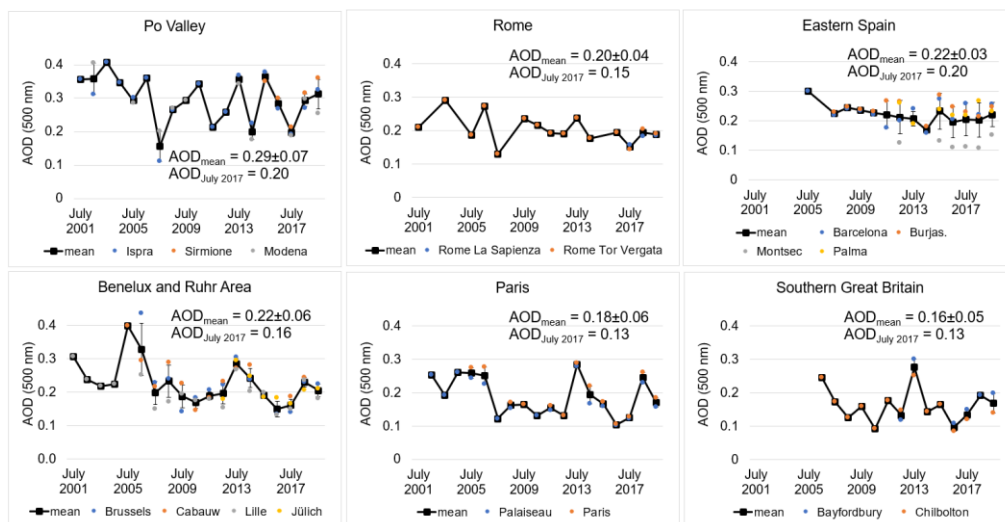


**Figure 3:** Monthly mean AOD values at 500 nm for July (years 2001-2019) in each of the EMeRGe target regions (black squares and standard deviations). These were obtained as mean of the multiple site monthly means (selected sites in colour, see legends). Note that for those AERONET instruments not having the 500 nm filter, the AOD values are interpolated using the Angstrom coefficient between the two closest wavelengths. The values of the climatological- and July-2017- AOD are also reported in the plot insets.

### 3.6 Flight regions and HALO flight tracks

The EMeRGe IOP in Europe comprised seven HALO flights for a total of 53 flight hours. All HALO flights started from the DLR base Oberpfaffenhofen (OP), located Southwest of Munich in Germany. The flights are named E-EU-FN, where E stands for EMeRGe, EU for Europe and FN are the two digits of the flight number. The flight tracks are shown in Fig. 4 and Table 3 summarises the corresponding flight times and targets.

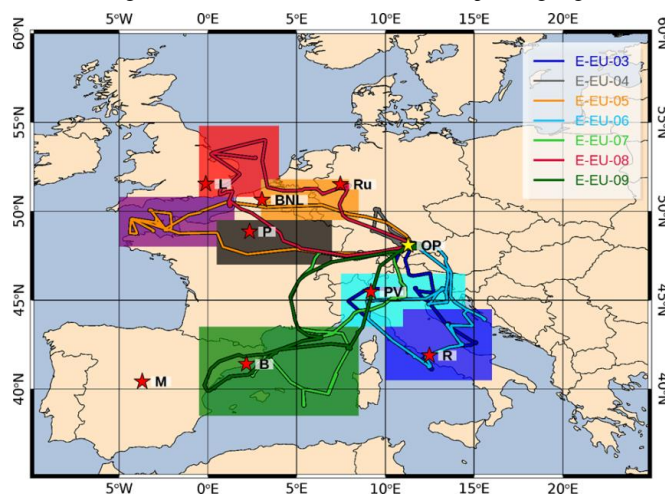


**Figure 4:** HALO flight tracks during the EMeRGe campaign in Europe on 11, 13, 17, 20, 24, 26 and 28 July 2017 (E-EU-03 to E-EU-09, respectively, colour coded). The specific flight times are presented in Table 3. MPC target areas are colour coded by shading: English Channel (purple) North Sea (red) Benelux/Ruhr (orange), Paris (black), Po Valley (cyan), Central Italy (blue), East Mediterranean (green). Distinctive locations/regions are marked with red stars, M: Madrid, B: Barcelona, P: Paris, L: London, BNL: Benelux, Ru: Ruhr area, PV: Po Valley, R: Rome. The coordinates of the MPC areas can be found in the supplement (S8). The position of the HALO base at DLR in Oberpfaffenhofen (OP) is also indicated by a yellow star for reference.

Overall, 60% of the HALO measurements during EMeRGe in Europe were performed below 3000 m to probe fresh and transported outflows of selected MPCs (see Fig. 5 for the distribution of HALO flight altitudes during the EMeRGe IOP).

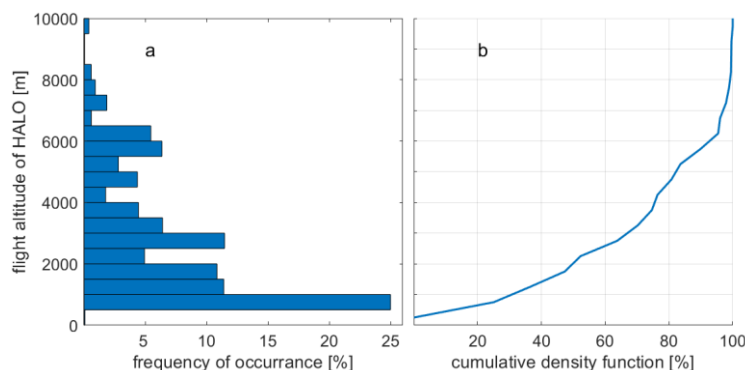


**Figure 5:** Frequency of occurrence of flight altitudes during EMeRGe in Europe in bins of 500 m, a) cumulated frequencies of flight altitudes from the ground to 10000 m b) cumulative density function.

Taking the flight constraints and the prevailing meteorological conditions into account, three flight regions were selected for the identification and measurement of outflows of target MPCs during the EMeRGe IOP:

- a) Flight region 1: Southern Europe - Italy
- b) Flight region 2: London and Central Europe
- c) Flight region 3: Southwestern Europe

#### a) Flight region 1: Southern Europe- Italy

The flight region 1 was selected for the HALO flights E-EU-03 (S9, Fig. S9.1) and E-EU-06 (Fig. 6) on the 11 and 20 July 2017, respectively. The synoptic situation in Europe during these days was characterised by a high-pressure system over the Mediterranean region and a cut-off low over the British Islands associated with the rapid passage of low-pressure systems over Great Britain and Scandinavia. As a result, a Southwest flow with a trough approaching from the West and a short wave passage dominated. These conditions were suitable for the investigation of the MPC targets in Italy (Po Valley and Rome) and of the transport of pollution over the Alps and Apennines. Along the flight route, cloud formation in the Po Valley and thunderstorms in Southern Germany in the afternoon after 15 UTC were observed on both days.

During these flights, BB emissions from forest and intentional fires in Southern Italy, particularly in the Naples area, and along the coast of Croatia were detected. In addition, the transport of mineral dust from Northern Africa to the central Mediterranean and the Italian west coast was observed.

The E-EU-03 and E-EU-06 flights were carried out over approximately the same geographical area. Initially HALO flew over the Alps, then along the Po Valley to the Mediterranean coast of Italy. During E-EU-06 the vertical and horizontal distribution of pollutants was investigated in more detail by shuttles before entering the Po Valley and flying at lower altitudes. The tracks followed the Tyrrhenian Sea heading to the South and crossing the Italian Peninsula from West to East towards the Adriatic coast after a shuttle upwind of Rome. Along the Adriatic coast, shuttles were made while flying to the North. Finally, the flights crossed over the Alps back to OP. The E-EU-06 flight track details are summarised in Fig. 6.



**Table 3:** Characteristics of the HALO flights carried out in Europe during EMeRGe. FR: flight region. Note that E-EU-01 and E-EU-02 were technical flights and are not considered in the present work.

Flight number	Day/ Month	Start/ End time (UTC)	FR	MPC emission and transport targets	Other features
E-EU-03	11/07	10:00/16:30	1	Rome, Po Valley; convection over Alps and Apennines	Mineral dust from Northern Africa; Fires in Southern Italy. Flights Sky Arrow over Rome
E-EU-04	13/07	10:40/15:00	2	Central Europe; Intercontinental transport	HALO-FAAM blind comparison Canada fires
E-EU-05	17/07	10:30/18:30	2	London, BNL/Ruhr, English Channel and Central Europe	FAAM flights over London PFC tracer release
E-EU-06	20/07	9:00/17:30	1	Rome, Po Valley; Convection over Alps and Apennines	Mineral dust from Northern Africa; Fires in Southern Italy and Croatia
E-EU-07	24/07	9:45/18:15	3	Po Valley, South France, Barcelona; West Mediterranean	Dust transport from Northern Africa, fires in Southern Europe
E-EU-08	26/07	7:45/17:30	2	London BNL/Ruhr, Paris; English Channel and Central Europe	PFC tracer releases London, Wuppertal
E-EU-09	28/07	10:00/18:30	3	Po Valley, South France, Madrid, Barcelona; West Mediterranean	Fires in Southern France and Portugal

During E-EU-03 the HALO airborne measurements were complemented by two circuits around Rome by the Sky Arrow aircraft and its payload (see S6 in the supplement), starting at 8 UTC and at 12 UTC, respectively. Each circuit comprised three vertical spirals from 200 m to 1800 m altitude approximately. The interpretation of these airborne observations in combination with ground-based and in-situ data is discussed in Barnaba et al. (2021, 2022, in preparation). Whole air samples for VOCs and their carbon isotope ratios were collected at the ground in evacuated canisters to determine a representative VOC fingerprint for Rome and Milan. To account for emission variations on the ground during the day, air samples were taken around 9 to 10 and 14 h local time.

#### b) Flight region 2: London and Central Europe

The flight region 2 was selected to study the London and BNL/Ruhr outflows with a scientific focus on their transport and interaction over Central Europe. As mentioned in Sect. 3.4, July 2017 had an unsettled weather in the UK and Central Europe with heavy, persistent rain at times and only brief hot spells. This made the selection of optimal flight tracks for this investigation challenging. The precise flight route 2 was tailored for the meteorological conditions prevailing during the E-EU-05, and E-EU-08 flights, which took place on 17 July and 26 July 2017 respectively, to optimally cover different aspects of the target outflows. The flight E-EU-05 (S9, Figure S9.3) took advantage of a short high-pressure ridge that formed behind a trough over Scandinavia on 17 July 2017. The outflow of the MPC London was predicted to travel to the English Channel and the Northern coast of France. This area is regularly used by the UK and French air forces whose activities in the SUAs constrained the original flight options and the flight track were optimised during the flight route. Over the area of interest, HALO flew at different altitudes within the PBL. On the way back to OP, the outflow of Paris was probed South of Orly. On that day, the FAAM platform carried out two complementary circuits around London at 8:00 and 13:30 UTC.

On 26 July 2017, the synoptic situation changed slightly as a cut-off low moved eastwards over Germany while a trough approached from the West. In the period after the cut-off low and before the passage of the warm front over London, the route of E-EU-08 was chosen such that the outflow of London close to the East coast of England and its mixing with the BNL/Ruhr outflow over the European continent were probed (see Fig. 7). Cloudy conditions predominated throughout the day. This flight is studied in more detail in Sect. 4.3. The identification of the London outflow was confirmed by the on-board measurement of a PFC tracer released in the centre of London for both flights. During E-EU-08, a second tracer release was carried out in Wuppertal in the afternoon to identify the BNL/Ruhr outflow. In addition, information on the isotopic fingerprints in VOCs representative for London and Ruhr MPC air were obtained by collecting whole air samples at the tracer release sites before, during and after the release, and in the afternoon (see Sect. 4.5).

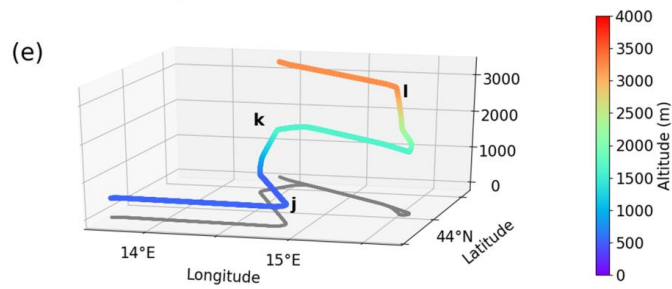
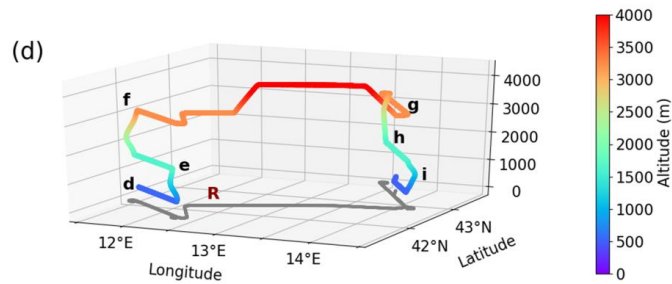
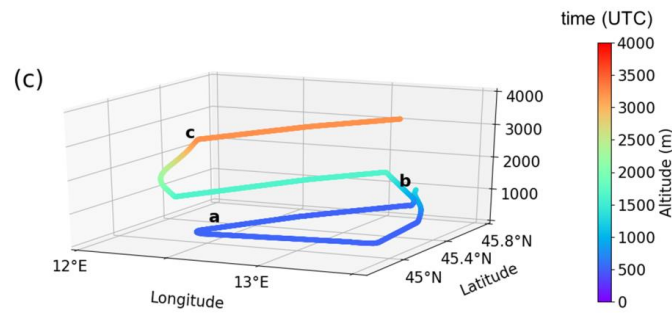
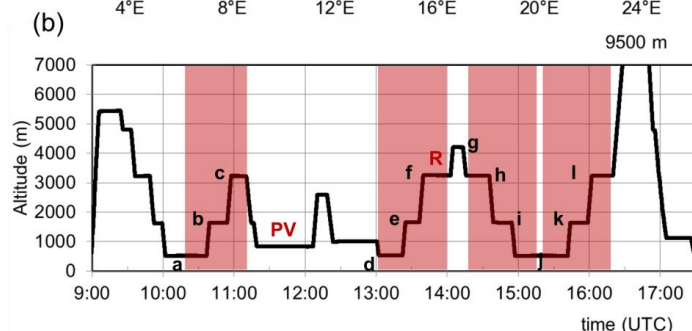
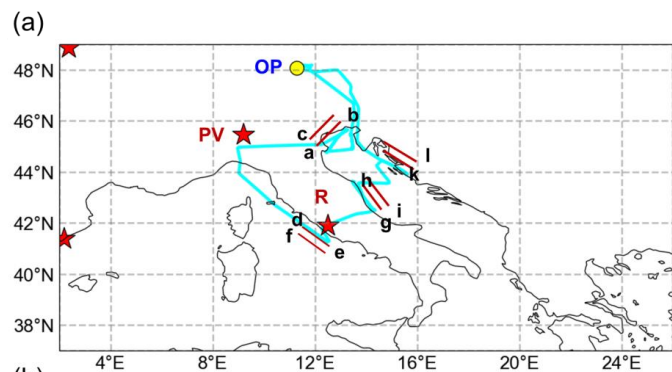
The E-EU-04 flight track on 13 July 2017 is a particular case that also covered Central Europe (see ~~S8-S9~~ in the supplement). The first part of the flight was dedicated to the blind instrumental intercomparison between the HALO and FAAM platforms described in S7 (see Schumann, 2020). A weak high-pressure ridge over Germany dominated. The main objective for the rest of the flight was to probe intercontinental pollution transport between 5000 and 7000 m altitude with signatures of fires originating in Canada.

#### c) **Flight region 3: Southwestern Europe**

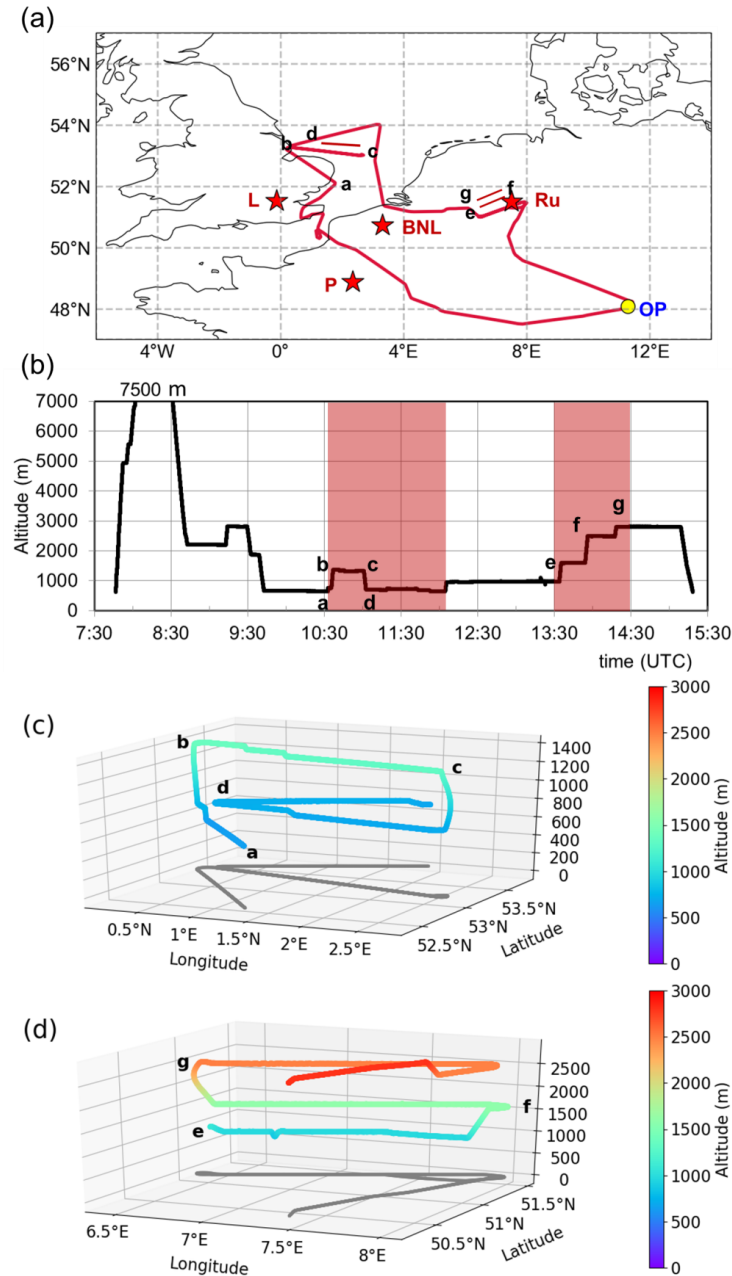
The objective of the flight ~~route-region~~ 3 was to investigate the transport of Southern European MPC outflows into the Western Mediterranean. This flight region was selected for the E-EU-07 and E-EU-09 flights on the 24 and 28 July 2017, respectively. The meteorological situation on 24 July 2017 over Europe was characterised by the eastwards displacement of a cut-off low leaving the British Islands. This was associated with a Southwest flow during the passage of a trough over Spain and France. Dust transport from Northern Africa, thunderstorms in the Po Valley and fires in the South Mediterranean coast of France and Corsica prevailed. The E-EU-07 flight track crossed the Po Valley and focused on the measurement of the predicted outflow of pollution from Southern France and Barcelona into the Mediterranean. Three shuttle flight patterns downwind from Marseille, Barcelona and close to the western coast of Sardinia were carried out (see S9 in the supplement).

On 28 July 2017, a short wave trough with a weak cold front passed over France. This situation led to a prevailing westerly flow and suitable conditions for the E-EU-09 flight over Southern Europe. Two shuttle flight patterns were carried out downwind of Marseille and Barcelona. Features of interest during this flight were the transport of the Madrid and Barcelona outflows in stratified layers into the Mediterranean and the transport of forest fire emissions originating in Southern France and Portugal. This is described in more detail in Sect. 4.3. Further details on all the flight tracks and shuttles are given in the supplement (S9).





481 **Figure 6:** Details of the E-EU-06 flight on the 20 July 2017. Three shuttles took place downwind of the Po Valley (PV),  
 482 upwind of Rome (R) and along the Adriatic coast and are marked with red lines on the map in a), as red shaded areas on the  
 483 altitude diagram in b), and as a 3-D depiction in c), d) and e). The flight tracks during the shuttles d) and e) are shown in  
 484 grey. The flight track in a) is coloured as in Fig. 4 and the EMeRGe MPC targets in red. Main changes in course and altitude  
 485 are marked (a-l) on the graphs for reference. OP indicates the position of the HALO base.



486  
 487 **Figure 7:** Details of the E-EU-08 flight on the 26 July 2017. The position of the shuttles downwind from London and the  
 488 BNL/Ruhr area are indicated in red on the map in a), marked by the red shaded areas in b), and as a 3-D depiction in c) and  
 489 d). The flight tracks during the shuttles are shown in c) and d) in grey. In a) the EMeRGe MPC targets are shown in red and  
 490 the flight track coloured as in Fig. 4. Main changes in course and altitude are marked (a-g) on the graphs for reference. OP  
 491 indicates the position of the HALO base.

### 3.7 Model predicted pollution transport patterns

CAMS global model data (see S3 for the model description) are used here to identify and characterise prominent pollution transport patterns during the EMeRGe IOP over Europe. Figures 8 to 10 show composite average maps of CAMS-global forecasts at 12 UTC for the EMeRGe flights to the North (Flight region 2: E-EU-05 and E-EU-08) and to the South of Europe (Flight regions 1 and 3: E-EU-03, E-EU-06, E-EU-07, and E-EU-09; see Fig.4 and Table 3 for description). A division into southwards and northwards flights is meaningful, as pollution transport patterns during individual flights in the two subgroups mainly resemble each other. Comparison of the CO city tracer simulations at ~~925-500~~ and ~~500-925~~ hPa (see Fig. 8) indicates that the largest part of the anthropogenic MPC emissions remained close to the surface within the PBL. The emissions from the MPCs in the North (e.g. London, Paris) were frequently transported eastwards due to the dominant west-southwesterly winds (Figure 8, top left). Emissions from MPCs South of the polar front, such as Madrid, rather remained in the proximity of the emission sources due to variable weak winds (Figure 8, bottom left). Emissions from the highly polluted Po Valley were often transported to the Northeast and lifted over the high mountains of the Alps (Figure 8, bottom right).

During flights towards the South, higher temperatures and dry conditions in Southern Europe favoured O<sub>3</sub> production and smog events (Fig. 10, bottom left). These meteorological conditions supported the propagation of multiple and mostly intentionally started fires in the Mediterranean area. Average fire radiative power observed by MODIS (MODerate resolution Imaging Spectroradiometer, <http://modis-fire.umd.edu/>) and assimilated within CAMS-global over Europe in July 2017 is included in the supplement (S10). Fire hot spots are visible around the Mediterranean and in Portugal. Further evaluation of the CAMS simulations shows that CO emitted by fires around the Mediterranean mainly remained below approximately 700 hPa. In contrast, CO resulting from the LRT of North American fire emissions was observed around 500-700 hPa over Europe. The average fields show that CO from North American fires was expected to be more pronounced during flights to the North (see Fig. 9), than to the South (see Fig.10) with a maximum in the average fields over Great Britain.

The stratospheric O<sub>3</sub> tracer indicates that stratospheric intrusions concurred with LRT of North American fire emissions initially lofted by warm conveyor belts or deep convection. Dry air masses rich in O<sub>3</sub> were transported downwards to comparably low altitudes. In the average fields of stratospheric O<sub>3</sub> for flights towards the North (see Fig. 9, bottom right), a stratospheric intrusion over Europe stretches broadly from Southern Greece and Southern Italy to the Northeast. The latter is associated with the cut-off low which developed on 20 July 2017 over UK and dominated the weather conditions over Europe for approximately one week.

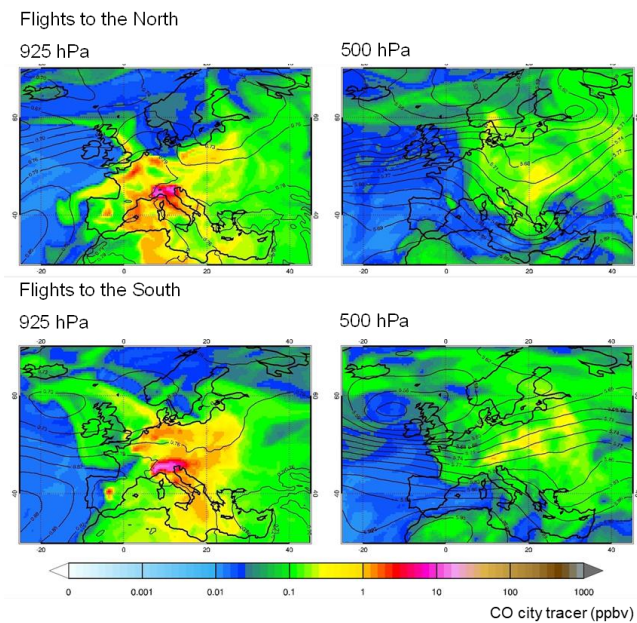


**Figure 8:** Coloured shadings of composite averages of CAMS-global city tracer forecasts of CO (ppbv) at 925 hPa (left) and 500 hPa (right) and 12:00 UTC for days of flights to the North (E-EU-05, E-EU-08, top) and South (E-EU-03, E-EU-06, E-EU-07, E-EU-09, bottom) of Europe. Black contours show corresponding averages of geopotential height (km) from the ECMWF-Integrated Forecasting System (IFS).

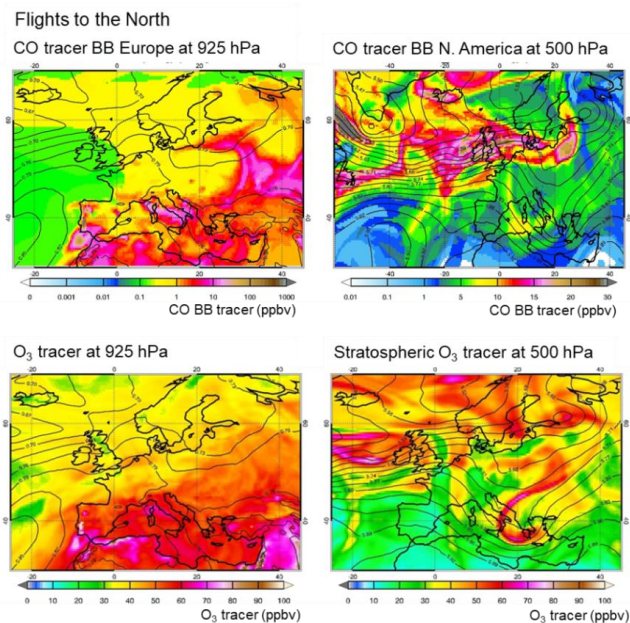


**Figure 9:** Coloured shadings of composite averages of CAMS-global forecasts at 12:00 UTC for flights to the North (E-EU-05, E-EU-08): BB CO tracer (ppbv) from Europe at 925 (top left), and from North America at 500 hPa (top right); O<sub>3</sub> (ppbv) at 925 hPa (bottom left), and stratospheric ozone tracer (ppbv) at 500 hPa (bottom right). Black contours show averages of geopotential height (km) from ECMWF-IFS. Note the different scales. The BB tracer from North America (top right) is shown on a larger map than the other CAMS forecasts in this image.

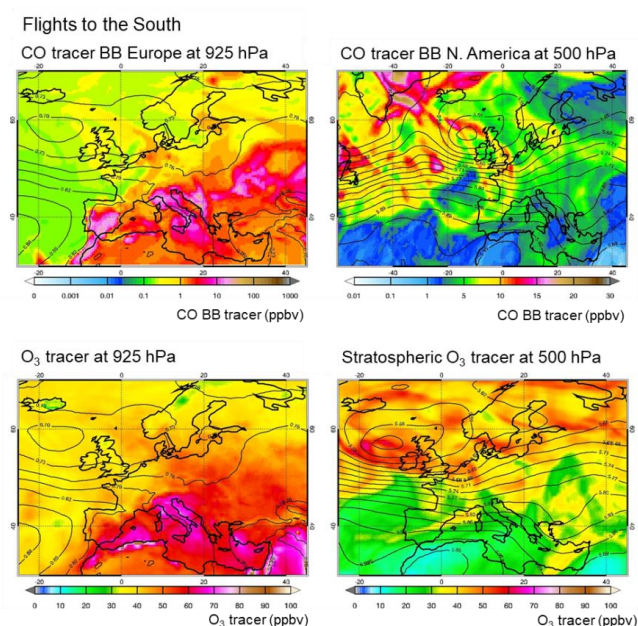


**Figure 10:** Coloured shadings of composite averages of CAMS-global forecasts as in Fig.109, but for flights to the South (E-EU-03, E-EU-06, E-EU-07 and E-EU-09). Note that the BB tracer from North America (top right) is shown on a larger map than the other CAMS forecasts in this image.

#### 4 Transport and transformation of pollution plumes during the EMerGe IOP in Europe

The EMerGe campaign in Europe focused on the identification and measurement of plumes of pollution from selected MPCs, i.e. their emissions, transport and transformation. EMerGe achieved its measurement objectives by exploiting the unique capabilities of the HALO research platform to probe these plumes over a relatively large geographical coverage and by the use of forecasting models and tools. The analysis and publication of EMerGe results is expected to provide new insights into the transport and transformation of pollution plumes over Europe during the IOP in July 2017. In that respect, general findings are summarised in the following sections concerning observations, identification and mixing of the plumes and outflows, and photochemical processing of the air masses encountered.

##### 4.1 Observations

EMerGe provides a unique set of in-situ and remote sensing airborne measurements of trace gases and aerosol particles along flight routes and regions in the lower troposphere over Europe. The use of colocated ground-based and satellite measurements facilitates the interpretation of the HALO measurements during the EMerGe IOP in Europe is facilitated by the use of colocated ground based and satellite measurements. In that respect, EMerGe enhances previous pollution studies in Europe by adding an extensive experimental data set in the PBL. The composition of the sampled air masses is highly variable throughout the flights, which cover large geographical areas of heterogeneous topography, under different solar insolation conditions and proximity to pollution sources. To illustrate this variability, average, median and quartiles values of selected species measured during the EMerGe flights are included in the supplement (S11).

**Formatiert:** Links, Ebene 2, Zeilenabstand: einfach, Nicht vom nächsten Absatz trennen, Diesen Absatz zusammenhalten  
**Formatiert:** Keine Aufzählungen oder Nummerierungen



• Pollution hotspots were identified by using the spatial distribution of trace gases and aerosol particles observed over the flight tracks. A detailed analysis of the complexity of the air masses measured and the variations encountered in individual flights is beyond the scope of the present work and will be presented in dedicated publications. Figure 11 shows as an example the CO, NO, O<sub>3</sub>, CH<sub>3</sub>COCH<sub>3</sub>, CH<sub>4</sub>, and the organic aerosol mass concentrations measured during the EMeRGe flights in Europe. CO, total reactive nitrogen (NO<sub>y</sub>) and its most reactive forms NO and NO<sub>2</sub>, are key species in the identification of anthropogenic pollution. As can be seen in ~~Fig.11~~the figure, the highest NO concentrations were found in the vicinity and downwind of major pollution sources like London, the BNL/Ruhr region and the Po Valley. The Alps and Apennines on the Italian Peninsula lead to the transport of the Po Valley outflow southwards along the Italian Adriatic coast which is the geographic opening of the Po Valley (Finardi et al., 2014). High NO concentrations are indicative of recent or “fresh” anthropogenic emissions. The NO<sub>y</sub> lifetime of a few days enables a more reliable identification of aged polluted air masses further out from the source regions. Maximum NO<sub>y</sub> values as large as 12 ppbv (not shown) were measured over Europe. Elevated CO and NO<sub>y</sub> accompanied by low NO, as measured in the proximity of Barcelona, indicate ~~that there has been a significant amount of~~the processing of the pollution plumes sampled. Emission hot-spots can be hardly identified in the spatial distribution of O<sub>3</sub> as expected from its non-linear secondary formation. Maximum O<sub>3</sub> mixing ratios were generally observed at a distance downwind of MPCs. Organic aerosol has strong anthropogenic sources such as combustion (traffic, fossil fuel combustion, industrial activity, BB), and showed similar behaviour to CO and NO, in that larger mass concentrations were closer in time and space to MPCs such as London, Po Valley, and BNL. The lifetime of aerosol particles in the PBL is in the order of a few days, which explains the high variability observed. Additionally, aerosol particle concentrations presented a strong gradient above the PBL (see Fig.12).

• Signatures of urban sources of long-lived greenhouse gases like CH<sub>4</sub> and CO<sub>2</sub> were identified in the airborne measurements close to the MPC regions in Europe. The identification of plumes of GHG and the quantification of the MPC contributions to the regional GHG budget are challenging. This is caused by the long lifetime of these gases which yields a well-mixed and large atmospheric background. As can be seen in Fig. 11, the highest and most distinctive CH<sub>4</sub> mixing ratios in the PBL were encountered in the Po Valley (up to 2.4 ppm), downwind of London and across the BNL/Ruhr region (up to 2 ppm). Slightly lower mixing ratios were detected downwind of Barcelona (up to 1.94 ppm). The CH<sub>4</sub> mixing ratios were higher than the global mean ground level mixing ratio of around 1.85 ppm for July 2017. At large downwind distances from the MPC regions, the CH<sub>4</sub> emissions are diluted and/or mixed with pollution from surrounding sources. Although the contribution of BB emissions to total global anthropogenic CH<sub>4</sub> is on the order of a few percent (Saunio et al., 2019), mixing ratios of CH<sub>4</sub> comparable to those in urban plumes were occasionally measured in BB events that strongly influenced the local GHG distribution, as during E-EU-07 (not shown). For the assignment of the GHG enhancements to their source region, supporting model simulations and complementary measurements of shorter-lived species with smaller background concentrations and thus better signal-to-background ratios are therefore needed (Klausner, 2020).

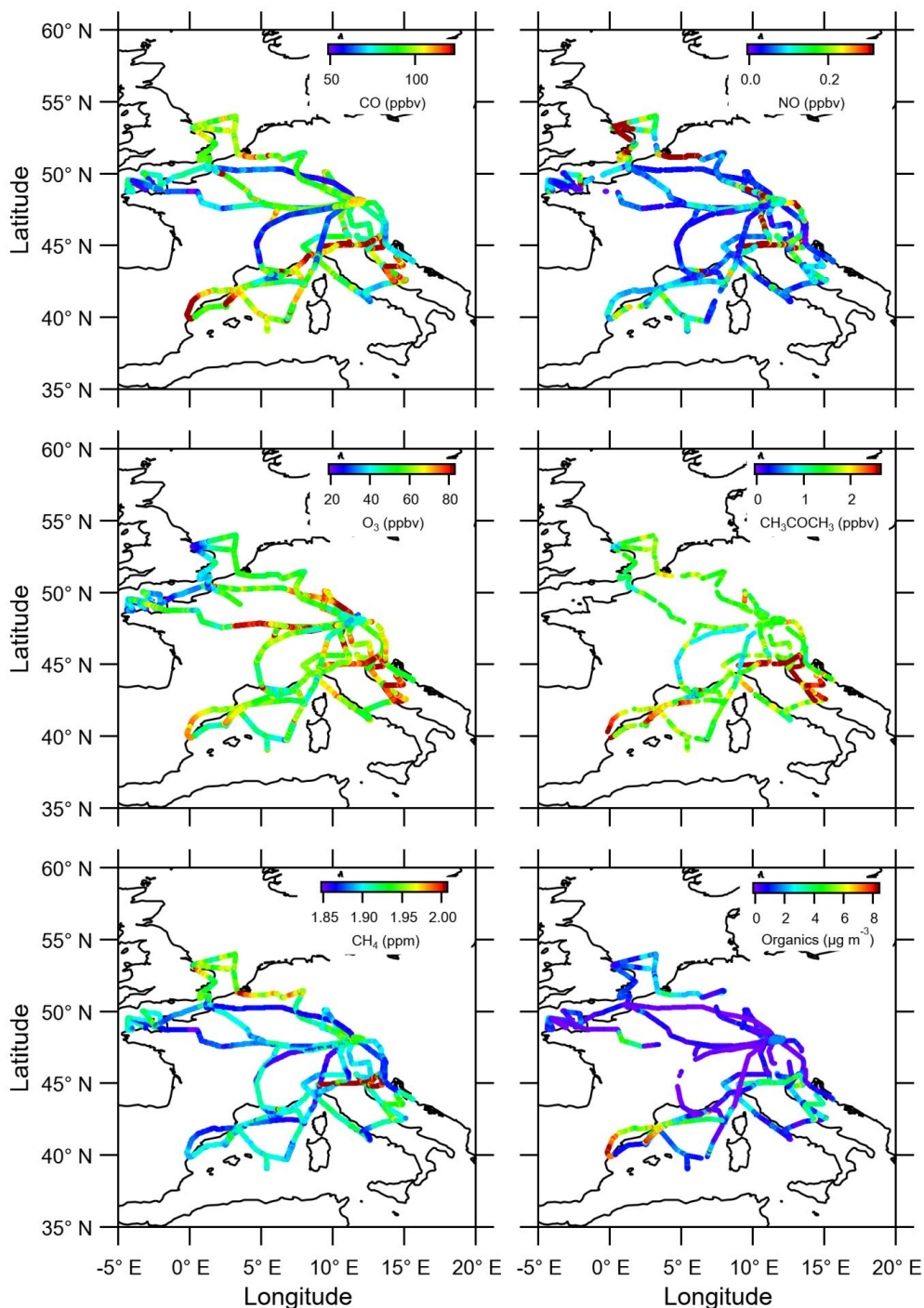


**Figure 11:** Mixing ratios of CO, NO, O<sub>3</sub>, CH<sub>3</sub>COCH<sub>3</sub>, CH<sub>4</sub>, and organic aerosol mass concentrations measured along all EMerge flights in Europe. To increase colour contrast, 50 ppbv has been set as lower limit for CO, and 0.5-3 ppbv and 80 ppbv as upper limit for NO and O<sub>3</sub>, respectively. These limits are representative for more than 95% of all measurements. CH<sub>4</sub> mixing ratios are maximum values in 0.05 x 0.05° bins as in Klausner (2020). Organic aerosol mass concentrations are plotted for the original time resolution of 30 sec and 8 µgm<sup>-3</sup> were set as upper limit. Note that mixing ratios measured at different altitudes in the shuttle areas are not distinguishable in the figure.

Formatiert: Hochgestellt

606 • ~~Interestingly, Large amounts of the~~ HONO detected in the moderately polluted upper boundary layer (several  
607 100 ppt) and in the lower free troposphere (several 10 ppt) often exceeded mixing ratios expected from known  
608 gas-phase reactions as indicated by comparisons with model simulations. Potential mechanisms for the  
609 heterogeneous HONO formation are explored using theoretical studies in combination with the gas-phase,  
610 aerosol composition and radiation observations. These measurements indicate that additional HONO is likely  
611 formed by a suite of different heterogeneous processes in the residual layer and lower free troposphere, in  
612 agreement with many near surface observations in the polluted environment. This additional HONO may  
613 contribute significantly to the oxidation capacity of these polluted air masses.

614 • Elevated concentrations of pollutants were typically observed below the top of the BL and occasionally after  
615 being transported over long distances. Curtain maps showing the latitudinal and vertical distributions of selected  
616 species supported the classification of the air masses, especially in the lower 2000 m of the troposphere.

617 Differences observed North and South of the Alps are e.g. evident in Fig. 12, showing a reasonable agreement in  
618 the geospatial distribution of the cloud condensation nuclei (CCN) and CO which has previously been  
619 documented as a nearly linear relationship within the PBL by Pöhlker et al. (2016, 2018). CO is a good tracer for  
620 relatively fresh combustion (e.g. Andreae, 2019). The CO emitted by open BB exceeds concentrations from  
621 anthropogenic sources. Thus, the good agreement ~~for-between~~ CCN and CO in the lower troposphere for the  
622 peak concentrations (color-coded in red in Fig. 12) implies BB to be the source of CCN. Observations of  
623 ~~Elevated CO observations~~ not related to increases in CCN indicate aerosol removal by cloud processing (e.g.  
624 Fig. 12 above 4000 m between 41 and 44°N).

625 The vertical and latitudinal distribution of the CCN number concentration ( $N_{CCN}$ ) showed a strong vertical  
626 gradient. Generally,  $N_{CCN}$  was highest in and above the PBL, up to ~2000 m a.s.l. The  $N_{CCN}$  depends strongly on  
627 the particular air mass, its photochemical history and the source of pollution as shown in Fig. 12b. In Northern  
628 Europe, ~~(from 50 to 55 °N)~~,  $N_{CCN}$  up to 1200 cm<sup>-3</sup> were measured in the London outflow over the North Sea and  
629 over the BNL/Ruhr region. Below 46 °N,  $N_{CCN}$  often exceeded 1500 cm<sup>-3</sup> above the MPC in the Po Valley,  
630 Rome, Marseille and Barcelona, the highest concentrations being observed in the Po Valley. An interesting  
631 observation was the distinct layer of BB smoke measured above the PBL between 2000 and 3500 m altitude,  
632 close to Marseille and Barcelona (40 to 42 °N). The high  $N_{CCN}$  due to BB are episodic in nature, whereas the  
633 CCN emissions from anthropogenic activity are produced daily with probably a weekend modulation. The  
634 vertical profile in Fig. 12b is a composite of all data but clearly shows that altitudes below 2000 m have the  
635 highest  $N_{CCN}$ . The increased values between 2000 and 4000 m are associated with air masses, which either come  
636 from Po Valley air being lifted up the Alps (e.g. Diemöz et al. 2019a, b), or from BB events upwind flowing into  
637 the Mediterranean.

**Formatiert:** Keine Aufzählungen oder  
Nummerierungen, Tabstopps: 0.5 cm,  
Links

**Formatiert:** Tabstopps: 0.5 cm, Links



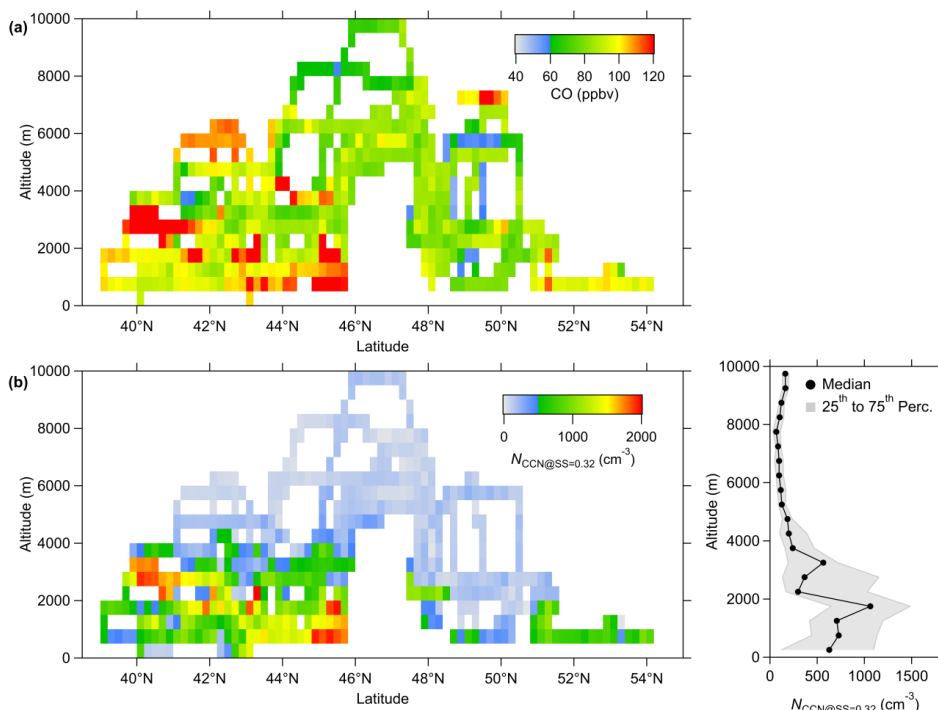


**Figure 12:** Vertical and latitudinal distribution observed during the EMERGE IOP of a) CO mixing ratios, and b) CCN number concentration at a supersaturation ( $S$ ) of 0.32 % (except for E-EU-04, due to instrumental failure). The CCN curtain plot on the **bottom** left is made with latitude- ( $0.2^\circ$ ) and altitude-binned (500 m) CCN number concentrations. On the right, the median vertical  $N_{\text{CCN}}(S=0.32\%)$  profile is represented by a solid black line and the interquartile range by a grey shaded area. CCN data is STP corrected.

#### 4.2 Identification, classification and characteristics of pollution plumes

Anthropogenic and biogenic signatures were identified in the pollution plumes by using enhancements in the concentration of selected species, such as CO, NO<sub>y</sub> and VOCs measured on-board HALO. Measured large pollution plume events were initially categorised into a) anthropogenic pollution (AP), b) biomass burning (BB), c) mixed and d) biogenic plumes, by using enhancements of CH<sub>3</sub>CN, C<sub>6</sub>H<sub>6</sub> and C<sub>3</sub>H<sub>8</sub> over 184 ppt, 49 ppt and 85 ppt thresholds, respectively. These thresholds take into consideration three times the instrumental noise over the limit of detection (LOD) or the individual atmospheric background values. Anthropogenic polluted air masses were e.g. identified by the enhancements of C<sub>6</sub>H<sub>6</sub> and absence of CH<sub>3</sub>CN in contrast with the unpolluted background air **measured** in the absence of both chemical tracers. Similarly, CH<sub>3</sub>CN enhanced plumes in the absence of C<sub>6</sub>H<sub>6</sub> were identified as pure or aged BB events (see S12 for details). Figure 13 illustrates the result of applying this procedure to the flight E-EU-08 on 26 July 2017, which investigated the London and BNL/Ruhr MPC outflows (see Sect.4.3).

**Formatiert:** Schriftart:

**Formatiert:** Links, Ebene 2, Nicht vom nächsten Absatz trennen, Diesen Absatz zusammenhalten

**Formatiert:** Keine Aufzählungen oder Nummerierungen

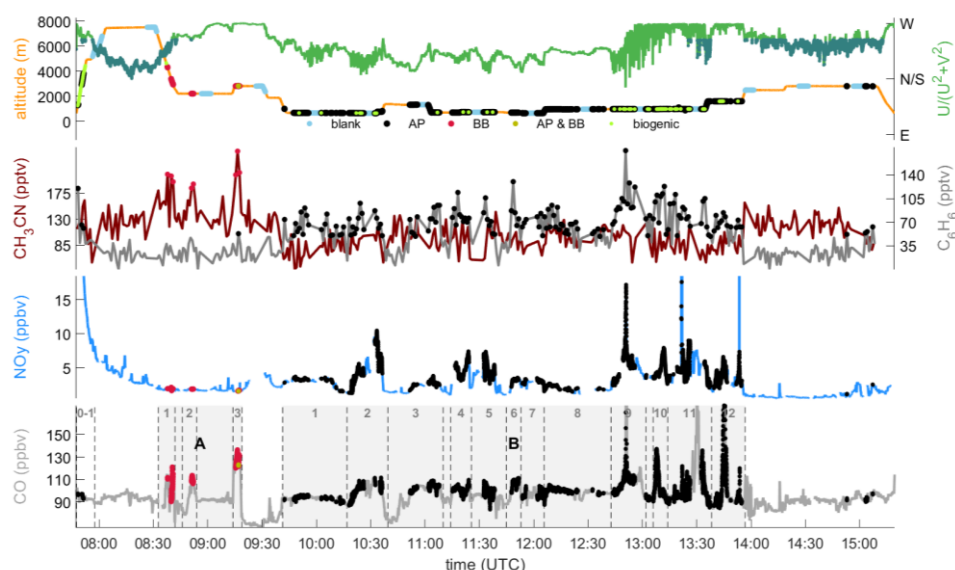


**Figure 13:** Time series for E-EU-08 on the 26 July 2017 used for the categorisation of plumes based on VOC measurements: altitude, wind direction, CH<sub>3</sub>CN, C<sub>6</sub>H<sub>6</sub> and NO<sub>y</sub> as refinement. The wind direction (green line and axis) is given as  $U/(U^2+V^2)$ , -1 is east wind (E), +1 is west wind (W), values around zero have North or South components (N/S). South components are marked with dark green colour. Altitude (brown line, top panel) is colour-coded in green during C<sub>5</sub>H<sub>8</sub> enhancements, in red during CH<sub>3</sub>CN enhancements, in black during C<sub>6</sub>H<sub>6</sub> enhancements and in dark red during both, CH<sub>3</sub>CN and C<sub>6</sub>H<sub>6</sub> enhancements. Additionally, blue colour-coded blank measurements of CH<sub>3</sub>CN, C<sub>6</sub>H<sub>6</sub> and C<sub>5</sub>H<sub>8</sub> are given. In the bottom panel, final numbering of structures and plumes according to concentration enhancements are shown for CO. Colour-coding indicates CH<sub>3</sub>CN enhancements (red), C<sub>6</sub>H<sub>6</sub> enhancements (black), and both, CH<sub>3</sub>CN and C<sub>6</sub>H<sub>6</sub> enhancements (brown).

• The anthropogenic polluted air measured presented during the EMERG IOP presented distinctive features in contrast to background air in Europe. These are summarised as follows:

a) First of all, the maximum concentrations of trace gases and aerosol species of anthropogenic origin were typically measured below 2000 m during the EMERG IOP.

As an example, Fig.14 shows median vertical distributions of observed major primary and secondary VOCs. Longer lived VOCs were, as expected, well mixed in the troposphere and those with anthropogenic sources showed higher variability and highest mixing ratios below 2000 m. Benzene (C<sub>6</sub>H<sub>6</sub>) and toluene (C<sub>7</sub>H<sub>8</sub>) are primarily of anthropogenic origin. HCHO and acetaldehyde (C<sub>2</sub>H<sub>4</sub>O) have anthropogenic BB and significant biogenic sources. They are also generated downwind by the oxidation of transported VOCs. These species have a short lifetime as they are oxidised quickly in the lower layers of the troposphere. As a result, the concentrations observed above 2000 m were close to the LOD. The same is true for isoprene (C<sub>5</sub>H<sub>8</sub>) and xylene (C<sub>8</sub>H<sub>10</sub>) which have lifetimes in the order of some hours.

This vertical distribution is not as evident in glyoxal (C<sub>2</sub>H<sub>2</sub>O<sub>2</sub>) and methylglyoxal (C<sub>3</sub>H<sub>4</sub>O<sub>2</sub>) which result from the oxidation of C<sub>5</sub>H<sub>8</sub> and BB. C<sub>2</sub>H<sub>2</sub>O<sub>2</sub> is also an oxidation product of acetylene (C<sub>2</sub>H<sub>2</sub>) which is of anthropogenic origin. C<sub>3</sub>H<sub>4</sub>O<sub>2</sub> Methylglyoxal is produced in the oxidation of CH<sub>3</sub>COCH<sub>3</sub>, which is thought to have a dominant biogenic source (Andreae, 2019; Wennberg et al., 2018). Both gases are also formed during the oxidation of other VOCs, particularly alkenes, aromatics, and monoterpenes (Myriokefalitakis et al., 2008; Fu et

**Formatiert:** Keine Aufzählungen oder Nummerierungen, Tabstopps: 0.5 cm, Links

**Formatiert:** Keine Aufzählungen oder Nummerierungen

**Formatiert:** Listenabsatz, Tabstopps: 0.75 cm, Links

al., 2008; Taraborrelli et al., 2020) and are present both as primary or secondary pollutants during BB events (e.g., Vrekoussis et al., 2009; Alvarado et al., 2020). Acetonitrile ( $\text{CH}_3\text{CN}$ ) and acetone ( $\text{CH}_3\text{COCH}_3$ ) are typically well mixed in the troposphere due to their longer lifetimes, which are in the order of months. The increase of median  $\text{CH}_3\text{CN}$  with altitude identifies the LRT of BB emissions from North America and the local transport of BB events in Europe.

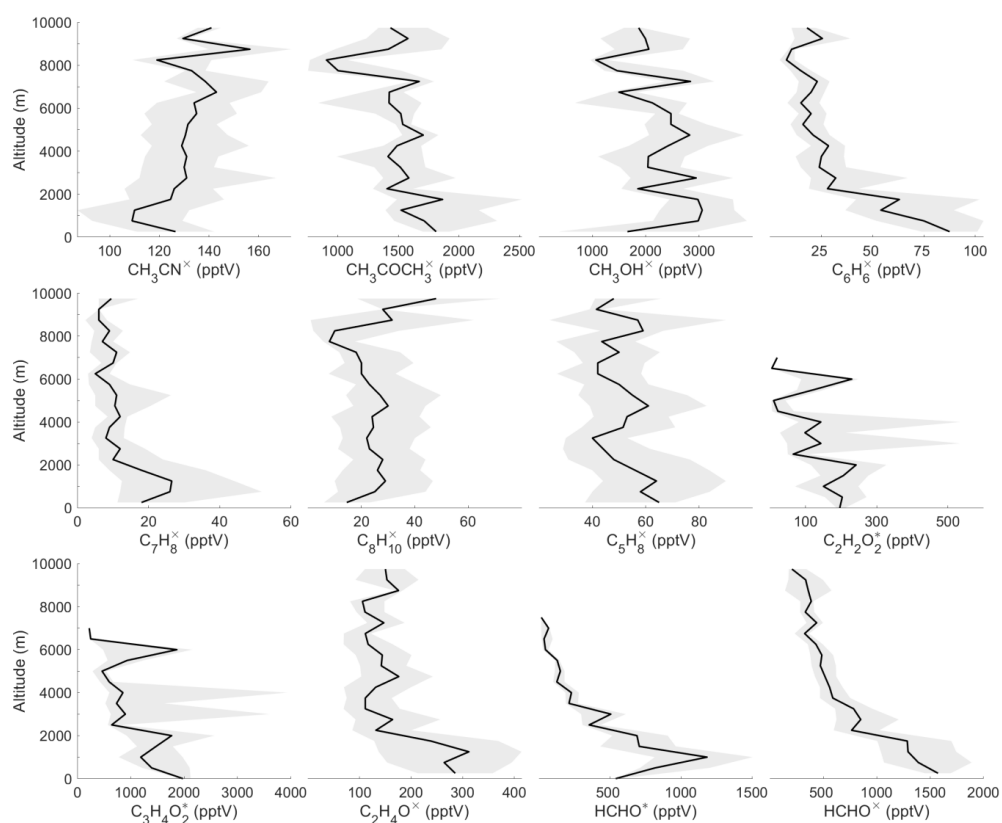


**Figure 14:** Variation of VOC versus altitude measured by the HKMS (labeled with \*) and the miniDOAS (labeled with \*) instruments during EMeRGe over Europe. Shaded areas are the quartiles, solid lines represent median concentrations.

During EMeRGe, HCHO was measured by the in-situ HKMS and the mini-DOAS remote sensing instruments (see Table 2). These instruments probed slightly different air masses due to their instrument characteristics (for averaging kernel of the mini-DOAS instrument see S11 in the supplement), and did not operate at strictly the same data rate and for the same times. For example, unlike HKMS, mini-DOAS did not probe the polluted air masses during aircraft ascent and descent from OP. Despite differences in sampling volume, rate and time, the instrument specific average vertical distribution of HCHO measured on-board HALO by both instruments illustrates in a similar manner the differences in trace gas concentrations encountered in polluted and background air during the EMeRGe IOP (see Fig. 15). In the air masses classified as polluted, the HCHO results from direct emission and oxidation of VOC precursors and is discernibly higher than the lower boundary of the

measurements. The HCHO in the less polluted or background air in Europe is then attributed to be predominantly released from CH<sub>4</sub> oxidation.

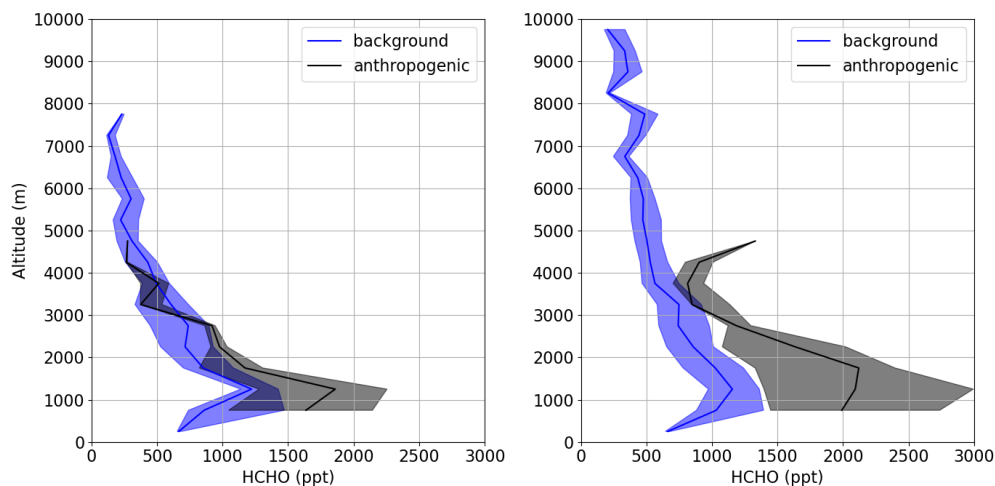


**Figure 15:** Vertical profiles of HCHO (miniDOAS left, HKMS right) for pure anthropogenic emissions (C<sub>6</sub>H<sub>6</sub> enhancement in absence of CH<sub>3</sub>CN) and background air (in the absence of C<sub>6</sub>H<sub>6</sub> and CH<sub>3</sub>CN). Shaded areas are the quartiles, solid lines represent median concentrations.

The HCHO mixing ratios measured during the IOP in Europe are consistent with previous remote sensing observations over South East Asia (Burrows et al., 1999) and North America in summer (Kluge et al., 2020; Chance et al., 2000; Dufour et al., 2009; Boeke et al. 2011; De Smedt et al., 2015; Kaiser et al., 2015; Chan Miller et al., 2017, and references therein). They are also in the same range as those measured in the Po Valley (Heckel et al., 2005). The HCHO mixing ratios observed in the PBL and middle troposphere during EMeRGe are somewhat lower than all summer North American mixing ratios previously measured (see Fig. 16). The emissions of HCHO and its VOC precursors have been reported in previous studies to be lower in Europe than in North America (e.g. Dufour et al., 2009; De Smedt et al., 2015). However, as several EMeRGe flight tracks were carried out far from emission sources over the North and the Mediterranean Seas, this difference might be related to a larger marine influence to the air masses analysed over Europe.

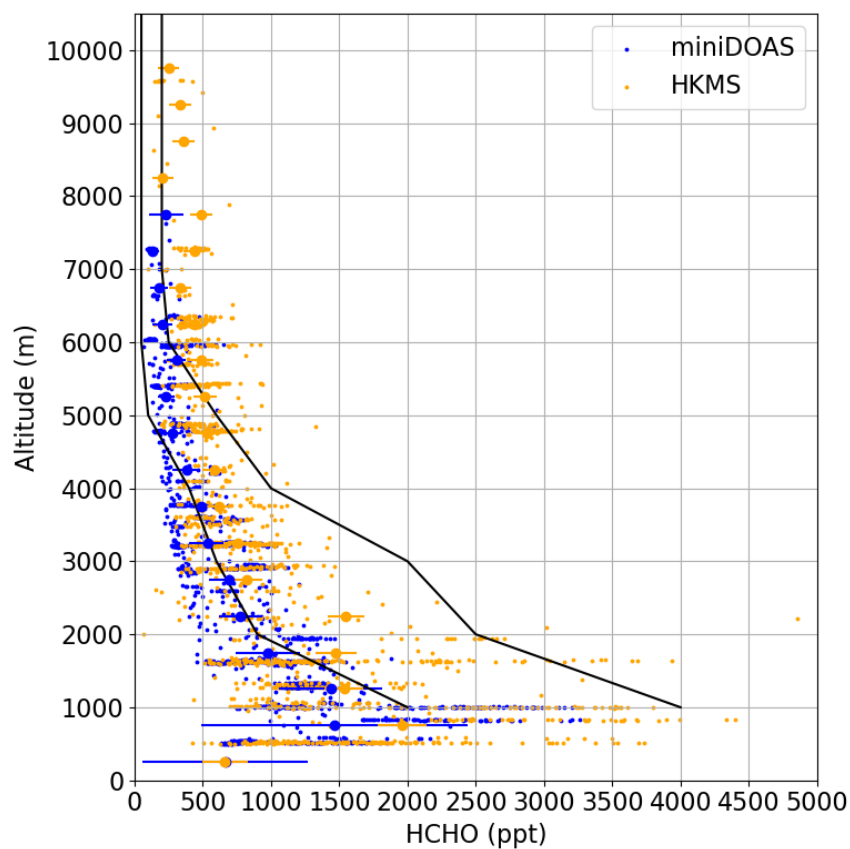


**Figure 16:** HCHO measurements by the HKMS (in orange) and the miniDOAS instruments (in blue). Mean values (bigger dots) and the respective accuracies (horizontal bars) are also shown. The black lines indicate the range of previous HCHO measurements over North America in summer (Kluge et al., 2020). Note that HKMS and miniDOAS agree within their accuracies in spite of having different air sampling volumes, which did not perfectly overlap.

b) Concerning particle measurements, ~~Inside pollution plumes~~ small particles in the diameter range 0.01 to 3  $\mu\text{m}$  dominated inside pollution plumes. In the vertical distribution of the total aerosol number concentrations (Fig. 17a), the difference between anthropogenic and background air masses is more pronounced in the size range between 0.25  $\mu\text{m}$  and 3  $\mu\text{m}$  than in the size range between 0.01  $\mu\text{m}$  and 3  $\mu\text{m}$ . At altitudes below 4000 m the averaged total aerosol number concentrations show several maxima which are mainly caused by local pollution plumes. In contrast to all other profiles, there are two additional maxima in the number concentration compared to background aerosol for the size range 0.01  $\mu\text{m}$  to 3  $\mu\text{m}$  at around 6000 m and 7500 m. These maxima are not apparent in the profiles of particle larger than 0.25  $\mu\text{m}$ . The corresponding sequences can be associated with air masses from convective outflows giving rise to enhanced particle concentrations in the sub-100 nm size range.

**Formatiert:** Keine Aufzählungen oder Nummerierungen, Tabstopps: 0.5 cm, Links

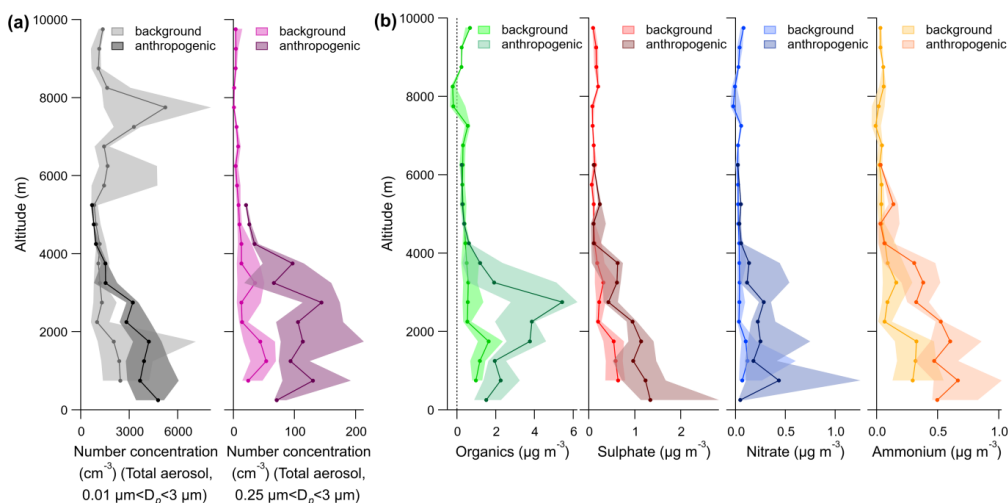


**Figure 17:** As in Fig. 15 but for a) the total aerosol number concentrations for two different size ranges (0.01-3  $\mu\text{m}$  and 0.25-3  $\mu\text{m}$ ), and b) organic, sulphate, nitrate and ammonium mass concentrations in the aerosol particles. The dots in the solid lines represent the medians averaged over altitude bins of 500 m and the shaded areas are the quartiles.

Secondary organic aerosol (SOA) prevailed in the polluted air masses probed in Europe above 2000 m. In the free troposphere above 4000 m the direct effect of anthropogenic emissions on the organic and inorganic aerosol components ~~is~~ was observed to be small. The vertical profiles of the chemically resolved aerosol mass concentrations in Fig. 17b clearly show the enhanced concentrations in the anthropogenically influenced air masses compared to the background air masses. Differences in the median vertical profiles of the inorganic and organic aerosol (OA) suggest that organic aerosol in anthropogenic air masses is mainly formed by secondary processes. The OA maximum between 2000 and 4000 m observed in the anthropogenically influenced air masses can be explained by one particular measurement period above Spain during flight E-EU-09. The trajectory analysis shows an uplift and transport of anthropogenic influenced air masses from Madrid to the measurement location ([see 4.3](#)). Further possible reasons might also be lower temperature leading to enhanced SOA formation in this altitude range, but also a longer conversion time of VOCs to SOA in comparison to the conversion time for inorganic aerosol precursor gases. In contrast, the inorganic components of the aerosol, especially ammonium and sulphate ions, show a steady decrease in the anthropogenically influenced air masses until up to about 4000 m. Above that altitude, the difference between background and anthropogenic profiles becomes small for both organic and inorganic aerosol components. This is a very interesting finding, implying that the direct influence of anthropogenic emissions on the aerosol of the free troposphere over Europe is small.

### 4.3 Identification of MPC outflows

The identification of individual MPC sources was possible by using a) enhancements in the concentration of selected atmospheric species, b) backward trajectories and the last contact with PBL, c) forward trajectories and [calculation of the](#) dispersion of MPC outflows, and d) detection of released PFC tracers. Details about the plume identification and tagging approaches used during the EMeRGe IOP in Europe are given in the supplement (S12).

MPCs were, as expected, identified as significant sources for reactive nitrogen species. The concentration of reactive nitrogen species within pollution plumes exceeded the background concentration by up to a factor of 10. With increasing distance to the MPC sources reactive nitrogen species were processed and finally removed from the atmosphere as indicated by correlations observed with CO.

MPC outflows not sampled by [in-situ](#) instruments were identified during overpasses by the down-looking remote sensing instruments on-board HALO. Fig. 18 shows HAIDI measurements at 8 km of the Milan outflow during E-EU-09. The measurements of HAIDI were used to estimate emissions and plume geometries, NO<sub>2</sub> being an important target species. The HAIDI instrument has three scanning telescopes pointed at nadir, 45° forward and 45° backwards direction. On the left side of Fig.18, the data from the nadir telescope scanner are shown at high spatial resolution (a pixel is ca.400x 400 m). The map shows a strong NO<sub>2</sub> plume Northeast of Milan. The plume substructures are also clearly visible. On the right side of the figure, the data from all three telescope scanners are plotted as a function of time at a lower spatial resolution. The time delay of about 80 s between the peak as seen in the forward and backward scanners indicates that this plume is close to the ground. Wind data from the lowest layer from the ECMWF ERA-5 reanalysis product [\(Copernicus Climate Change Service, 2017\)](#) implied a wind angle of 293°, which is consistent with this outflow from the urban area East of Milan. ~~The uncertainty in the estimated NO<sub>2</sub> emission rate of 607± 67 kg/day may be increased due to the low~~ wind speed (0.6 m/s), the complex plume shape and the small relative angle between the HALO flight track and the plume direction ~~might increase the uncertainty in the estimated NO<sub>2</sub> emission rate of 607± 67 kg/day.~~

**Formatiert:** Links, Ebene 2, Nicht vom nächsten Absatz trennen, Diesen Absatz zusammenhalten

**Formatiert:** Keine Aufzählungen oder Nummerierungen

**Formatiert:** Keine Aufzählungen oder Nummerierungen, Tabstopps: 0.5 cm, Links

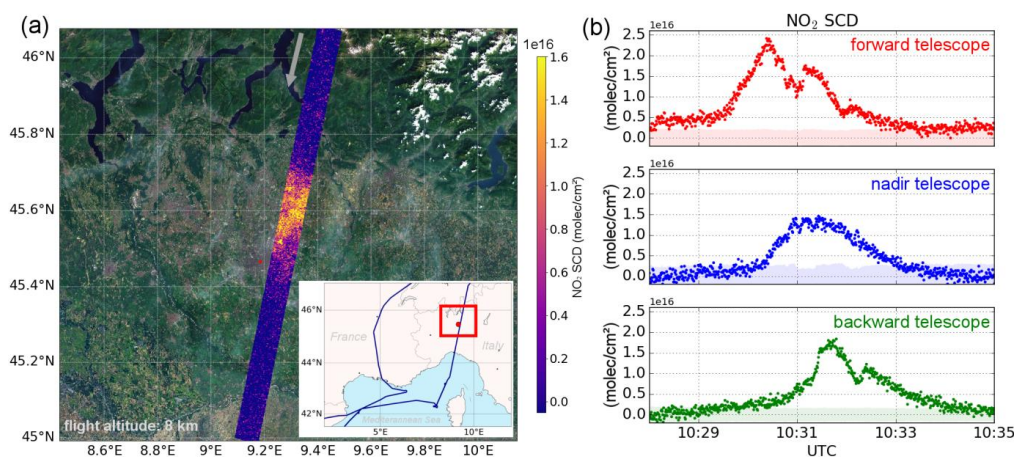


**Figure 18:** HAIDI measurement at 8 km altitude of the Milan outflow during the flight E-EU-09: a) pixel-resolved NO<sub>2</sub> slant column densities observed by the nadir camera (marked by the red square on the map). The grey arrow indicates the direction of the flight. An enhancement of up to  $1.5 \times 10^{16}$  molec/cm<sup>2</sup> over the background is observed Northeast of Milan (red coloured circle), b) NO<sub>2</sub> slant column densities averaged over the whole swath for all three telescopes: forward (top) nadir (middle) and backward (bottom). The height of the plume centre is estimated from the time difference of the maxima. Sources of



790 background imagery: ESRI, DigitalGlobe, GeoEye, i-cubed, USDAFSA, USGS, AEX, Getmapping, Aerogrid, IGN, IGP,  
791 swisstopo, and the GIS User Community.

792 • Different ranges of  $\delta^{13}\text{C}$  values in VOCs were determined and attributed to MPC sources for the first time,  
793 e.g. for  $\text{C}_6\text{H}_6$  in the Po Valley and Rome. Atmospheric residence times of the MPC plumes measured on-board  
794 were retrieved from isotope measurements in VOC samples collected at MPC ground sites in London,  
795 Wuppertal, Milan and Rome and on-board HALO. The vertical distribution of  $\delta^{13}\text{C}$  values in pentanal ( $\text{C}_5\text{H}_{10}\text{O}$ )  
796 and  $\text{C}_6\text{H}_6$  are shown in Fig. 19, colour coded according to the different areas sampled, as given in the overview  
797 map in Fig. 4. In general, the  $\delta^{13}\text{C}$  values are in the expected range reported by previous studies (e.g. Rudolph et  
798 al., 2000; Goldstein and Shaw, 2003).

799 The air samples taken during the EMERGE IOP at ground stations exhibited different features in  $\delta^{13}\text{C}$  values for  
800 the Southern and for the Northern European MPCs. Lower  $\delta^{13}\text{C}$  values for  $\text{C}_5\text{H}_{10}\text{O}$  and  $\text{C}_6\text{H}_6$ , indicative of fresh  
801 emissions, were generally observed below 2000 m altitude. On average,  $\text{C}_5\text{H}_{10}\text{O}$  was less enriched in  $^{13}\text{C}$  in the  
802 Rome and Milan (-32.6 ‰) than in the London and Wuppertal samples (-31.4 ‰), whereas it was the opposite  
803 for  $\text{C}_6\text{H}_6$ , i.e., (-27.3 ‰) and (-29.0 ‰), respectively. Moreover, the  $\delta^{13}\text{C}$  ground values in Italy indicated more  
804 constant sources in  $\text{C}_5\text{H}_{10}\text{O}$  and  $\text{C}_6\text{H}_6$  as in the Northern MPCs, as was apparent from the standard deviations of  
805 0.8 ‰ and 0.7 ‰ in contrast to 1.2 ‰ and 3.3 ‰, respectively.

806 The EMERGE flights to the Southern MPCs in Europe covered a larger altitude range than the flights to the  
807 Northern MPCs. The upwind and downwind shuttles at different flight altitudes of the Rome MPC illustrated a  
808 general increase in  $\delta^{13}\text{C}$  in  $\text{C}_5\text{H}_{10}\text{O}$  and  $\text{C}_6\text{H}_6$  with increasing altitude. This implies that chemically processed air  
809 was encountered during the transits over the Apennines. In comparison to  $\text{C}_5\text{H}_{10}\text{O}$ , the enrichment in  $^{13}\text{C}$  with  
810 altitude in  $\text{C}_6\text{H}_6$  was not very pronounced. This is consistent with the longer lifetime of  $\text{C}_6\text{H}_6$  and a well-mixed  
811 troposphere with a variety of ground sources mixed by convection (e.g. thunderstorms) in summer.  
812 Consequently, the values for  $\delta^{13}\text{C}$  in  $\text{C}_5\text{H}_{10}\text{O}$  represented local conditions, whereas those in  $\text{C}_6\text{H}_6$  provided  
813 regional or LRT information. The isotopic signatures revealed a second layer with rather fresh emissions in the  
814 altitude region between 2000 and 3000 m which extended to 4000 m in the Southern MPCs (e.g. Rome and Po  
815 Valley). These observations were consistent with the trace gases and aerosol measurements.

816 • Concerning The location and position of the city plumes, they were typically well forecasted by the  
817 CAMS-global, MECO(n) regional and by HYSPLIT dispersion simulations using urban city tracers. Figure 20  
818 shows an example with results from E-EU-08 on 26 July 2017 as the London and BNL/Ruhr MPC outflows  
819 were investigated. The HYSPLIT dispersion calculations of the CO city plumes were used to define the location  
820 of the outflows, which were measured along the Eastern UK coast between 10 and 12 UTC and over the  
821 European continent between 13:20 and 14:15 UTC approximately. The plumes identified using enhanced mixing  
822 ratios of selected atmospheric species; and the estimated air-mass transport times are summarised in S13 in the  
823 supplement. These plumes show mixtures of anthropogenic pollution (AP), BB and biogenic emissions (BIO).  
824 Overall, the HYSPLIT dispersion and FLEXTRA backward calculations agreed reasonably in identifying fresh  
825 emitted London plumes such as B-02 and B-04 (see Fig.13): the measured 22 and 19 ppbv CO increases over  
826 background are estimated by HYSPLIT as 25 and 22 ppbv (sum of all transport times). B-05 is a good example  
827 of significant mixing with aged plumes (12-24 h) which seem to dominate in B-06 and B-08 (see detail in Fig.  
828 20). Plume B-09 is a good example of mixing of freshly emitted plumes from BNL/Ruhr (0-6 h) and aged  
829 emissions (>24 h) of London origin.

**Formatiert:** Keine Aufzählungen oder  
Nummerierungen, Tabstopps: 0.5 cm,  
Links

**Formatiert:** Tabstopps: 0.5 cm, Links  
+ 0.75 cm, Links

**Formatiert:** Keine Aufzählungen oder  
Nummerierungen, Tabstopps: 0.5 cm,  
Links



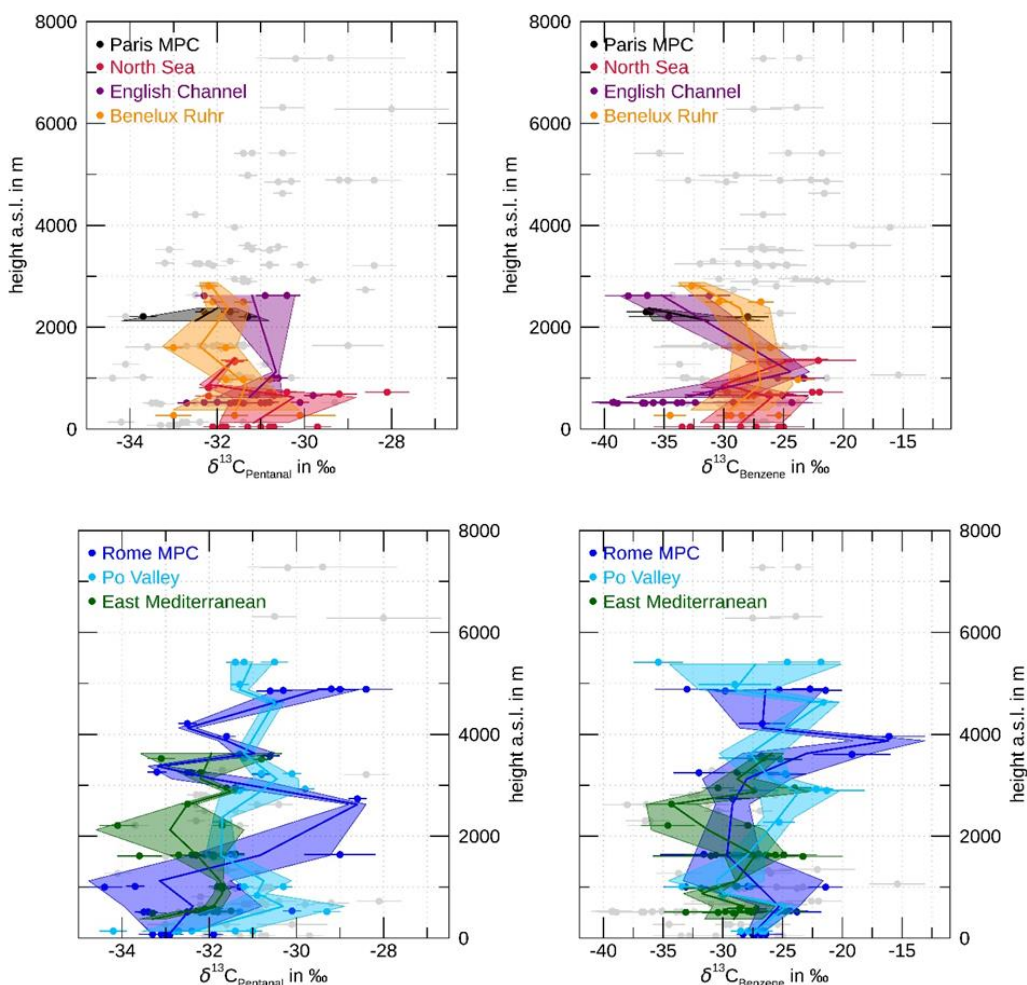


**Figure 19:** Vertical distribution of  $\delta^{13}\text{C}$  values in  $\text{C}_3\text{H}_{10}\text{O}$  (left column) and  $\text{C}_6\text{H}_6$  (right column) in whole air samples taken on HALO and at the ground sites in London, Wuppertal, Milan and Rome. Data for northbound flights (top row) are colour coded for Paris MPC (black), North Sea (red), English Channel (violet), BNL/Ruhr (orange). Data for southbound flights (bottom row) are colour coded for Rome MPC (blue), Po Valley MPC (cyan) and East Mediterranean (green). The coloured shadings refer to the standard deviation of  $\delta^{13}\text{C}$  values in altitude bins of 250 m. Mean  $\delta^{13}\text{C}$  values of the respective altitude bins are represented as solid colour-coded lines. The  $\delta^{13}\text{C}$  values at the lowest altitudes in each colour represent the results of air samples at the ground stations: London (red), Wuppertal (orange), Rome (blue) and Milan (cyan). Error bars in  $\delta^{13}\text{C}$  are given for each sample value. Remaining data are shown in grey.

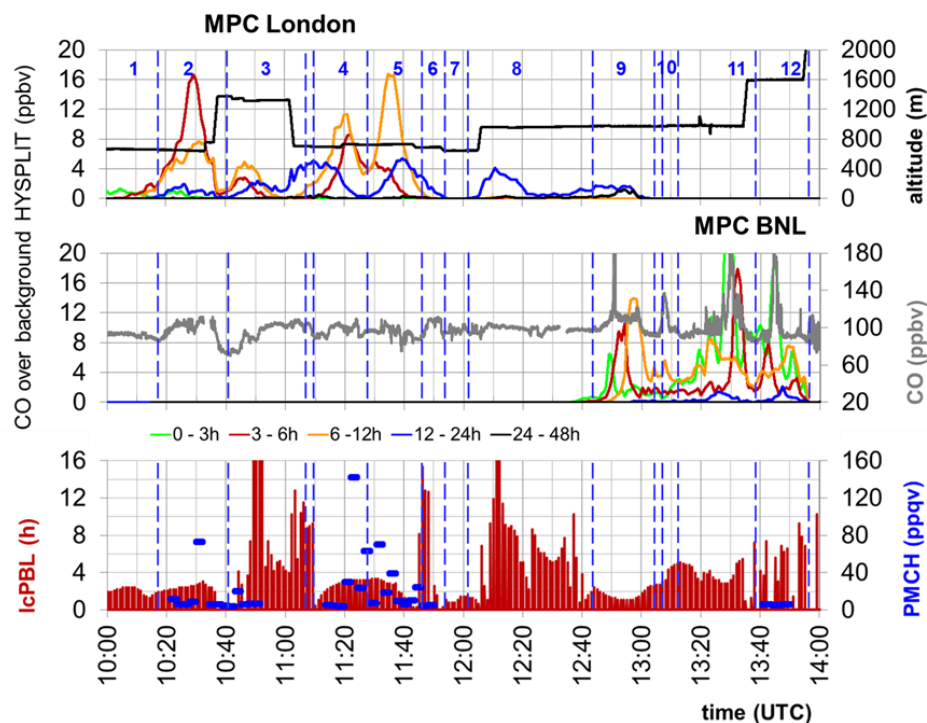


**Figure 20:** Detail of the MPC outflow of London (B-01 to B-09) and BNL/Ruhr (B-09 to B-12) probed with HALO along the E-EU-08 flight track. Numbering in blue corresponds with the classification in Fig. 13 (“B-0” is omitted for clarity). The position of the plumes is also indicated by the blue lines. Dispersion of CO emissions of target MPCs and the transport time of the air mass calculated by HYSPLIT are depicted in the middle panel. The last contact with the PBL (lcpBL) calculated using FLEXTRA is also shown. Elevated PMCH mixing ratios were measured for B-02, B-04 and B-05.

• MPC outflows were successfully and unambiguously identified after transport times of between 5 and 26 hours by tagging polluted air masses through ground-based releases of PFC tracers in the centre of MPCs. The aim of the PFC tracer experiments was to establish Lagrangian connections between polluted air masses in the center of selected cities and downstream measurements on-board HALO guided by HYSPLIT forecasts of the dispersion of the tracer plumes. In Fig. 20 the PMCH volume mixing ratios measured on-board during E-EU-08 are shown. For B-02, B-04 and B-05, enhanced tracer values above the 8.5 ppqv atmospheric background in Europe were clearly detected.

• The downwind impact of pollution from MPCs was identified by combining information from measurements on-board in selected areas with backward and sensitivity trajectories. Figure 21 shows an example of the density distribution for forward trajectories (FT) of MPC Rome outflows. The figure highlights the typical transport pattern towards the Adriatic coast and the representativeness of the HALO shuttles at different altitudes in the Mediterranean and along the Adriatic coast during the flights E-EU-03 and E-EU-06. The flight tracks for E-EU-03 and E-EU-06 are colour-coded with the BC mass, a good tracer for urban emissions (Krüger et al. 2022). The elevated BC mass concentrations observed in the area of an increased FT density over the Adriatic indicates the measurement of urban emissions in the statistically expectable transport pattern for the urban outflow of Rome during the month of July. A comparison of the gases remote sensing observations on-board HALO with their columnar amounts –observed by ground-based measurements in the Rome area in the framework of the

**Formatiert:** Keine Aufzählungen oder Nummerierungen, Tabstopps: 0.5 cm, Links

863 PANDONIA global network for air quality and atmospheric composition ([https://www.pandonia-global-](https://www.pandonia-global-network.org/)  
864 [network.org/](https://www.pandonia-global-network.org/)) is discussed in Campanelli et al. [2021](#) ([in preparation 2021/2022](#)).

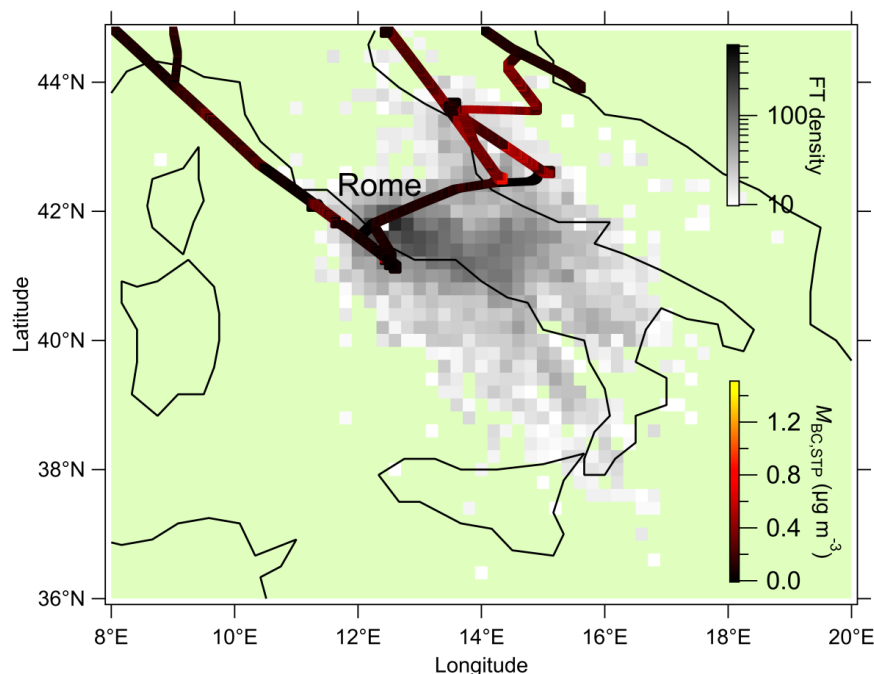


**Figure 21:** Forward trajectory (FT) density plot for air masses starting in Rome (100 m a.g.l.) in the month of July from multiple years (2017 to 2020). The grey scale represents the counts of FT points in each grid cell. The flight track of E-EU-03 and E-EU-06 is colour-coded with the BC mass concentration. The FT density distribution was calculated as explained in Pöhlker et al. (2019). The FT starts at 100 m above ground level for the month of July in a multi-year period (2017 until 2020) by using the HYSPLIT package (version 4, Revision 664, October 2014) (Stein et al., 2015; Rolph et al., 2017).

872 • Regional transport of several European MPC outflows was successfully identified and measured: a) London  
873 over the English Channel to Central Europe, b) Po Valley either North over the Alps or in a south-easterly  
874 direction towards the Adriatic, c) Rome over the Apennines into the Adriatic and d) Madrid and Barcelona into  
875 the Western Mediterranean.

876 The downwind impact of the MPC outflows during EMERGE was explored in respect of the vertical and  
877 horizontal extension of the observed plumes by combining - 4 - information from transects and shuttles in selected  
878 areas. ~~was combined, as~~ An example is shown in Fig. 22 for the B-01 to B-12 plumes during the E-EU-08 flight.  
879 The E-EU-08 track included a flight transect (a-b-c-d-e) at approximately 600 m altitude and a shuttle (600-1400  
880 m) between b-c and c-d in the outflow of London from 10 UTC to 12 UTC. A second shuttle (g-h-i) at 900, 1500  
881 and 2400 m was made in the BNL outflow from 13:20 UTC approximately. Relevant changes in the HALO  
882 course and altitude are marked by coloured circles and letters in Fig. 22. Backward trajectories indicated that the  
883 air measured at around 10:30 UTC at 600 m (blue circle), 11:00 UTC (point c at 1400 m and 600 m), 11:20 UTC  
884 (yellow circle) and 11:50 UTC at 600 m (pink circle) had passed over the MPC London a few hours before being  
885 probed at an altitude below 1000 m. Selected backward trajectories are shown in Fig. 22c. At these times, the  
886 measured enhancements in CO and NO<sub>y</sub> and the NO/NO<sub>y</sub> ratios were in reasonable agreement with the transport  
887 time predicted by HYSPLIT for the CO enhancement in the MPC London plumes in Fig. 20. For plume B-02,  
888 HYSPLIT predicted the London contribution to be a mixture of air masses transported in the previous 3 to 24

**Formatiert:** Keine Aufzählungen oder Nummerierungen, Tabstopps: 0.5 cm, Links

**Formatiert:** Tabstopps: 0.5 cm, Links

hours. The air probed had up to 10 ppb of  $\text{NO}_y$  and approximately 2 ppbv NO. The latter suppresses  $\text{RO}_2^*$ . OH and RO are produced but also react with NO and  $\text{NO}_2$ . These measurements confirm the predicted mixing of relatively fresh emissions with aged and more photochemically processed air masses.

The vertical distribution of CO in the plume during the shuttles is depicted in the 3D diagrams in Fig. 22b. The CO measured indicates that the plume B-03 is well mixed horizontally with the plume B-06 up to 1400 m altitude. According to the backward trajectories (not shown), the plume at 11:52 UTC is transported from the Northeast coast of UK and had no recent contact with the outflow of London. This is distinguishable by the high  $\text{SO}_2$  mixing ratios measured. The plumes B-08 and B-09 measured over the continent at 900 m were predicted to have been in contact with emissions of the MPC London within the previous 24 hours (Fig. 20 and Fig. 22c). From 12:50 UTC the air probed was expected to mix with recent emissions of the MPC BNL as indicated by the observed higher NO levels and enhancements in  $\text{NO}_y$ ,  $\text{SO}_2$  and  $\text{C}_6\text{H}_6$  in Fig. 22a.

The composition of the air measured during the shuttle between the way points g and h in Fig. 22a at 13:30 and 13:45 UTC and the backward trajectories indicated that the outflow from the MPC BNL was sampled in a plume extending from 1000 m to 1500 m. This air mass was not detectable at 2500 m.

Distinct pollution and aerosol layering were observed over some of the investigated MPCs. Collocated ground-based remote sensing instruments improved the understanding of the evolution of the airborne observed scenarios and the attribution of the vertical distribution of pollutants probed during the shuttles.

A particular case of interest was the vertical distribution of pollutants observed at the coast of Barcelona during E-EU-09. HYSPLIT CO dispersion simulations indicated that the Madrid outflow was transported over a long distance above the Iberian Peninsula to the North-Eastern coast at altitudes above 2000 m while in the lower layers the Barcelona outflow predominated, as illustrated in Fig. 23. In contrast with the air sampled at 500 m, the backward trajectories and HYSPLIT dispersion calculations indicated that the air probed from 15:15 to 15:25 UTC at 1600 m had passed over MPC Barcelona within 6-12 hour before sampling. In these measurements, there ~~is~~ was no indication of fresh NO emissions, and  $\text{NO}_y$ ,  $\text{C}_6\text{H}_6$  and CO were significantly higher than at the lower altitude. The layering is attributed to be the result of the recirculation of emissions in the Barcelona outflow within the land-breeze regimes close to the coast. Later at this FL (green and red circles in Fig. 23), the backward trajectories and HYSPLIT estimations indicated sampling of regional emissions that had travelled along the coast from Valencia. This is consistent with the observed decreases in  $\text{C}_6\text{H}_6$ ,  $\text{NO}_y$  and BC. In the upper FL at 15:45 UTC,  $\text{NO}_y$ ,  $\text{C}_6\text{H}_6$  and CO significantly increased in air transported from Portugal (as in the 36 h backward trajectories) across the Iberian Peninsula at altitudes above 2000 m, after PBL contact with the MPC Madrid below 1000 m the evening before. According to the pollution control network of Madrid, the average CO surface concentration exceeded 350 ppb on the 27 July 2017, the zonal wind direction was WSW and the average wind speeds were greater than 16 km/h. The observed mixing ratio decreased when this feature at 3000 m disappeared. Re-entering and stratification of plumes having different processing along the Spanish coast has also been documented in the past (e.g. Millán et al., 1997, 2000 and references therein).

**Formatiert:** Standard, Tabstopps:  
Nicht an 0.75 cm

**Formatiert:** Keine Aufzählungen oder  
Nummerierungen, Tabstopps: 0.5 cm,  
Links

**Formatiert:** Tabstopps: 0.5 cm, Links  
+ 0.75 cm, Links

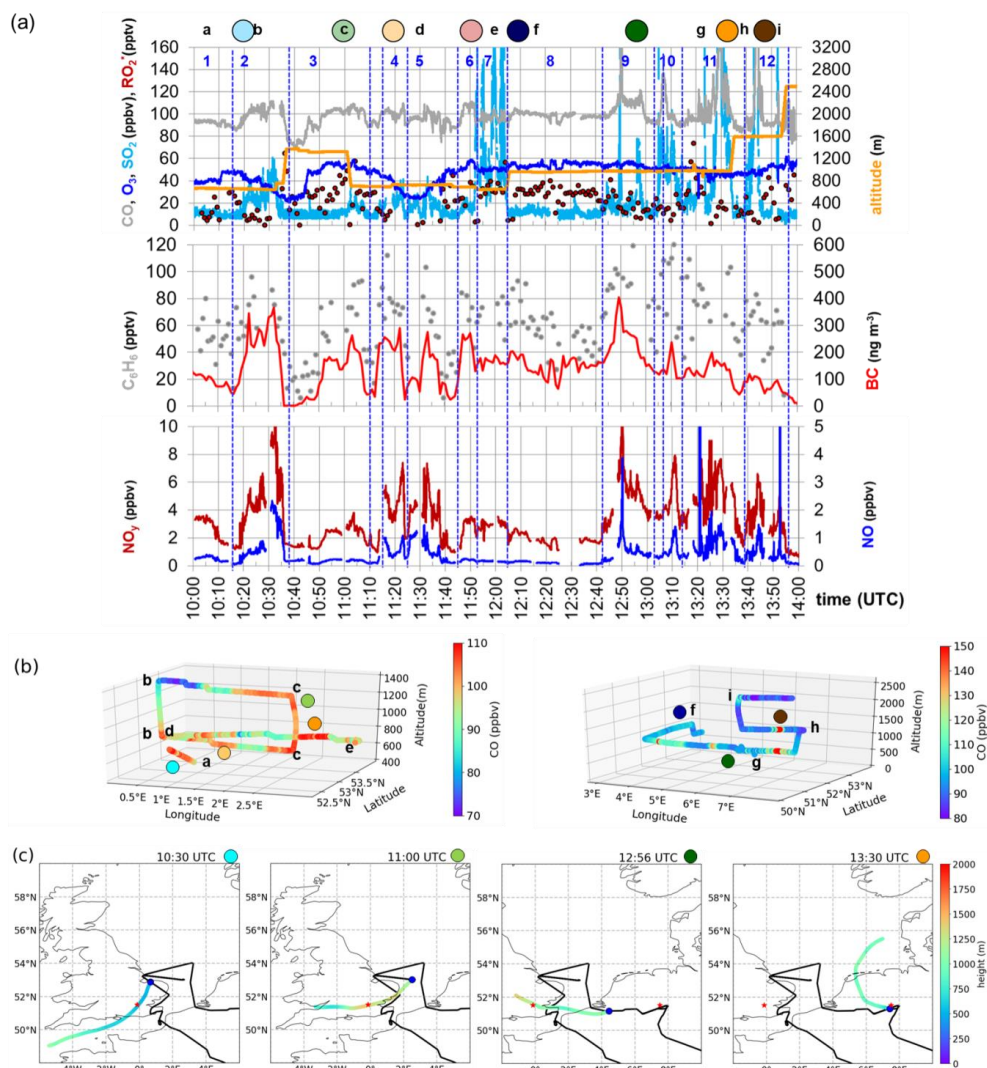


**Figure 22:** a) CO, O<sub>3</sub>, SO<sub>2</sub>, RO<sub>2</sub>\*, NO<sub>y</sub>, NO, C<sub>6</sub>H<sub>6</sub> and BC measured in the outflow of London and BNL during E-EU-08 on 26 July 2017. The position and numbering of the plumes are indicated by blue lines and numbers as classified in Fig. 22 ("B-0" is omitted for clarity), b) 3D shuttles colour coded with the CO mixing ratios observed. Relevant changes in the HALO course and altitude are marked by colour circles and letters (a-i). c) Selected backward trajectories (24h). The red stars and the blue dot indicate the position of the MPCs of interest and of HALO, respectively.



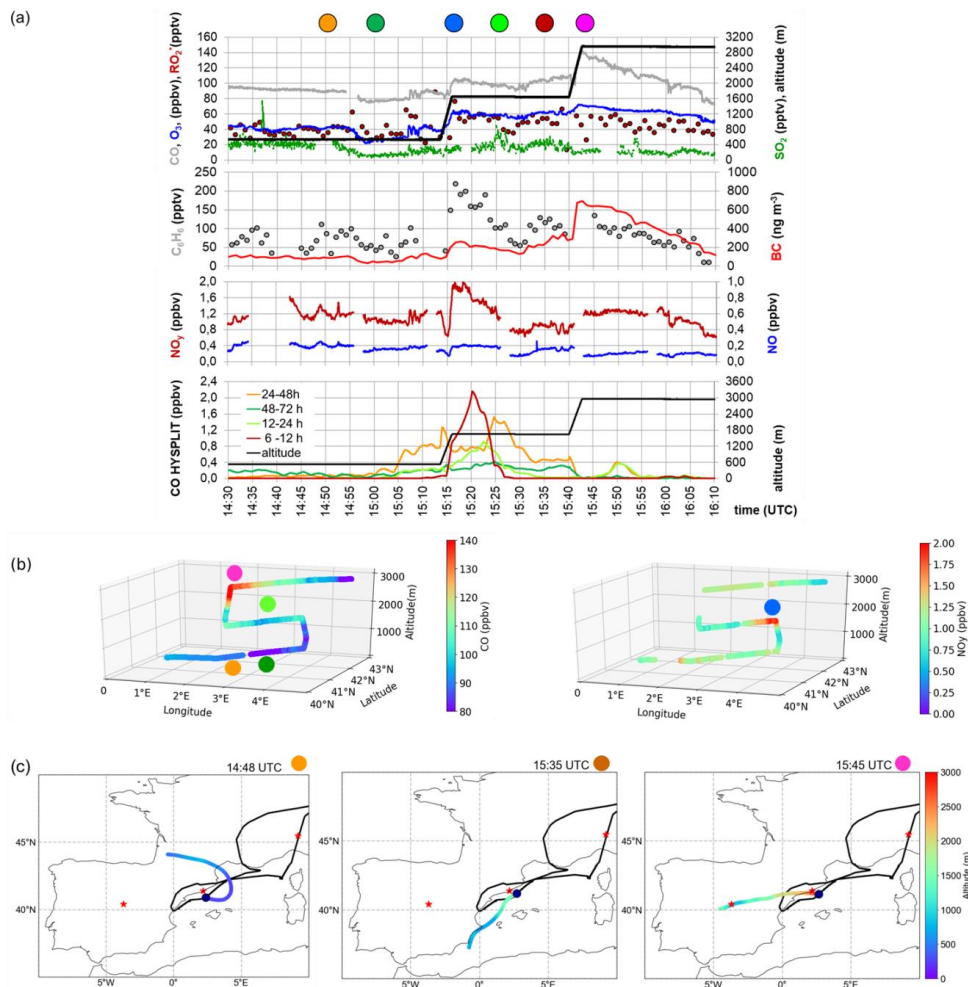


**Figure 23:** Stratified pollution layers along the Spanish coast during the E-EU-09 flight on the 28 July 2017, a) temporal variation of CO, O<sub>3</sub>, RO<sub>2</sub>\*, NO<sub>y</sub>, NO, SO<sub>2</sub>, C<sub>6</sub>H<sub>6</sub> and BC during the shuttle, b) 3D view of the shuttle colour coded with CO (left) and NO<sub>y</sub> (right) mixing ratios, c) selected backward trajectories (last 24h). Coloured circles marked the corresponding times in b). Red stars and the blue dot indicate the position of the MPCs of interest and of HALO, respectively.

Formatiert: Tiefgestellt

The interpretation of these HALO measurements during E-EU-09 was enhanced by using data from the closest four ground-based remote sensing stations available in the framework of EMerge international. enhanced the interpretation of the HALO measurements. These are data of a lidar in Barcelona (BRC) and three ceilometers in Montseny (MSY), on top of the Serra del Montsec (MSA) (Titos et al., 2019), and in Burjassot (VLC) near Valencia. Figure 24 shows the location of the stations with respect to the HALO flight track. The stations MSY and MSA were approached at a flight altitude of 2600 m when HALO entered the air space above the Iberian Peninsula. Subsequently, HALO shuttles were carried out Northeast of Valencia at 500, 1000, 2000 and 2600 m and East of Barcelona at 500, 1600 and 3000 m.

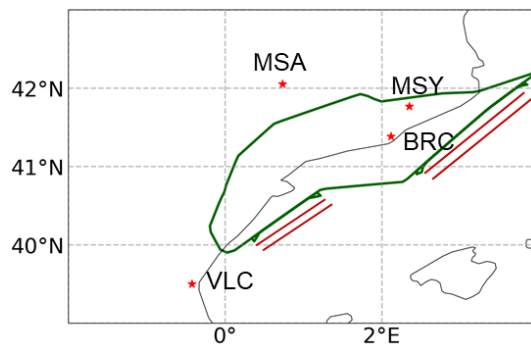


**Figure 24:** Detail of E-EU-F09 flight track (in green) and the ground-based stations with coordinated remote sensing measurements in the vicinity: Montseny (MSY), Sierra del Montsec (MSA), Burjassot (VLC) and Barcelona (BRC). Red lines indicate the position of the HALO shuttles.

The lofted aerosol layer observed at all ground-based remote sensing stations from above the PBL up to 4000 m altitude was also probed by HALO (see Fig. 25). The profiles of the backscatter coefficient derived at MSY, MSA, VLC and BRC on the 28 July 2017 are displayed in Fig. 26 and Fig. 27. The lofted aerosol layer in Fig. 25 corresponds with increased backscatter coefficients ranging from 0.4 to 1.9 ( $\text{Mm}\cdot\text{sr}^{-1}$ ).

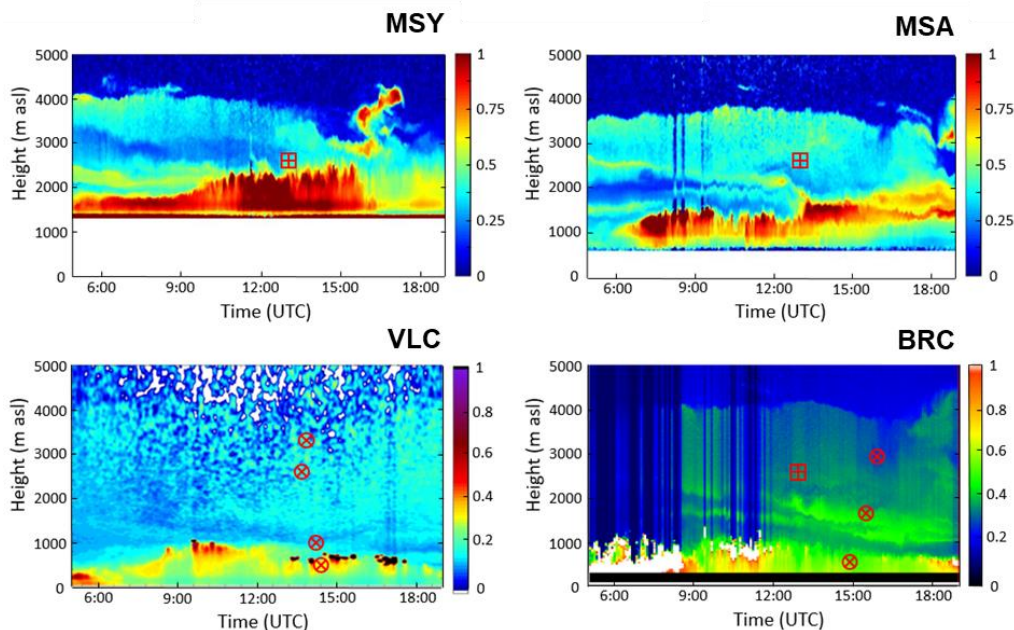


**Figure 25:** Time series of range-corrected lidar signals from ground-based remote sensing measurements in MSY, MSA (both at a wavelength of 1064 nm), VLC (910 nm) and BRC (532 nm) on the 28 July 2017. Depicted are the signal strengths relative to the maximum signal of the corresponding measurement. Red circles show time and altitude of the HALO overpasses used for the comparison of airborne with ground-based remote sensing measurements (see Fig. 26 and Fig. 27). Red squares show further HALO overpasses.

The composition of PM<sub>1</sub> particles (i.e., with diameter up to 1  $\mu\text{m}$ ) was retrieved from the HALO in-situ measurements at different altitudes during the shuttles. The observed PM<sub>1</sub> composition near Burjassot is shown in Fig. 27. Although the ceilometer measurements refer to total aerosol and the in-situ data only to PM<sub>1</sub>, both revealed two distinct aerosol layers: a) a PBL below 1000 m altitude with enhanced concentrations of sulphate

970 and ammonium and a backscatter coefficient between 2.0 and 2.7 ( $\text{Mm}\cdot\text{sr}^{-1}$ ), and b) a lofted aerosol layer  
 971 between 1500 and 3500 m altitude with higher organic, nitrate and BC mass fraction. The difference in  
 972 composition is likely related to different aerosol sources. While the boundary aerosol layer had a local origin, the  
 973 lofted aerosol layer was influenced by the transport of regional emissions. This is consistent with the transport of  
 974 the MPC Madrid outflow as indicated in Fig. 23.

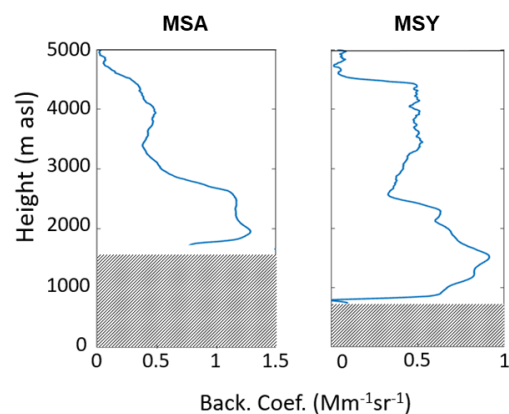
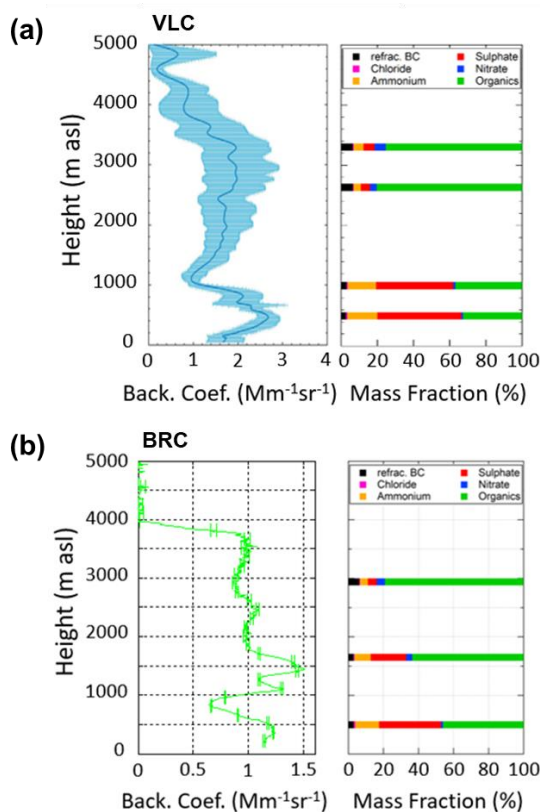


**Figure 26:** Profiles of the backscatter coefficient derived at 1064 nm in MSA and MSY for the 28 July 2017 from 12:50 to 13:20 UTC. The grey shadings indicate the height of the ceilometers.

979 | Similarly, the lidar and in-situ measurements close to Barcelona revealed a different aerosol composition of the  
 980 PBL below 900 m and a lofted aerosol layer above 2000 m. In addition, a third aerosol layer evolved between  
 981 1000 and 1800 m altitude with a backscatter coefficient up to  $1.5 (\text{Mm}\cdot\text{sr}^{-1})$ . The mass fractions of ammonium,  
 982 sulphate and organic aerosol are between the values of those of the PBL and of the lofted aerosol layer above.  
 983





984

985 **Figure 27:** Distinct aerosol layers observed near Burjassot/Valencia (VLC) and Barcelona (BRC). a) Profile of the  
 986 backscatter coefficient derived at 910 nm for 13:30-14:30 UTC in VLC (left), and fractional composition of PM1 measured  
 987 (SP2 and AMS) on-board HALO (right), b) the same derived in BRC at 532 nm for 14:45-15:45 UTC. The periods of  
 988 comparison with the HALO data are 13:42-13:56 (9:30 min) at 3300 m; 13:34-13:40 (5:30 min) at 2630 m, 14:03-14:14  
 989 (11:30 min) at 1000 m and 14:18-14:31 (23 min) at 500 m for VLC, and 15:43-16:00 (17:30 min) at 2940 m; 15:16-15:40  
 990 (24 min) at 1650 m, and 14:47-15:14 (27 min) at 500 m for BRC.

#### 991 4.4 Mixing of MPC outflows with air masses of biogenic and natural origin: forest fires and dust

992 • Plumes of anthropogenic, biogenic and natural origin were often mixed in the air probed over Europe  
 993 during the EMerGe IOP.

994 • The BB contribution of fresh wildfires in the Mediterranean area was substantial as indicated by VOCs, in  
 995 particular  $\text{CH}_3\text{CN}$ , and aerosol observations. For particles emitted from BB, a frequently used tracer is  
 996 levoglucosan which is identified using the  $m/z$  60 ion ( $\text{C}_2\text{H}_4\text{O}_2^+$ ) in aerosol mass spectrometry (Schneider et al.,  
 997 2006; Alfara et al., 2007). However, the photochemical degradation of levoglucosan is fast in summer  
 998 (Hennigan et al., 2010, 2011; Lai et al., 2014), and in the BB aerosol observed during the IOP in Europe ~~flight~~  
 999 ~~tracks it~~ was generally processed too fast to be distinguished from other secondary aerosol.

1000 A more robust indicator for particles from BB is BC. BC particles are formed in processes of incomplete  
 1001 combustion, and ~~are~~ therefore ~~are~~ an important component of both BB and urban aerosol particles (Bond et al.,  
 1002 2013). The microphysical properties of BC give insights into the combustion sources and atmospheric ageing  
 1003 time of the pollution plumes (Liu, 2014; Laborde, 2012; ~~Holanda et al., in preparation 2021~~). Figure 28 shows an  
 1004 example of average BC mass size distributions encountered during the E-EU-06 flight. A complex mixing of

Formatiert: Schriftart:

Formatiert: Ebene 2, Nicht vom  
nächsten Absatz trennen, Diesen Absatz  
zusammenhalten

Formatiert: Keine Aufzählungen oder  
Nummerierungen

Formatiert: Keine Aufzählungen oder  
Nummerierungen, Tabstopps: 0.5 cm,  
Links

different open BB sources with lightly aged BB smoke from fires in Croatia was observed. Grassland and fires in Italy mostly from mixed forests and savannahs were the dominant combustion fuel. The plumes were classified according to the VOC observations (see S12). This complex mix of biomass burning (BB, core diameter ( $D_c$ ) = 200 nm) BC sources, ~~got-mixed~~ occasionally ~~further-mixed~~ with anthropogenic emissions (BB+AP,  $D_c$  = 210 nm). Rather pure anthropogenic urban haze (AP) with significantly smaller mean modal diameter ( $D_c$  = 170 nm) was additionally measured. The resulting sizes agree with literature values for urban haze and BB smoke (e.g. Schwarz et al., 2008; Laborde et al., 2013; Liu et al., 2020; Holanda et al. 2020). During E-EU-06, the average total BC mass concentration was also substantially higher in relatively pure BB smoke and in the mixed conditions with urban haze (BB,  $0.61 \pm 0.12 \mu\text{g m}^{-3}$  and BB+AP,  $0.81 \pm 0.35 \mu\text{g m}^{-3}$ , respectively) than in urban pollution (AP,  $0.35 \pm 0.15 \mu\text{g m}^{-3}$ ).

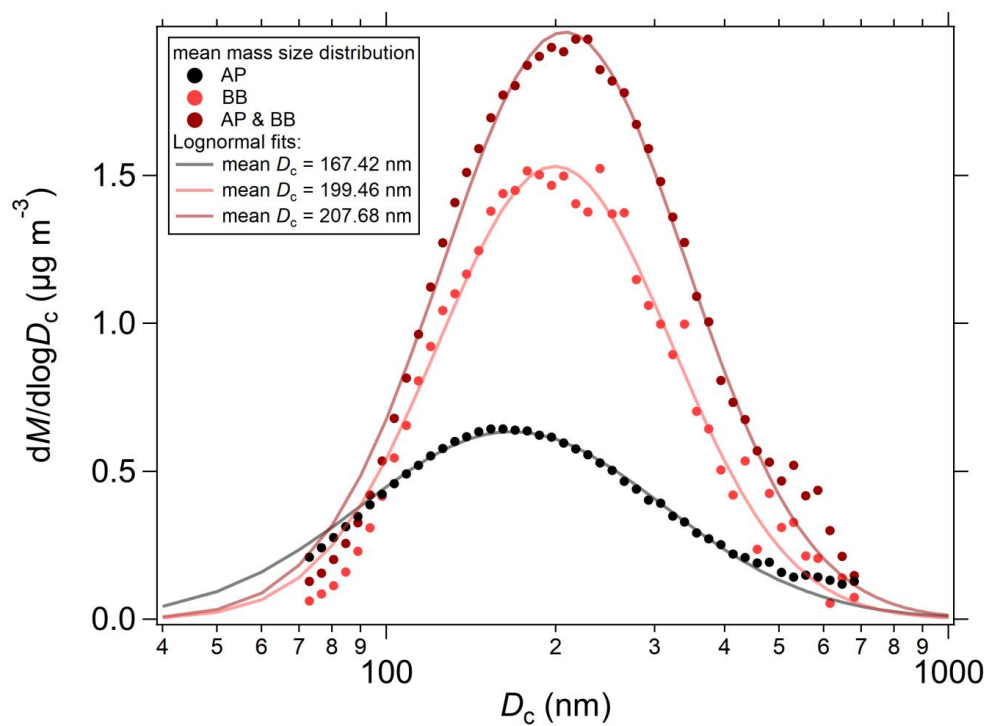


**Figure 28:** Mean mass size distribution of black carbon particles measured in anthropogenic pollution (AP, black), BB (light red), pollution from anthropogenic/ BB mix (AP & BB, dark red) during E-EU-06 on 20 July 2017.  $D_c$ : refractive black carbon core diameter. Lognormal fits were applied to the mean size distributions for  $100 < D_c < 300$  nm.

Mineral dust events contributed significantly to some of the plumes measured over Europe during the EMerGe IOP. Mineral dust was identified in the aerosol size distribution and the optical properties of air masses probed in Southern Europe above the PBL. An example of the ~~observed~~ impact of dust on the aerosol size distributions ~~observed~~ close to the western coast of Italy is illustrated in Fig. 29. The concentration of particles with a diameter below 250 nm was analysed by the Differential Mobility Analyzer (DMA) in 6 steps of 30 s duration, resulting in a period of 3 minutes for each integrated measurement. The evaluated DMA data were then combined with the data from an Optical Particle Counter (OPC) for particles in the range from 0.25 to 3  $\mu\text{m}$ . The first two sequences in Fig. 29 are taken

**Formatiert:** Keine Aufzählungen oder Nummerierungen, Tabstopps: 0.5 cm, Links

at 2900 m and the third at 1300 m altitude during E-EU-03. The third period and lowest in altitude had the smallest total number concentration with a clear enhancement of the particles above 600 nm. According to FLEXTRA, HALO flew approximately 800 m above the PBL at the time of sampling. The increase in the coarse mode particles above the PBL implies mineral dust rather than sea salt. According to backward trajectories, the air mass probed had recent contact at altitudes below 1000 m with the dust plumes over the Mediterranean near Sardinia. In fact, both satellite- and ground-based observations indicated a Saharan dust event affecting the Central Mediterranean air masses measured during E-EU-03 on 11 July 2017—(see Fig.32 and the discussion below).

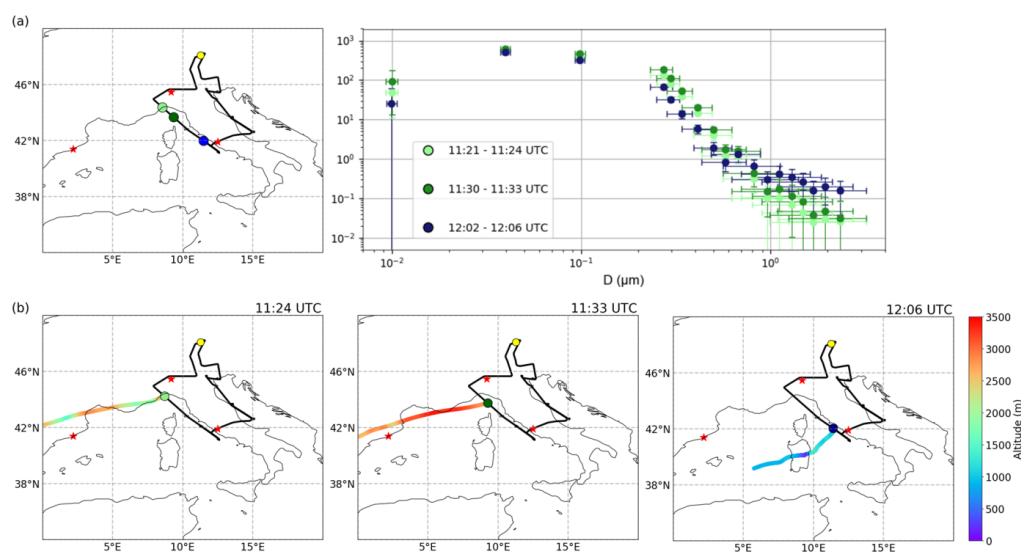
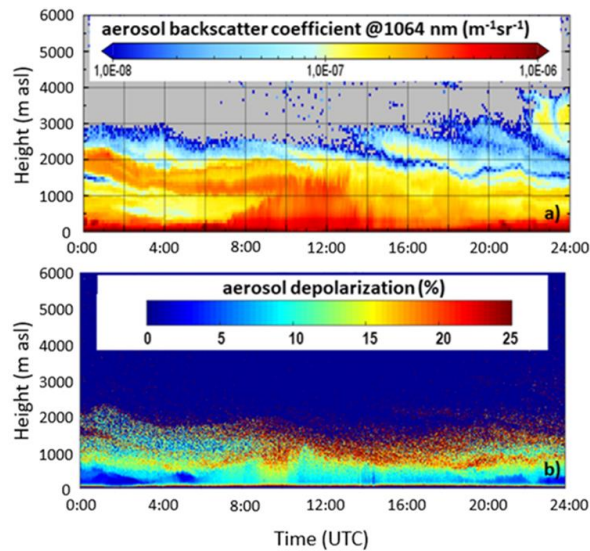


**Figure 29:** Example of the effect of dust plumes on the aerosol concentration during E-EU-03 on the 11 July 2017. a) Particle size distribution for 3 selected time periods (right) and position of the sample points in the flight track (left). The error bars on the y-axis are the standard deviations of the mean measured concentrations. The error bars in x-direction indicate the 16th and 84th percentile of the median diameters of the sensitivities of each size channel, b) 48h backward trajectories for the three periods selected. The red stars and the yellow dot indicate the position of the MPCs of interest and of the HALO base (OP), respectively.

The presence of mineral dust on 11 July 2017 is also confirmed by the continuous aerosol profile measurements made over Rome by the automated lidar-ceilometer (ALC)—HALO overpassed the Rome area around midday. Figure 30 shows a lofted aerosol layer with increased depolarization indicative of the non-spherical mineral particles, at an altitude between 1000 and 2000 m from the morning. This layer then vertically mixed with local particles lifted by the PBL dynamics in the middle of the day, at the time of the DMA measurement. This indicates that HALO flew above a dust layer during the first two time-periods of the DMA measurement, thus probing rather low concentrations of large particles. Subsequently, in the time-period 3, HALO dived into the dust layer and this explains the increase of particles larger than 600 nm in the DMA measurements. Additionally to the coarse mineral particles, aerosol properties observed over Rome both on board the Sky Arrow aircraft and at the ground provide evidence for an important role of fine particle photo-nucleation in the MPC Rome,

1056 favoured by high radiation and temperatures (Campanelli et al., 2021,2022; Barnaba et al., 2021–2022in  
1057 preparation).



1058  
1059 **Figure 30:** Aerosol profile measurements performed in Rome (Italy) on 11 July 2017 by the Automated Lidar-Ceilometer  
1060 network (ALICENET). Aerosol backscatter coefficient ( $\text{m}^{-1} \text{sr}^{-1}$ ) at 1064 nm (top), and aerosol depolarization in % (bottom).  
1061  
1062 • The Transport of BB emissions from fires and mineral dust events were was identified by combining HALO  
1063 observations with remote sensing satellite retrievals.  
1064 BB emission from fires was e.g. probed during the E-EU-07 flight downwind of Marseille. The plume transport  
1065 eastwards from near Marseille is well-captured by SEVIRI with AOT values around 0.25 at  $0.55 \mu\text{m}$  in the  
1066 afternoon, as shown in Fig. 31. This plume was probed by HALO in-situ measurements at around 11:30 and  
1067 16:30 UTC. The BC mass concentrations depicted in the figure agree with the satellite data. The highest BC was  
1068 measured at roughly 2000 m and exceeded  $7 \mu\text{g m}^{-3}$ . In the PBL, measured BC mass concentrations were as high  
1069 as  $1 \mu\text{g m}^{-3}$ . The stratification of pollution plumes above the PBL is a commonly observed feature for BB  
1070 emissions (Holanda et al., 2020).  
1071

Formatiert: Hochgestellt

Formatiert: Hochgestellt

Formatiert: Keine Aufzählungen oder Nummerierungen, Tabstopps: 0.5 cm, Links

Formatiert: Tabstopps: 0.5 cm, Links

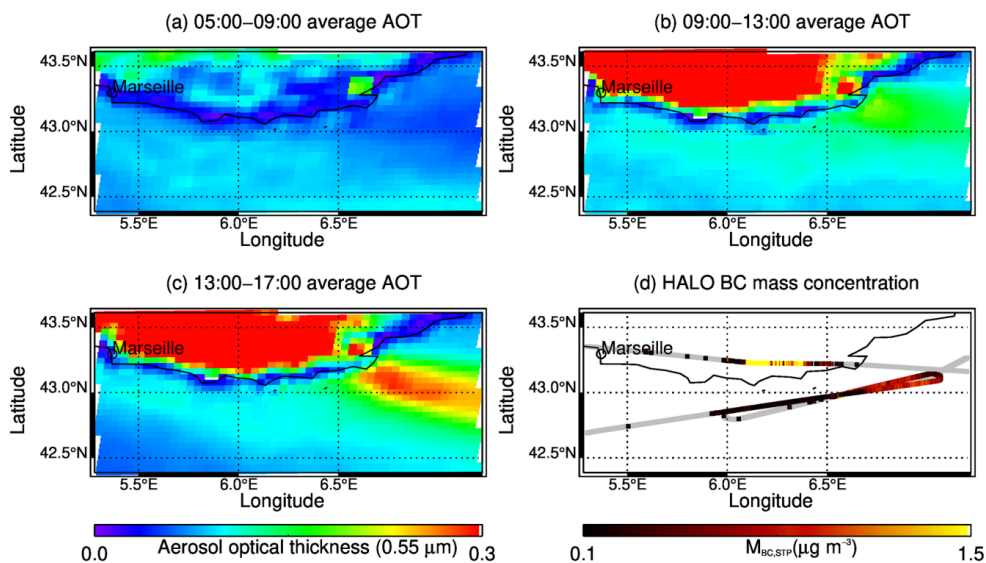


**Figure 31:** (a – c) Aerosol optical thickness at  $0.55 \mu\text{m}$  as retrieved from SEVIRI from 05:00 to 17:00 UTC on 24 July 2017. (d) E-EU-07 flight track, colour-coded with BC mass concentration ( $M_{\text{BC}}$ ). For a better contrast, the scale for  $M_{\text{BC}}$  ranges from  $0.1$  to  $1.5 \mu\text{g m}^{-3}$ . Grey colour on the flight track indicates values below  $0.1 \mu\text{g m}^{-3}$ . The mass concentration reached values up to  $7 \mu\text{g m}^{-3}$  at the French coast.

A further example is the transport of the Saharan dust event affecting the air masses measured during E-EU-03 on 11 July 2017 as explained in Fig. 29. Figure 32 shows the MODIS satellite RGB image at 10:30 UTC and the corresponding dust-related elevated AOT at  $0.55 \mu\text{m}$  as retrieved from SEVIRI from 09:00 to 13:00 UTC.

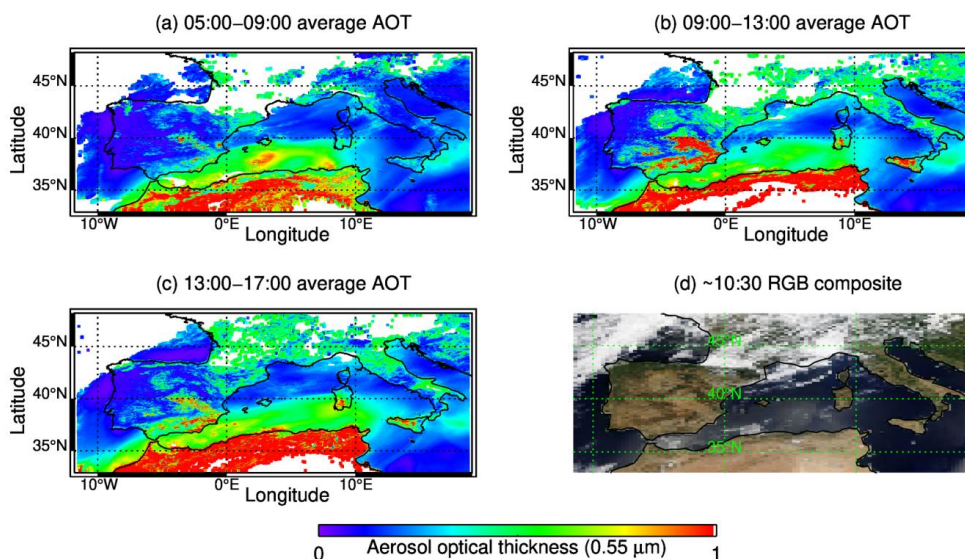


**Figure 32:** (a-c) Aerosol optical thickness at  $0.55 \mu\text{m}$  as retrieved from SEVIRI from 05:00 to 17:00 UTC on 11 July 2017, (d) MODIS RGB composite figure showing corrected reflectance at 10:30 UTC (<https://worldview.earthdata.nasa.gov/>). The MODIS RGB composite is created combining red, green and blue bands into one picture. White areas are clouds. The E-EU-03 flight track (in red) is superimposed on (d).

#### 4.5 Photochemical processing of polluted air masses during transport

Photochemical processing of the MPC emissions during transport was substantial during EMeRGe as inferred from airborne observations of primary and secondary pollutants and the ratios between species having different chemical lifetime:

a) The **NO to NO<sub>y</sub> ratio** provided information about the reactivity of the air mass but was not a reliable chemical clock due to the complex and rapid chemistry involved in the air masses investigated. Depending on the chemical and physical conditions, the lifetime of NO versus the formation of other reactive nitrogen compounds was of the order of a few hours or less. Internal transformation processes within the family of total reactive nitrogen NO<sub>y</sub> do not alter their integrated concentration. However, the lifetime of NO<sub>y</sub>, which varies between hours and days, is also controlled by loss processes such as washout and aerosol formation.

b) The **NO<sub>y</sub> to CO ratio** was generally significantly higher for the processed polluted plumes than for the background air masses. For instance, during E-EU-08 the NO<sub>y</sub> to CO ratio was of the order of 0.01 to 0.02 in the air sampled outside the outflow of London and increased up to 0.1 in the London outflow plumes, as the air mass was processed and mixed. This ratio is usually used to study ageing of an air mass with respect to ozone and nitrogen chemistry (e.g. Stohl et al., 2002). The CO lifetime varies between several weeks and months (e.g. Emmons et al., 2010) and the NO<sub>y</sub>/CO ratio is expected to decline to background values within a few days, depending on the distance from the source as well as on the chemical and physical properties of the air mass.

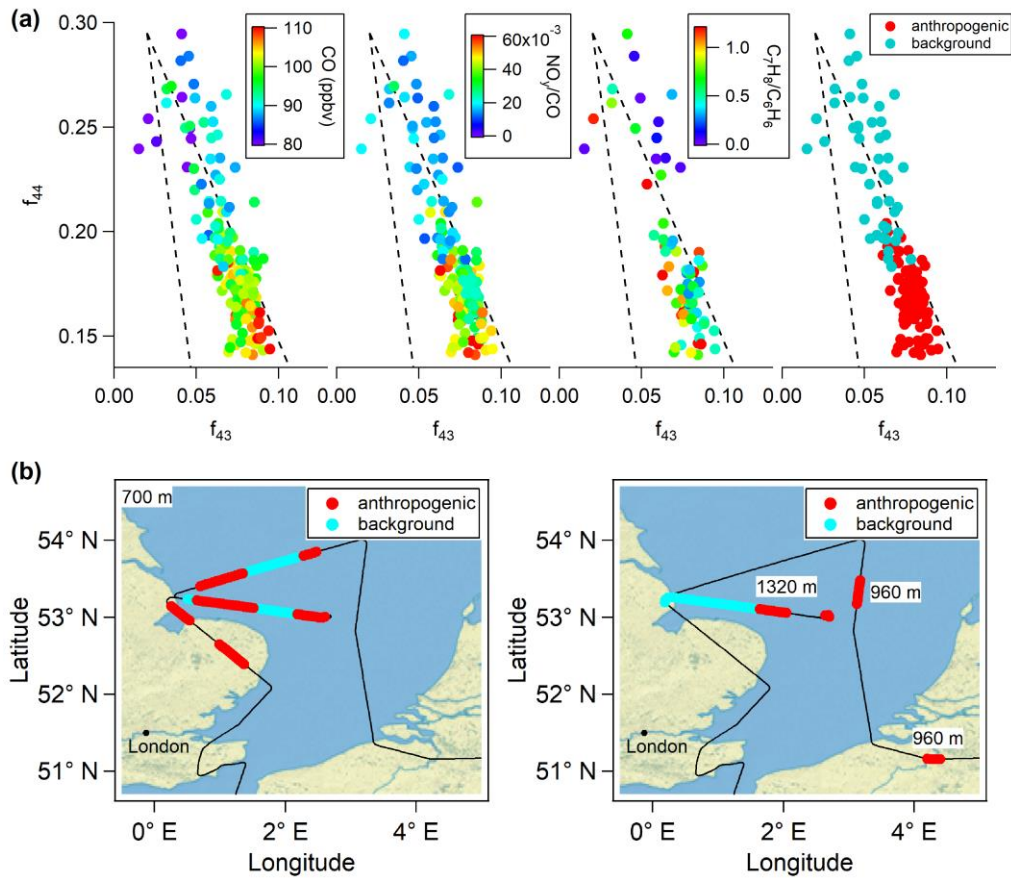
c) The ratio between **VOCs** with comparable emission sources but significantly different chemical lifetimes such as C<sub>7</sub>H<sub>8</sub>/C<sub>6</sub>H<sub>6</sub> was a good indicator for the presence of freshly or already processed anthropogenic emissions in the probed air within EMeRGe (Förster et al., 2022). This ratio is often used as a chemical clock to study emissions from gasoline-powered engines ~~used infor~~ traffic and industry (Gelencsér et al., 1997; Shaw et al., 2015; Warneke et al., 2001). The atmospheric lifetime of these aromatic hydrocarbons, i.e., 1.9 and 9.4 days, respectively (Garzón et al., 2015), is assumed to be controlled only by the reaction with OH radicals (Atkinson, 2000). Provided that the emission rates are known, the C<sub>7</sub>H<sub>8</sub>/C<sub>6</sub>H<sub>6</sub> ratio is expected to decrease with increasing distance to the pollution source and can be used to estimate the photochemical age of the sampled air (Winkler et al., 2002; Warneke et al., 2007). However, the complex plume mixing before sampling and potential variations in the emission ratios of distinct VOC sources (e.g. Barletta et al., 2005) limited the use and feasibility of this chemical clock for the determination of the transport time of specific outflows in EMeRGe.

d) The combination of **C<sub>7</sub>H<sub>8</sub>/C<sub>6</sub>H<sub>6</sub> and NO<sub>y</sub>/CO ratios** with the simultaneous observations of **CO and organic ions in aerosol particles** enabled the discrimination of dilution and processing in the plumes. Figure 33 shows an example of photochemical processing of the gas and the aerosol phases in ageing London plumes as measured by the C-ToF-AMS during E-EU-08. Aerosol mass spectrometer data using organic ions containing oxygen, e.g. CO<sub>2</sub><sup>+</sup> (m/z 44) and C<sub>2</sub>H<sub>3</sub>O<sup>+</sup> (m/z 43), were used to assess photochemical oxidation. Observations from laboratory and field studies indicate that during photochemical processing the ion signal of m/z 43 decreases while that of m/z 44 increases (Ng et al., 2010; Lambe et al., 2011). This metric is used to infer the degree of photochemical processing of organic aerosol in the atmosphere (e.g., Ng et al., 2011; Schroder et al., 2018; de Sa et al., 2018). The data in Fig. 33 are plotted in *f*<sub>44</sub>-*f*<sub>43</sub> space, where *f* denotes the ratio of the respective ion to the total organic ion signal. In these metric, atmospheric processing moves the data points towards the upper left corner of the triangle indicated by the dotted lines (Ng et al., 2010). Since photo-oxidation of fresh plumes is fast and mixing of aged plumes with the background occurs, the use of aerosol composition to assess photochemical processing requires complementary information from other measurements to be reliable.

**Formatiert:** Keine Aufzählungen oder Nummerierungen



1127 This is achieved by using simultaneous measurements of CO to indicate dilution, while inferring atmospheric  
 1128 processing from the  $C_7H_8/C_6H_6$  and  $NO_y/CO$  ratios. Lower CO concentrations due to plume dilution along  
 1129 transport correspond to higher photochemical processing in the upper part of the triangle. As  $NO_y$  has a shorter  
 1130 lifetime than CO, the  $NO_y/CO$  ratio indicates that the processing is taking place in addition to dilution.  
 1131 Therefore, lower  $NO_y/CO$  and  $C_7H_8/C_6H_6$  ratios in the upper part of the triangle indicate aged and processed air.  
 1132 In the case shown, the FLEXTRA backward trajectories revealed that the air masses identified as “background”  
 1133 were transported above the PBL and had no recent contact to the MPC London. The anthropogenically  
 1134 influenced air masses were a mixture of recent emissions and photochemically processed London outflow as  
 1135 mentioned in 4.3 (see also Fig. 36).



1136  
 1137 **Figure 33:** a) Scatter plots of C-ToF-AMS signal fractions at  $m/z$  44 ( $f_{44}$ ) and  $m/z$  43 ( $f_{43}$ ) of the London plume measured  
 1138 during the E-EU-08 on 26 July 2017 between 10:20 and 12:57 UTC. In this metric, the degree of photochemical processing  
 1139 increases to the upper left corner of the triangle which encompasses the range of typical atmospheric observations. The  
 1140 colour code indicates dilution (CO) and processing of the gas phase ( $NO_y$  to CO and  $C_7H_8$  to  $C_6H_6$  ratios). The right panel  
 1141 shows the assignment to unpolluted background air and air masses of anthropogenic polluted origin as introduced in Sect.  
 1142 4.2. b) Spatial distribution of the background and anthropogenic polluted air masses identified in a). The flight altitudes are  
 1143 indicated in the graphs.

1144 Photochemical processing of aerosol was evident during the transport of MPC plumes. Chemical processing was  
 1145 fast under European summer conditions and modified both the chemical properties and the partitioning between  
 1146 gas and particle phase in the air masses over Europe. The aerosol composition and mass loadings were to a large  
 1147 degree determined by the atmospheric dynamics, i.e. mass concentrations in the PBL were generally higher than

above, and most of the MPC plumes were found to reside in the PBL. However, anthropogenically influenced air masses above the PBL were found to also contain higher aerosol mass concentrations than air masses not influenced by anthropogenic emissions. Plume air contained less oxygenated organic aerosol, but the transition to background air conditions was smooth, indicating that the aerosol oxidation was faster than the decay of benzene which was used for the plume tagging.

The photochemical activity as indicated by the presence of free radicals varied widely in the plumes. The  $\text{RO}_2^*$  mixing ratios observed in EMeRGe are shown in Fig. 34. The  $\text{RO}_2^*$  measured is the sum of  $\text{HO}_2 + \sum \text{RO}_2$ , R being an organic chain which produces  $\text{NO}_2$  in its reaction with  $\text{NO}$ . Mixing ratios up to 120 pptv  $\text{RO}_2^*$  were measured in the air masses probed. Provided that insolation conditions (i.e. actinic fluxes) and the amount of precursors are similar, peroxy radicals are expected to be produced as long as plumes mix at any altitude. Generally, higher  $\text{RO}_2^*$  were measured below 45°N and 3000 m. This was in part due to the higher insolation and temperatures prevailing during the flights over the Mediterranean area, which accelerated photooxidation and the production of  $\text{RO}_2^*$ . Rates of photochemical production and loss of  $\text{HO}_2$  and  $\text{RO}_2$  were estimated by using airborne measurements and photostationary steady state calculations. In particular the measured photolysis frequencies are important to quantify the primary production of radicals and to elucidate the radical budget based on the measured  $\text{RO}_2^*$  concentrations. Overall, measured and estimated radical concentrations are in good agreement (George et al., 2021, in preparation 2022). Up to 4000 m,  $\text{O}_3$  photolysis was found to be the primary radical source (> 40 %) followed by  $\text{HCHO}$  photolysis in the air masses probed.  $\text{HONO}$  and  $\text{HNO}_3$  formation and heterogeneous losses on the aerosol surface dominated the peroxy radical losses in the polluted plumes encountered. The  $\text{O}_3$  production rates calculated from the  $\text{RO}_2^*$  measured on-board are consistent with the values reported in urban pollution for  $\text{NO} < 1$  ppbv (e.g. Tan et al, 2017; Whalley et al, 2018, 2021).

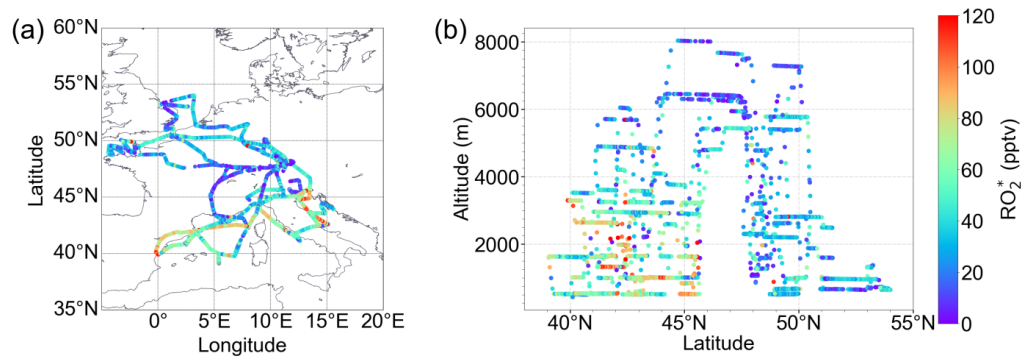


**Figure 34:**  $\text{RO}_2^*$  spatial and vertical distribution measured along all EMeRGe flights in Europe.

During the EMeRGe IOP, the secondary photochemical formation of formic acid ( $\text{HCOOH}$ ) was observed to be the main source of  $\text{HCOOH}$  in Europe, in pollution plumes of major cities aged 24 to 48 hours. Figure 35 shows  $\text{HCOOH}$  enhancements above ambient background relative to  $\text{CO}$  enhancements in different MPC plumes as a function of plume age. Here,  $\Delta\text{HCOOH}$  and  $\Delta\text{CO}$  are determined from the measurements, and the plume age from HYSPLIT simulations considering  $\text{CO}$  emissions from EDGAR and the dispersion of the plumes during transport.  $\text{CO}$  is used as an indicator of the strength of emissions from combustion in the individual MPC plumes and as tracer for the dilution of the plumes for the meteorological conditions during the measurements. Although  $\text{HCOOH}$  has primary sources, i.e., the emissions by fossil fuel combustion and BB, the

**Formatiert:** Keine Aufzählungen oder Nummerierungen, Tabstopps: 0.5 cm, Links

**Formatiert:** Tabstopps: 0.5 cm, Links

secondary formation from gas-phase and aqueous photochemistry has been suggested to be dominant in the troposphere (Paulot et al., 2011). The  $\Delta\text{HCOOH}$  to  $\Delta\text{CO}$  ratios in Fig. 35 increase significantly with plume age indicating secondary formation of HCOOH to be the main source in the MPC plumes, mainly due to oxidation of  $\text{C}_5\text{H}_8$  in the plume.

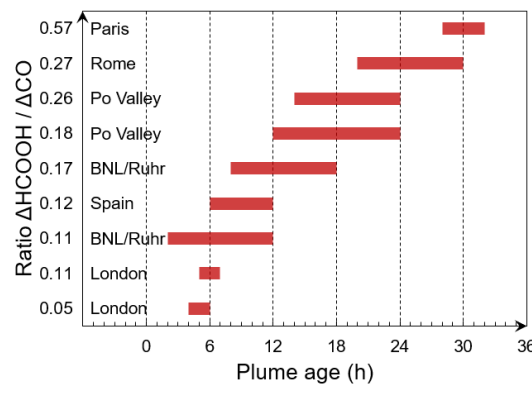


**Figure 35:** Observed enhancements of formic acid ( $\Delta\text{HCOOH}$ ) in MPC plumes relative to observed CO enhancements ( $\Delta\text{CO}$ ) as a function of plume age from HYSPLIT simulations. The corresponding city-plume is indicated next to the ratios.

Chemical ageing of MPC plumes was additionally assessed from the isotope measurements in VOC samples collected at MPC ground sites and on-board HALO. Figure 36 shows an example of the measured  $\delta^{13}\text{C}$  values of  $\text{C}_5\text{H}_{10}\text{O}$  and  $\text{C}_6\text{H}_6$  observed during the flight E-EU-08. Low carbon isotope ratios indicate fresh emissions, whereas higher values indicate an enrichment of the compound in  $^{13}\text{C}$ , which is linked to chemical ageing. The identified London outflow in Sect.4.3 is also evident in the carbon isotope ratios obtained from HALO samples taken between 10 and 11 UTC. The latter remain in the range of the representative source values from whole air samples collected at the ground station in London. The higher  $\delta^{13}\text{C}$  values observed between 11:10 and 12:00 UTC indicate chemically-processed London outflow air. Later in the flight, the  $\delta^{13}\text{C}$  values measured over the BNL/Ruhr area are in the range of the source values in air samples collected in Wuppertal. The range in  $\delta^{13}\text{C}$  values of  $\pm 1.5 \text{ ‰}$  in  $\text{C}_5\text{H}_{10}\text{O}$  ( $\pm 3.5 \text{ ‰}$  in  $\text{C}_6\text{H}_6$ ) implies a mixture of slightly aged air and rather fresh emissions from the Ruhr area.

**Formatiert:** Keine Aufzählungen oder Nummerierungen, Tabstopps: 0.5 cm, Links

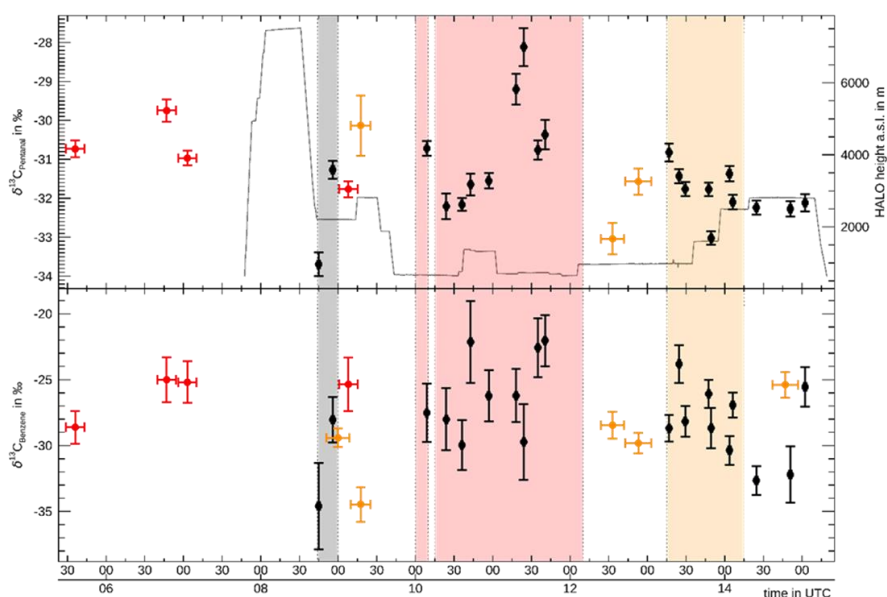


**Figure 36:**  $\delta^{13}\text{C}$  values in  $\text{C}_5\text{H}_{10}\text{O}$  (top panel) and  $\text{C}_6\text{H}_6$  (bottom panel) in whole air samples gathered with the whole air sampler MIRAH on the HALO aircraft (black) during E-EU-08 as well as on the ground sites in London (red) and Wuppertal (orange). The HALO flight altitude is given in grey on the top panel. Background shadings indicate different measurement regions during the flight according to Fig. 4: Paris (grey), South of London and North Sea region (red), BNL/Ruhr (orange).

#### 4.6 Model simulations of EMERGE observations

First results of the global/regional chemistry-climate MECO(n) model (Kerkweg & Jöckel 2012, Mertens et al., 2016) indicated that the emissions of  $\text{NO}_x$  and/or their further processing in the model (deposition, washout, chemical transformation) reasonably agree with the HALO measurements. However, the simulation of complex plume structures would benefit from a higher model spatial resolution.

An example is given in Fig. 37 for the E-EU-05 flight on 17 July 2017, when the London plume was probed over the English Channel. The MECO(n) model (Kerkweg & Jöckel 2012, Mertens et al., 2016) couples a global and a regional chemistry climate model. In the set-up applied here, Central Europe was resolved with up to 7 km horizontal resolution. The model data was sampled along the HALO flight paths with 60 s temporal resolution using the MESSy submodel S4D (Jöckel et al., 2010). These sampled model data are used for a one-by-one comparison with the measurements. The EDGAR 4.3.1 emission inventory for the year 2010 was used (see S15).

The enhancements of  $\text{NO}_x$  between 12 and 16 UTC below 900 hPa in Figure 37a are reasonably well simulated by the model except for the measurements at around 15:30 UTC which are strongly overestimated by the model. To address this issue, two plumes marked with ‘1’ and ‘2’ in Fig. 37a were investigated in more detail. The model results and the measurements on the plume marked ‘1’ are shown at 980 hPa and 965 hPa in Fig. 38a. 980 hPa is the pressure of the model layer which is nearest to the HALO flight altitude at 13:30 UTC while 965 hPa is pressure of one model layer above. The model results show large horizontal and vertical inhomogeneities in the  $\text{NO}_x$  mixing ratios indicating different mixtures instead of a single London plume. The  $\text{NO}_x$  enhancement coincides with the London plume (marked with the turquoise square in Fig. 38a).

Formatiert: Tiefgestellt

Formatiert: Tiefgestellt

Formatiert: Tiefgestellt

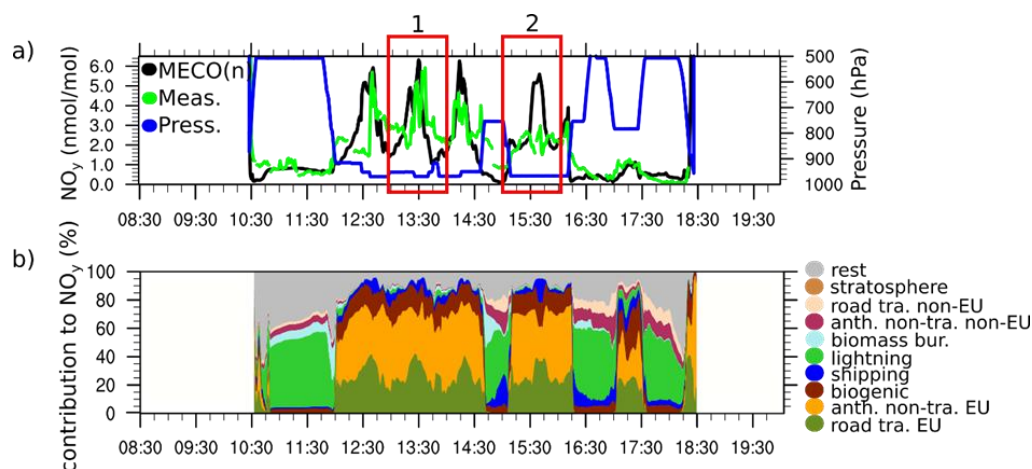


**Figure 37:** a) NO<sub>y</sub> mixing ratios measured (green) and simulated by the MECO(n) model (black) for E-EU-05 on 17 July 2017. The blue line denotes the pressure altitude of the aircraft (right axis). b) Relative contributions of different emission sectors to the NO<sub>y</sub> mixing ratios simulated by MECO(n). Note that the NO<sub>y</sub> measurements were averaged to 60 s to fit the MECO(n) temporal resolution.

Similarly, Figure 38b shows the model results and measurements for the plume marked '2'. Here, the model shows a large plume remnant in the western part (turquoise square in Fig. 38b) leading to the overestimation of mixing ratios around 15:30 UTC. The simulated mixing ratios in a higher model layer are lower and agree better with the observations. These results indicate that a vertical displacement of the plume remnant causes the mismatch between measurements and model results around 15:30 UTC.

MECO(n) results showed a positive bias in O<sub>3</sub> and a negative bias in CO with respect to the EMeRGe measurements over Europe. This confirms previous comparisons with other observational data (see Mertens et al., 2016, 2020b) and is investigated for EMeRGe in separate sensitivity studies focusing on the representation of the NO<sub>x</sub>-VOC-O<sub>3</sub> chemistry and the evaluation of the applied emission data sets.

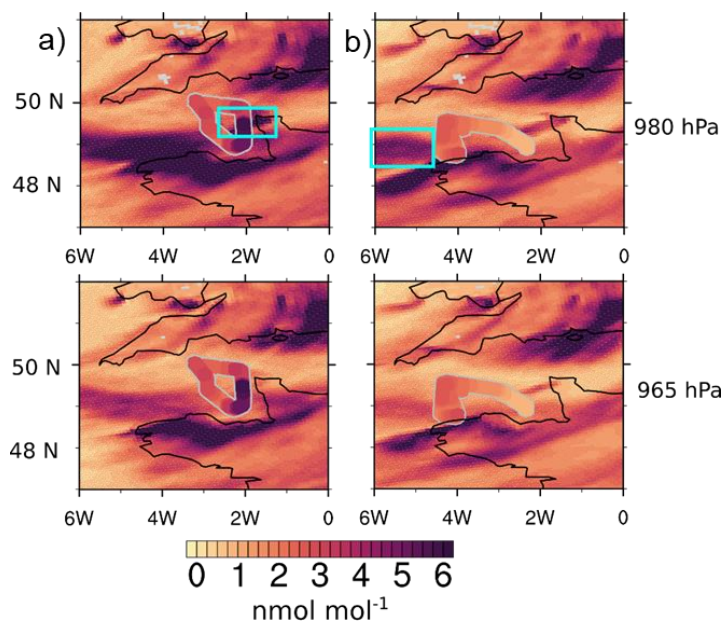


**Figure 38:**  $\text{NO}_y$  mixing ratios as simulated by MECO(n) (background) and measured during E-EU-05. The model results at 980 hPa and 965 hPa are shown. Model results are averaged between a) 13 and 14 UTC, b) 15 and 16 UTC. The measured mixing ratios of  $\text{NO}_y$  during 13-14 UTC and 15-16 UTC are colour-coded and highlighted by grey contours. Black lines indicate coast lines. The turquoise rectangles highlight the regions discussed in the text.

The diagnostic capabilities of MECO(n), e.g. the tagging method by Grewe et al., (2017), were applied to individual EMErGe flight tracks to investigate the impact of emissions on the atmospheric chemistry in Europe. Figure 37b shows the relative contribution of the different emission sectors to the measured  $\text{NO}_y$  mixing ratios during the E-EU-05 as a stacked graph. According to this, emissions from European road transport, anthropogenic non-traffic and biogenic sectors dominate the  $\text{NO}_y$  mixing ratios of the London plume with a similar relative contribution in all four plume crossings. For the  $\text{NO}_y$  measurements in the free troposphere (until 12 UTC approximately) a large relative contribution of lightning emissions is calculated in the model. In these regions, however, the absolute mixing ratios are rather low. As the  $\text{NO}_y$  lifetime is much longer in the upper troposphere than in the PBL, LRT of  $\text{NO}_y$  might be more likely than encounters of fresh lightning  $\text{NO}$ -plumes. A detailed description of the model and the source apportionment technique are provided in the supplement (S15).

• The tracer experiments during EMErGe additionally tested the ability of models (HYSPLIT, FLEXPART, FLEXPART-WRF, FALL3D) to simulate the transport and dispersion of the tracer for different meteorological conditions and topography around the release sites. While the simulated position of the PFC plumes agreed with the measurements, the tracer mixing ratios calculated by the dispersion models were by a factor 2 to 3 higher than detected. The degree of agreement between the tracer simulations and observations depended on the parametrisation of dispersion and the representation of the topography in the models, as well as the goodness of tracer sampling in the plume, e.g. matching the maximum PFC concentrations was not always possible due to restrictions by air traffic control and flight endurance. Sensitivity studies with different meteorological datasets (ECMWF's ERA5 and IFS) and advanced turbulence parametrisation options in the PBL highlighted the pivotal role of meteorological input data on transport simulations (Schlager et al., 2021, in preparation).

**Formatiert:** Keine Aufzählungen oder Nummerierungen, Tabstopps: 0.5 cm, Links



## 5 Outlook

EMeRGe contributes to the long history of providing observations facilitating a continuous and incremental progress in the capability to forecast and simulate atmospheric composition and chemistry. The interpretation of the extensive EMeRGe observational data set provides a clear step forward in understanding the complex spatial distribution of trace gases and aerosol particles resulting from mixing, transport and transformation of pollution plumes over Europe. The present work is an overview of the most salient results which are addressed in additional dedicated EMeRGe studies. The lessons learned from a continued analysis of the EMeRGe observations are also expected to be valuable to build upon and to improve airborne measurement strategies for future deployments focusing on pollution in Europe. First of all, the results of EMeRGe confirm the chemical complexity of the air masses over Europe as a result of the mixing of emissions from nearby MPC sources. EMeRGe airborne observations of primary and secondary pollutants and the ratios between species having different chemical lifetime were used as tracers of the degree of processing of the pollution plumes probed. The distinction between fresh and aged air was possible and gave a coherent picture for the applied methods and chemical clocks. However, high specific background measurements close to MPCs are needed, and following the ageing of the outflow of a single MPC is challenging. At large distances from the source, the use of gas and aerosol trace species is insufficient for unequivocally identifying MPC plumes. In this context, the relevance of PFC tracers and the support of adequate transport models become obvious. EMeRGe is one of the first airborne measurement campaigns using air mass tracer approaches and has successfully demonstrated its value. For future studies, sampling the same air mass inside a tagged MPC plume at several different aging states, either by following the air mass or by crossing the plume at different distances from the source, would be beneficial to investigate the atmospheric processing of trace gases and organic aerosol as a function of time. For this (quasi-) Lagrangian approach the combination with either a Zeppelin-based measurement platform or with a small, slow-flying aircraft might be suitable to cope with air traffic control restrictions, in particular for low level flights close to MPCs.

Satellite data have proven useful in assessing the overall pollution patterns and to put measurements during the campaign phase into a long-term perspective. For future campaigns, the new generation of geostationary air quality satellites, started with the Korean GEMS instrument providing data at hourly resolution, will enable detailed tracing of transport patterns and chemical evolution. For flight planning, satellite observations are best used in combination with models which provide forecasting capability. In the case of EMeRGe, the use of CAMS tracer and full chemistry forecasts facilitated the measurement of several pollution plumes. Subsequent comparisons to the measurements reflect the quality of the forecasts and support the improvement of future model runs. The total column AOT derived from geostationary satellites provided valuable information for the EMeRGe campaign. The integration of satellite total column AOT and model simulated aerosol extinction profile information enables further analysis of the component aerosol near the EMeRGe flight height. An important step to move further is the synergistically use of hyperspectral and multi-spectral satellite instruments for a better understanding of the aerosol component near the flight height and the component AOT (e.g. dust AOT, black carbon AOT).

An interesting aspect of EMeRGe is the high added value from measurements rarely used for the characterisation of urban pollution. In that sense, the measurement of stable carbon isotope ratios in VOC collected on the ground close to or at certain MPCs supported source apportionment and the estimation of integrated residence times of compounds in the air sampled on board HALO. EMeRGe has significantly expanded the very rare coverage of

stable carbon isotope data from different locations and atmospheric regions. This and future data sets are valuable to verify model results and to assess the physical and chemical processing of VOCs during transport. Similarly, the sparse in-situ data available for HCOOH has also been enhanced by EMeRGe. This major organic acid in the troposphere was found to be more abundant in MPC plumes than the sulphur and nitrogen precursor species of inorganic acids. The HCOOH production rates in the pollution plumes as a function of the plume ages during the EMeRGe IOP in Europe differ significantly to those encountered in Asia. Future studies are required to investigate sources and composition of organic compounds with respect to the effect on the formation and the properties of aerosols, clouds and acidity of precipitation in different seasons and for MPCs in different regions of the world. Furthermore, signatures of urban sources of long-lived GHG like CH<sub>4</sub> and CO<sub>2</sub>, identified in the airborne measurements in plumes close to the MPC regions in Europe, provided valuable insights on sources and expanded the knowledge on existing top-down studies by confirming urban emission hotspots. An accurate knowledge of GHG sources and sinks in MPCs establishes the link between air quality and climate change. In that respect, the impact of climate change (e.g. increasing number of fires, temperature effect on chemical processing, changes in radiation), and emission reduction strategies or the use of alternative fuels, on the composition and transformation of the outflows along transport requires increasing interest. For a more comprehensive picture, conducting dedicated local flight experiments complemented with coordinated ground-based GHG measurements on several days and in all seasons for the same area is highly desirable. This would show seasonal evolution and emission sources (e.g. residential biomass burning in winter), increase statistics and reinforce the findings.

Finally, the EMeRGe set of airborne data are particularly expected to support photochemical transport models in assessing:

- the relative contribution of biogenic, BB and anthropogenic sources to the VOC burden over Europe,
- the net ozone production in the investigated MPC outflows in relation to the transport time and mixing of the pollution plumes,
- the adequacy of radiative transfer model calculations and the prediction capabilities of photolysis frequencies,
- the contribution of VOC species such as glyoxal and/or methylglyoxal to secondary aerosol formation in aged pollution plumes,
- the adequacy of Angstrom coefficients, aerosol fine mode fraction products and the geostationary satellite derived AOT to identify aerosol sources and transport features of mixing events of anthropogenic particles and mineral dust, and
- the significance and representativeness of the transport and concentration patterns obtained during EMeRGe in summer 2017, which was a period with anomalous meteorological conditions in Central Europe.

#### 1338 **Data availability**

1339 The EMeRGe data are available at the HALO data base (<https://halo-db.pa.op.dlr.de/>) and can be accessed upon  
1340 registration. Further data can be made available upon request to the corresponding author.

## 1341 Acknowledgements

1342 The authors thank the following teams and individuals, without whom the EMeRGe in Europe IOP would not have been  
1343 possible:

1344 • HALO flight organisation, permissions and related  
1345 the DLR-FX and the HALO EMeRGe team. Special thanks to Lisa Kaser, Frank Probst, Michael Großrubatscher, Stefan  
1346 Grillenbeck, Marc Puskeiler, for flight coordination and planning, to Alexander Wolf, and Thomas Leder, the flight  
1347 engineers and to the BAHAMAS team. The authors also thank enviscope GmbH in particular of Nicole Brehm and Rolf  
1348 Maser for the support during the integration and preparation phase of the IOP in Europe.

1349 • Meteorological and chemical composition forecasting  
1350 Michael Gauss and Álvaro Valdebenito (MetNo) for provision of EMEP forecasts for the campaign and  
1351 CAMS/ECMWF, in particular Johannes Flemming and Luke Jones for providing the atmospheric composition and tracer  
1352 forecasts through the CAMS field campaign support ([https://atmosphere.copernicus.eu/scientific-field-campaign-](https://atmosphere.copernicus.eu/scientific-field-campaign-support)  
1353 [support](https://atmosphere.copernicus.eu/scientific-field-campaign-support)). The CAMS-regional modelling team are also acknowledged for providing regional model forecast data for  
1354 Europe.

1355 • Ground based remote sensing observations  
1356 EARLINET for providing aerosol LIDAR measurements and DWD, ALICE-net and RMI for ceilometer measurements.  
1357 The support from AERONET, Service National d'Observation PHOTONS/ AERONET-EARLINET part of the  
1358 ACTRIS-France research infrastructure and GOA-CF, part of ACTRIS-Spain, for their continuous efforts in providing  
1359 high-quality measurements and products, and in particular of all PIs and Co-PIs of the AERONET sites contributing to  
1360 EMeRGe for maintaining their instruments and providing their data to the community is greatly appreciated.

1361 • Luca Ferrero (GEMMA and POLARIS Research Centers, Department of Earth and Environmental Sciences, University  
1362 of Milano-Bicocca) for the air samples collected at the ground in Milan (Italy) during the HALO flights.

1363 • Tracer releases  
1364 Jonathan E. Murray and Helen Graven and the Imperial College team for releasing the PFC tracer in London.

1365 KK and JohS would like to thank Christiane Schulz and Philipp Schuhmann for support during the integration phase. BAH,  
1366 OOK, CP, DW, UP and MLP would like to thank Thomas Klimach, Björn Nilus, Jorge Saturno, Oliver Lauer and Meinrat  
1367 Andreae for support during the EMeRGe campaign in Europe and during the data analysis.

1368 MDAH, MG, YL and JPB thank Wilke Thomssen for support during the preparation and integration phases of EMeRGe and  
1369 Heiko Schellhorn for continuous technical support and retrieval of model data during the campaigns.

## 1370 Funding information

1371 The HALO deployment during EMeRGe was funded by a consortium comprising the German Research  
1372 Foundation (DFG) Priority Program HALO-SPP 1294, the Institute of Atmospheric Physics of DLR, the Max  
1373 Planck Society (MPG) and the Helmholtz Association.

1374 FK, BS, and KP acknowledge the support given by the DFG through the projects PF 384-16, PF 384-17 and PG  
1375 385-19. RK and MK acknowledge DFG funding through the project KR3861\_1-1. KB acknowledges additional  
1376 funding from the Heidelberg Graduate School for Physics. JohS, KK, and SB acknowledge funding through the  
1377 DFG, project No. 316589531. LE and HS acknowledge support by DFG through project MEPOLL  
1378 (SCHL1857/4-1). ABKH would like to thank DAAD and DLR for a Research Fellowship. HS acknowledge  
1379 financial support by the DLR TraK (Transport and Climate) project. MS acknowledges support from the EU  
1380 (GA no. 654109, 778349, 871115 and 101008004) and the Spanish Government (ref. CGL2017-90884-REDT,  
1381 PID2019-103886RB-I00, RTI2018-096548-B-I00 and MDM-2016-0600).

1382 MG, YL, MDAH and JPB acknowledge financial support from the University of Bremen. FLEXPART  
1383 simulations were performed on the HPC cluster Aether at the University of Bremen, financed by DFG within the  
1384 scope of the Excellence Initiative. A.-M. Blechschmidt was partly funded through the CAMS-84 project.

1385 JW acknowledges support from the German Federal Ministry for Economic Affairs and Energy – BMWi (project  
1386 Digitally optimized Engineering for Services – DoEfS; contract no. 20X1701B)

1387 TK thanks DLR VO-R for funding the young investigator research group “Greenhouse Gases”.

1388 MM, PJ, MK acknowledge resources of the Deutsches Klimarechenzentrum (DKRZ) granted by the WLA  
1389 project ID bd0617 for the MECO(n) simulations and the financial support from the DLR projects TraK  
1390 (Transport und Klima) and the Initiative and Networking Fund of the Helmholtz Association through the project  
1391 “Advanced Earth System Modelling Capacity” (ESM).

1392 BAH acknowledges the funding from Brazilian CNPq (process 200723/2015-4).

## 1393 References

- 1394 AERONET: AERONET aerosol data base, available at: <http://aeronet.gsfc.nasa.gov/>, last access: 11 December  
1395 2020
- 1396 Alfara, M. R., Prevot, A. S. H., Szidat, S., Sandradewi, J., Weimer, S., Lanz, V. A., Schreiber, D., Mohr, M., and  
1397 Baltensperger, U.: Identification of the mass spectral signature of organic aerosols from wood burning emissions,  
1398 Environ. Sci. Technol., 41, 5770–5777, doi.org/10.1021/es062289b, 2007.
- 1399 Alvarado, L. M. A., Richter, A., Vrekoussis, M., Hilboll, A., Kalisz Hedegaard, A. B., Schneising, O., and  
1400 Burrows, J. P.: Unexpected long-range transport of glyoxal and formaldehyde observed from the Copernicus  
1401 Sentinel-5 Precursor satellite during the 2018 Canadian wildfires, Atmos. Chem. Phys., 20, 2057–2072, 2020.
- 1402 Andreae, M. O., and Rosenfeld, D.: Aerosol–cloud–precipitation interactions. Part 1. The nature and sources of  
1403 cloud-active aerosols, Earth-Science Reviews 89, 13–41, 2008.
- 1404 Andreae, M. O., Afchine, A., Albrecht, R., Holanda, B. A., Artaxo, P., Barbosa, H. M. J., Borrmann, S.,  
1405 Cecchini, M. A., Costa, A., Dollner, M., Fütterer, D., Järvinen, E., Jurkat, T., Klimach, T., Konemann, T., Knote,  
1406 C., Krämer, M., Krisna, T., Machado, L. A. T., Mertes, S., Minikin, A., Pöhlker, C., Pöhlker, M. L., Pöschl, U.  
1407 Rosenfeld, D., Sauer, D., Schlager, H., Schnaiter, M., Schneider, J., Schulz, C., Spanu, A., Sperling, V. B.,  
1408 Voigt, C., Walser, A., Wang, J., Weinzierl, B., Wendisch, M., Ziereis, H.: Aerosol characteristics and particle  
1409 production in the upper troposphere over the Amazon Basin. Atmos. Chem. Phys., 18, 921–961, doi:  
1410 10.5194/acp-18-921-2018, 2018.
- 1411 Andreae, M. O.: Emission of trace gases and aerosols from biomass burning – an updated assessment, Atmos.  
1412 Chem. Phys., 19, 8523–8546, doi.org/10.5194/acp-19-8523-2019, 2019.
- 1413 Ashworth, K. et al, Megacity and local contributions to regional air pollution: an aircraft case study over  
1414 London, Atmos. Chem. Phys., 20, 7193–7216, doi:10.5194/acp-20-7193-2020, 2020.
- 1415 Atkinson, R.: Atmospheric chemistry of VOCs and NO<sub>x</sub>, Atmospheric Environment, 34, 2063–2101, 2000.
- 1416 Barnaba, F. and Gobbi, G. P., Aerosol seasonal variability over the Mediterranean region and relative impact of  
1417 maritime, continental and Saharan dust particles over the basin from MODIS data in the year 2001. Atmos.  
1418 Chem. . Phys., 4, doi:10.5194/acpd-4-4285-2004, 2004.
- 1419 Barnaba, F., Angelini, F., Curci, G., and Gobbi, G.P.: An important fingerprint of wildfires on the European  
1420 aerosol load, Atmos. Chem. Phys, 11, 10487–10501, doi: 105194/acp-11-10487-2011, 2011.
- 1421 [Barnaba F., Di Liberto L., Bellini A., Diemoz H., Campanelli, M., Shuli I., Gobbi G.P., Andrés Hernández,  
1422 M.D., and J.P.Burrows: The intricate summer mixing of atmospheric particles in an urban Mediterranean  
1423 environment: a 4D insight from airborne and and ground measurements in Rome \(Italy\) during EMeRGe,  
1424 Atmos. Chem., Phys., in preparation, 2022.](#)
- 1425 Beekmann, M., Prévôt, A. S. H., Drewnick, F., Sciare, J., Pandis, S. N., Denier van der Gon, H. A. C., Crippa,  
1426 M., Freutel, F., Poulain, L., Ghersi, V., Rodriguez, E., Beirle, S., Zotter, P., von der Weiden-Reinmüller, S.-L.,  
1427 Bressi, M., Fountoukis, C., Petetin, H., Szidat, S., Schneider, J., Rosso, A., El Haddad, I., Megaritis, A., Zhang,  
1428 Q. J., Michoud, V., Slowik, J. G., Moukhtar, S., Kolmonen, P., Stohl, A., Eckhardt, S., Borbon, A., Gros, V.,  
1429 Marchand, N., Jaffrezo, J. L., Schwarzenboeck, A., Colomb, A., Wiedensohler, A., Borrmann, S., Lawrence, M.,  
1430 Baklanov, A., and Baltensperger, U.: In situ, satellite measurement and model evidence on the dominant regional  
1431 contribution to fine particulate matter levels in the Paris megacity, Atmos. Chem. Phys., 15, 9577–9591,  
1432 <https://doi.org/10.5194/acp-15-9577-2015>, 2015. Beirle, S., Borger, C., Dörner, S., Li A., Hu, Z., Liu, F., Wang,  
1433 Y., Wagner, T.: Pinpointing nitrogen oxide emissions from space, Sci. Adv. 2019, 5, eaax9800 13 November  
1434 2019.
- 1435 Boeke, N. L., Marshall, J. D., Alvarez, S., Chance, K. V., Fried, A., Kurosu, T. P., Rappenglück, B., Richter, D.,  
1436 Walega, J., Weibring, P. and Millet, D.B.: Formaldehyde columns from the Ozone Monitoring Instrument:  
1437 Urban versus background levels and evaluation using aircraft data and a global model, J. Geophys. Res., 116,  
1438 D05303, doi:10.1029/2010JD014870, 2011.

1439 Bohn, B., and Lohse, I.: Calibration and evaluation of CCD spectroradiometers for ground-based and airborne  
1440 measurements of actinic flux densities, *Atmos. Meas. Tech.*, 10, 3151–3174, doi:10.5194/amt-10-3151-2017,  
1441 2017.

1442 Bond, T.C., Doherty, S.J., Fahey, D.W., Forster, P.M., Bernsten, T., DeAngelo, B.J., Flanner, M.G., Ghan, S.,  
1443 Kärcher, B., Koch, D., Kinne, S., Kondo, Y., Quinn, P.K., Sarofim, M.C., Schultz, M.G., Schulz, M.,  
1444 Venkataraman, C., Zhang, H., Zhang, S., Bellouin, N., Guttikunda, S.K., Hopke, P.K., Jacobson, M.Z., Kaiser,  
1445 J.W., Klimont, Z., Lohmann, U., Schwarz, J.P., Shindell, D., Storelvmo, T., Warren, S.G., and Zender, C.S.:  
1446 Bounding the role of black carbon in the climate system: A scientific assessment, *Journal of Geophysical*  
1447 *Research: Atmospheres*, Vol. 118, 5380–5552, doi: 10.1002/jgrd.50171, 2013.

1448 Brands, M., M. Kamphus, T. Böttger, J. Schneider, F. Drewnick, A. Roth, J. Curtius, C. Voigt, A. Borbon, M.  
1449 Beekmann, A. Bourdon, T. Perrin, and S. Borrmann: Characterization of a Newly Developed Aircraft-Based  
1450 Laser Ablation Aerosol Mass Spectrometer (ALABAMA) and First Field Deployment in Urban Pollution  
1451 Plumes over Paris During MEGAPOLI 2009, *Aerosol Sci. Technol.*, 45, 46–64, doi: 10.1080/02786826.2010.  
1452 517813, 2011.

1453 Bréon, F.M., Vermeulen, A., and Descloitres J.: An evaluation of satellite aerosol products against sun  
1454 photometer measurements. *Remote Sensing of Environment*, doi:10.1016/j.rse.2011.06.017, 2011.

1455 Bréon, F.M., Broquet, G., Puygrenier, V., Chevallier, F., Xueref-Remy, I., Ramonet, M., Dieudonné, E., Lopez,  
1456 M., Schmidt, M., Perrussel, O., and Ciais, P.: An attempt at estimating Paris area CO<sub>2</sub> emissions from  
1457 atmospheric concentration measurements, *Atmos. Chem. Phys.* 2015, 15 (4), 1707–1724. doi: 10.5194/acp-15-  
1458 1707-2015, 2015.

1459 Brito, J., and Zahn, A.: An unheated permeation device for calibrating atmospheric VOC measurements, *Atmos.*  
1460 *Meas. Tech.*, 4(10), 2143–2152, doi: 10.5194/amt-4-2143-2011, 2011.

1461 Burrows, J.P., Richter A., Dehn A., Deters B., Himmelmann S., Voigt S. and Orphal J.: Atmospheric remote  
1462 sensing reference data from GOME: Part 2 temperature dependent absorption cross-sections of O<sub>3</sub> in the 231–794  
1463 nm range, *Journal of Quantitative Spectroscopy and Radiative Transfer*, Volume: 61 Issue: 4, 509–517, 1999.

1464 Butler, T. M., and Lawrence, M. G.: The influence of megacities on global atmospheric chemistry: A modelling  
1465 study, *Environ. Chem.*, 6 (3), 219– 225. 2009.

1466 Butler, T.M., Stock, Z.S., Russo, M.R., Denier van der Gon, H.A.C., and Lawrence, M.G.: Megacity ozone air  
1467 quality under four alternative future scenarios. *Atmos. Chem. Phys.*, 12, 4413–4428, doi: 10.5194/acp-12-4413-  
1468 2012, 2012.

1469 Campanelli, M., Bassani, C., Iannarelli A.M., Casadio, S., Barnaba, F., Bigge, K., Wolf, J., Sauer, D., Hilboll  
1470 A., Cacciani, Mueller, M., Tiefengraber, M., Cede A., Perrino, C., Dionisi, D., Casasanta G., Andrés  
1471 Hernández, M.D., Burrows, J.P.: Gas and aerosol properties over Rome during EMeRGe flights from columnar  
1472 and profiling observations, Atmos. Chem., Phys., in preparation, 2022.

1473 Campos Braga, R., Rosenfeld, D., Weigel, R., Jurkat, T., Meinrat O. Andreae, M.O., Wendisch, M., Pöschl, U.,  
1474 Voigt, C., Mahnke, C., Borrmann, S., Albrecht, R.I., Molleker, S., Vila, D.A., Machado, L.A.T., and Grulich, L.:  
1475 Further evidence for CCN aerosol concentrations determining the height of warm rain and ice initiation in  
1476 convective clouds over the Amazon basin, *Atmos. Chem., Phys.*, 17, 14433–14456, [https://doi.org/10.5194/acp-](https://doi.org/10.5194/acp-17-14433-2017)  
1477 [17-14433-2017](https://doi.org/10.5194/acp-17-14433-2017), 2017.

1478 Cassiani, M., Stohl, A., and Eckhardt S.: The dispersion characteristics of air pollution from world's megacities,  
1479 *Atmospheric Chemistry and Physics*, 13, 9975–9996, 2013.

1480 Chan Miller, C., Jacob, D. J., Marais, E. A., Yu, K., Travis, K. R., Kim, P. S., Fisher, J. A., Zhu, L., Wolfe, G.  
1481 M., Hanisco, T. F., Keutsch, F. N., Kaiser, J., Min, K.-E., Brown, S. S., Washenfelder, R. A., González Abad,  
1482 G., and Chance, K.: Glyoxal yield from isoprene oxidation and relation to formaldehyde: chemical mechanism,  
1483 constraints from SENEX aircraft observations, and interpretation of OMI satellite data, *Atmos. Chem. Phys.*, 17,  
1484 8725–8738, <https://doi.org/10.5194/acp-17-8725-2017>, 2017.

1485 Chance, K., Palmer, P. I., Spurr, R. J. D., Martin, R. V., Kurosu, T. P., and Jacob, D.: Satellite observations of  
1486 formaldehyde over North America from GOME, *Geophys. Res. Lett.*, 27, 3461–3464, 2000.

1487 Chen H., Winderlich, J., Gerbig, C., Hofer, A., Rella, C. W., Crosson, E. R., Van Pelt, A. D., Steinbach, J.,  
1488 Kolle, O., Beck, V., Daube, B. C., Gottlieb, E. W., Chow, V. Y., Santoni, G. W., and S. C. Wofsy, High-  
1489 accuracy continuous airborne measurements of greenhouse gases (CO<sub>2</sub> and CH<sub>4</sub>) using the cavity ring-down  
1490 spectroscopy (CRDS) technique, *Atmos. Mes. Tech.*, 3, 375–386, 2010.

1491 Copernicus Climate Change Service (C3S): ERA5: Fifth generation of ECMWF atmospheric reanalyses of the  
1492 global climate. Copernicus Climate Change Service Climate Data Store (CDS), 2017.

1493 Crippa, M., DeCarlo, P. F., Slowik, J. G., Mohr, C., Heringa, M. F., Chirico, R., Poulain, L., Freutel, F., Sciare,  
1494 J., Cozic, J., Di Marco, C. F., Elsasser, M., Nicolas, J. B., Marchand, N., Abidi, E., Wiedensohler, A., Drewnick,  
1495 F., Schneider, J., Borrmann, S., Nemitz, E., Zimmermann, R., Jaffrezo, J.-L., Prévôt, A. S. H., and  
1496 Baltensperger, U.: Wintertime aerosol chemical composition and source apportionment of the organic fraction in  
1497 the metropolitan area of Paris, *Atmos. Chem. Phys.*, 13, 961–981, <https://doi.org/10.5194/acp-13-961-2013>,  
1498 2013.

1499 De Smedt, I., Stavrakou, T., Hendrick, F., Danckaert, T., Vlemmix, T., Pinardi, G., Theys, N., Lerot, C., Gielen,  
1500 C., Vigouroux, C., Hermans, C., Fayt, C., Veeffkind, P., Müller, J.-F., and Van Roozendaal, M.: Diurnal,  
1501 seasonal and long-term variations of global formaldehyde columns inferred from combined OMI and GOME-2  
1502 observations, *Atmos. Chem. Phys.*, 15, 12519–12545, <https://doi.org/10.5194/acp-15-12519-2015>, 2015.

1503 De Gouw, J. A., Warneke, C., Parrish, D. D., Holloway, J. S., Trainer, M., and Fehsenfeld, F. C.: Emission  
1504 sources and ocean uptake of acetonitrile (CH<sub>3</sub>CN) in the atmosphere, *J. Geophys. Res.*, D11, 108, 4329,  
1505 doi:10.1029/2002JD002897, 2003.

1506 De Sá, S. S., Palm, B. B., Campuzano-Jost, P., Day, D. A., Hu, W., Isaacman-VanWertz, G., Yee, L. D., Brito,  
1507 J., Carbone, S., Ribeiro, I. O., Cirino, G. G., Liu, Y., Thalman, R., Sedlacek, A., Funk, A., Schumacher, C.,  
1508 Shilling, J. E., Schneider, J., Artaxo, P., Goldstein, A. H., Souza, R. A. F., Wang, J., McKinney, K. A., Barbosa,  
1509 H., Alexander, M. L., Jimenez, J. L., and Martin, S. T.: Urban influence on the concentration and composition of  
1510 submicron particulate matter in central Amazonia, *Atmos. Chem. Phys.*, 18, 12185–12206, doi.org/10.5194/acp-  
1511 18-12185-2018, 2018.

1512 Diémoz, H., Barnaba, F., Magri, T., Pession, G., Dionisi, D., Pittavino, S., Tombolato, I., Campanelli, M., Della  
1513 Ceca, L. S., Hervo M., Di Liberto, L., Ferrero, L., Gobbi, G. P.: Transport of Po Valley aerosol pollution to the  
1514 northwestern Alps – Part 1: Phenomenology. *Atmospheric Chemistry and Physics*. 19. 3065–3095. 10.5194/acp-  
1515 19-3065-2019, 2019a.

1516 Diémoz, H., Gobbi, G.P., Magri, T., Pession, G., Pittavino, S., Tombolato, I.K.F., Campanelli, M., and Barnaba,  
1517 F.: Transport of Po Valley aerosol pollution to the northwestern Alps –Part 2: Long-term impact on air quality,  
1518 *Atmos. Chem. Phys.*, 19, 10129–10160, 2019b.

1519 Dodman, D.: Blaming cities for climate change? An analysis of urban greenhouse gas emissions inventories.  
1520 *Environ.Urban*. 21 (No. 1, April), 185–202, 2009.

1521 Dufour, G., Wittrock, F., Camredon, M., Beekmann, M., Richter, A., Aumont, B., and Burrows, J. P.:  
1522 SCIAMACHY formaldehyde observations: constraint for isoprene emission estimates over Europe?, *Atmos.*  
1523 *Chem. Phys.*, 9, 1647–1664, <https://doi.org/10.5194/acp-9-1647-2009>, 2009.

1524 European Environmental Agency: Air quality in Europe - 2019 report, No 10/2019; ISBN 978-92-9480-088-6,  
1525 doi:10.2800/822355, 2019.

1526 European Strategy and Policy Analysis System, ESPAS, Global Trends to 2030: The future of urbanization and  
1527 Megacities, ESPAS Ideas Paper series, 2018

1528 Finardi et al., Analysis of pollutants exchange between the Po Valley and the surrounding European region,  
1529 *Urban Climate* 2014

1530 Fischer, E. V., Jacob, D. J., Yantosca, R. M., Sulprizio, M. P., Millet, D. B., Mao, J., Paulot, F., Singh, H. B.,  
1531 Roiger, A., Ries, L., Talbot, R. W., Dzepina, K., and Pandey Deolal, S.: Atmospheric peroxyacetyl nitrate



1532 (PAN): a global budget and source attribution, *Atmos. Chem. Phys.*, 14, 2679–2698, [https://doi.org/10.5194/acp-](https://doi.org/10.5194/acp-14-2679-2014)  
1533 14-2679-2014, 2014.

1534 Fisher, R., Lowry, D., Wilkin, O., Sriskantharajah, S., and Nisbet, E.G.: High-precision, automated stable  
1535 isotope analysis of atmospheric methane and carbon dioxide using continuous-flow isotope-ratio mass  
1536 spectrometry, *Rapid communications in mass spectrometry: RCM*, 20 (2), 200–208. doi: 10.1002/rcm.2300,  
1537 2006.

1538 Flemming, J., Huijnen, V., Arteta, J., Bechtold, P., Beljaars, A., Blechschmidt, A.-M., Diamantakis, M.,  
1539 Engelen, R. J., Gaudel, A., Inness, A., Jones, L., Josse, B., Katragkou, E., Marecal, V., Peuch, V.-H., Richter, A.,  
1540 Schultz, M. G., Stein, O., and Tsikerdekis, A.: Tropospheric chemistry in the Integrated Forecasting System of  
1541 ECMWF, *Geosci. Model Dev.*, 8, 975–1003, doi: 10.5194/gmd-8-975-2015, 2015.

1542 Flemming, F., Jones, L., and Blechschmidt, A.-M.: CAMS supports scientific aircraft campaigns, ECMWF  
1543 Newsletter No. 160, Summer 2019, available online at <https://www.ecmwf.int/en/publications/newsletters>. 2019

1544 Förster, E., Bönisch, H., Neumaier, M., Obersteiner, F., Zahn, A., Hilboll, A., Kalisz Hedegaard, A. B.,  
1545 Daskalakis, N., Vrekoussis, M., Lichtenstern, M., and Braesicke P.: Chemical and dynamical identification of  
1546 emission outflows during the HALO campaign EMeRGe in Europe and Asia, in preparation, 2022, to be  
1547 submitted to ACP.

1548 Forzieri, G., Cescatti, A., Batista e Silva, F., Feyen, L.: Increasing risk over time of weather-related hazards to  
1549 the European population: a data-driven prognostic study, *The Lancet Planetary Health*, Vol 1, Issue 5, p e-200-  
1550 e208, 2017.

1551 Freney, E. J., Sellegri, K., Canonaco, F., Colomb, A., Borbon, A., Michoud, V., Doussin, J.-F., Crumeyrolle, S.,  
1552 Amarouche, N., Pichon, J.-M., Bourianne, T., Gomes, L., Prevot, A. S. H., Beekmann, M., and Schwarzenböck,  
1553 A.: Characterizing the impact of urban emissions on regional aerosol particles: airborne measurements during the  
1554 MEGAPOLI experiment, *Atmos. Chem. Phys.*, 14, 1397–1412, <https://doi.org/10.5194/acp-14-1397-2014>, 2014.

1555 Freutel, F., Schneider, J., Drewnick, F., von der Weiden-Reinmüller, S.-L., Crippa, M., Prévôt, A. S. H.,  
1556 Baltensperger, U., Poulain, L., Wiedensohler, A., Sciare, J., Sarda-Estève, R., Burkhardt, J. F., Eckhardt, S., Stohl,  
1557 A., Gros, V., Colomb, A., Michoud, V., Doussin, J. F., Borbon, A., Haeffelin, M., Morille, Y., Beekmann, M.,  
1558 and Borrmann, S.: Aerosol particle measurements at three stationary sites in the megacity of Paris during  
1559 summer 2009: meteorology and air mass origin dominate aerosol particle composition and size distribution,  
1560 *Atmos. Chem. Phys.*, 13, 933–959, <https://doi.org/10.5194/acp-13-933-2013>, 2013.

1561 Fu, T.-M., Jacob, D. J., Wittrock, F., Burrows, J. P., Vrekoussis, M., and Henze, D. K.: Global budgets of  
1562 atmospheric glyoxal and methylglyoxal, and implications for formation of secondary organic aerosols, *J.*  
1563 *Geophys. Res.-Atmos.*, 113, D15303, <https://doi.org/10.1029/2007JD009505>, 2008.

1564 Fu, Y., Tai, A. P. K. and Liao, H.: Impacts of historical climate and land cover  
1565 changes on fine particulate matter (PM<sub>2.5</sub>) air quality in East Asia between 1980 and 2010, *Atmospheric*  
1566 *Chemistry and Physics*, 16(16), pp. 10369–10383. doi: 10.5194/acp-16-10369-2016, 2016.

1567 Gardi, C.: *Urban Expansion, Land Cover and Soil Ecosystem Services*, Ed. Taylor & Francis, ISBN  
1568 1317504712, 9781317504719, 2017.

1569 Garzon, J.P., Huertas, J. I., Magana, M. Huertas, M.E., Cardenas, B., Watanabe, T., Maeda, T., Wakamatsu, S.,  
1570 Blanco, S.: Volatile organic compounds in the atmosphere of Mexico City, *Atmospheric Environment*, 119, 425-  
1571 429, 2015.

1572 Gelencsér, A; Siszler, K; and Hlavay, J: *Environmental Science & Technology* 31 (10), 2869-2872, doi:  
1573 10.1021/es970004c, 1997.

1574 General, S., Pöhler, D., Sihler, H., Bobrowski, N., Frieß, U., Zielcke, J., Horbanski, M., Shepson, P. B., Stirm, B.  
1575 H., Simpson, W. R., Weber, K., Fischer, C., and Platt, U.: The Heidelberg Airborne Imaging DOAS Instrument  
1576 (HAIDI) – a novel Imaging DOAS device for 2-D and 3-D imaging of trace gases and aerosols, *Atmos. Meas.*  
1577 *Tech.*, 7, 3459–3485, 2014, doi:10.5194/amt-7-3459-2014.

George, M., Andrés Hernández, M. D., Nenakhov, V., Liu, Y., and Burrows, J. P.: Airborne measurement of peroxy radicals using chemical amplification coupled with cavity ring-down spectroscopy: the PeRCEAS instrument, *Atmos. Meas. Tech.*, 13, 2577–2600, <https://amt.copernicus.org/articles/13/2577/2020/>, 2020.

George, M., Andrés Hernández, M. D., Nenakhov, V., Liu, Y., Burrows, J. P., Bohn, B., Förster, E., Obersteiner, F., Zahn, A., Harlaß, T., Ziereis, H., Schlager, H., Schreiner, B., Kluge, F., Bigge, K., and Pfeilsticker, K.: On the understanding of tropospheric fast photochemistry: airborne observations of peroxy radicals during the EMERG-Europe campaign, *Atmos. Chem. Phys. Discuss.* [preprint], <https://doi.org/10.5194/acp-2022-119>, in review, 2022.

Gerbig, C., Kley, D., Volz-Thomas, A., Kent, J., Dewey, K., and McKenna, D. S.: Fast response resonance fluorescence CO measurements aboard the C-130: Instrument characterization and measurements made during North Atlantic Regional Experiment 1993, *J. Geophys. Res.*, 101, 29229–29238, 1996.

Gioli, B., Miglietta, F., Vaccari, F. P., Zaldei, A. and De Martino, B.: The Sky Arrow ERA, an innovative airborne platform to monitor mass, momentum and energy exchange of ecosystems. *Annals of Geophysics*. 49. 10.4401/ag-3159, 2009.

Gioli, B., Carfora, M.F., Magliulo, V., Metallo, M.C., Poli, A.A., Toscano, P., and Miglietta, F.: Aircraft mass budgeting to measure CO<sub>2</sub> emissions of Rome, Italy, *Environmental monitoring and assessment*, 186 (4), 2053–2066. DOI: 10.1007/s10661-013-3517-4, 2014.

Gkikas, A; Hatzianastassiou, N., Mihalopoulos, N., Katsoulis, V., Kazadzis, S., Pey, J., Querol, X., and Torres, O.: The regime of intense desert dust episodes in the Mediterranean based on contemporary satellite observations and ground measurements, *Atmos. Chem. Phys.*, 13, 12135–12154, doi:10.5194/acp-13-12135-2013, 2013.

Giles, D.M., Sinyuk, A., Sorokin, M.G., Schafer, J.S., Smirnov, A., Slutsker, I., Eck, T.F., Holben, B.N., Lewis, J.R., Campbell, J.R., Welton, E., J., Korkin, S. V., and Lyapustin, A. I. : Advancements in the Aerosol Robotic Network (AERONET) Version 3 database – automated near-real-time quality control algorithm with improved cloud screening for Sun photometer aerosol optical depth (AOD) measurements, *Atmos. Meas. Tech.*, 12, 169–209, doi.org/10.5194/amt-12-169-2019, 2019.

Goldstein, A. and Shaw, S.: Isotopes of volatile organic compounds: an emerging approach for studying atmospheric budgets and chemistry, *Chem. Rev.*, 103, 5025–5048, doi:10.1021/cr0206566, 2003.

Grewe, V., Tsati, E., Mertens, M., Frömming, C., & Jöckel, P.: Contribution of emissions to concentrations: the TAGGING 1.0 submodel based on the Modular Earth Submodel System (MESSy 2.52), *Geoscientific Model Development*, 10, 2615–2633, doi: 10.5194/gmd-10-2615-2017, URL <https://www.geosci-model-dev.net/10/2615/2017/>, 2017.

Grimm, N.B., Faeth, S.H., Golubiewski, N.E., Redman, C.L., Wu, J., Bai, X., Briggs, J.M.: Global change and the ecology of cities. *Science* 319, 756–760. doi:10.1126/science.1150195, 2008.

Guerreiro, S. B., Dawson, R. J., Kilsby, C., Lewis, E., and Ford, A.: Future heat-waves, droughts and floods in 571 European cities, *Environ. Res. Lett.* 13 034009, doi.org/10.1088/1748-9326/aaaad3, 2018.

Haywood, J. and Boucher, O.: Estimates of the direct and indirect radiative forcing due to tropospheric aerosols: A review, *Reviews of Geophysics*, doi: 38.10.1029/1999RG000078, 2000.

Heckel A., Richter, A. Tarsu T., Wittrock, F., Hak C., Pundt I., Junkermann W. and Burrows J.P. :MAX-DOAS measurements of formaldehyde in Po-Valley, *Atmospheric Chemistry and Physics*, 5, 909-918, 2005.

Helfter, C., Tremper, A.H., Halios, C.H., Kotthaus, S., Björkegren, A., Grimmond, C.S.B., Barlow, J.F., and Nemitz, E.: Spatial and temporal variability of urban fluxes of methane, carbon monoxide and carbon dioxide above London, UK, *Atmos. Chem. Phys.*, 16 (16), 10543–10557. DOI: 10.5194/acp-16-10543-2016, 2016.

Hennigan, C. J., Sullivan, A. P., Collett, J. L., and Robinson, A. L.: Levoglucosan stability in biomass burning particles ex-posed to hydroxyl radicals, *Geophys. Res. Lett.*, 37, L09806, doi:10.1029/2010GL043088, 2010.

Hennigan, C. J., Miracolo, M. A., Engelhart, G. J., May, A. A., Presto, A. A., Lee, T., Sullivan, A. P., McMeeking, G. R., Coe, H., Wold, C. E., Hao, W.-M., Gilman, J. B., Kuster, W. C., de Gouw, J., Schichtel, B.

1624 A., Collett Jr., J. L., Kreidenweis, S. M., and Robinson, A. L.: Chemical and physical transformations of organic  
1625 aerosol from the photo-oxidation of open biomass burning emissions in an environmental chamber, *Atmos.*  
1626 *Chem. Phys.*, 11, 7669–7686, doi.org/10.5194/acp-11-7669-2011, 2011.

1627 Hilboll, A., Richter, A., and Burrows, J. P.: Long-term changes of tropospheric NO<sub>2</sub> over megacities derived  
1628 from multiple satellite instruments, *Atmos. Chem. Phys.*, 13, 4145–4169, doi:10.5194/acp-13-4145-2014, 2014

1629 Holanda, B.A., Pöhlker, M.L., Walter, D., Saturno, J., Sörgel, M., Ditas, J., Ditas, F. Schulz, C., et al.: Influx of  
1630 African biomass burning aerosol during the Amazonian dry season through layered transatlantic transport of  
1631 black carbon-rich smoke, *Atmos. Chem. Phys.*, 20, 4757–4785, doi.:org/10.5194/acp-20-4757-2020, 2020.

1632 ~~Holanda et al., in preparation 2021: Characteristic correlations between CCN and BC of most relevant aerosol~~  
1633 ~~species.~~

1634 Holben, B.N., Eck, T.F., Slutsker, I., Tanré, D., Buis, J.P., Setzer, A., Vermote, E., Reagan, J.A., Kaufman, Y.J.,  
1635 Nakajima, T., Lavenu, F., Jankowiak, I., and Smirnov, A.: Aeronet—A Federated Instrument Network and Data  
1636 Archive for Aerosol Characterization. Remote Sensing of Environment, 66, 1–16. doi.org/10.1016/S0034-  
1637 4257(98)00031-5, 1998.

1638 Hollingsworth, A. R., Engelen, R. J., Textor, C., Benedetti, A., Boucher, O., Chevallier, F., Dethof, A., Elbern,  
1639 H., Eskes, H., Flemming, Granier, C., Kaiser, J. W., Morcrette, J.-J., Rayner, P., Peuch, V.-H., Rouil, L., Schultz,  
1640 M. G., Simmons, A. J., and Consortium, T. G.: Toward a monitoring and forecasting system for atmospheric  
1641 composition: The GEMS project, *B. Am. Meteorol. Soc.*, 89, 1147–1164, 2008.

1642 Hoole, C., Hincks, S. and Rae, A.: The contours of a new urban world? Megacity population growth and density  
1643 since 1975. *Town Planning Review*, 90 (6). ISSN 0041-0020, <https://doi.org/10.3828/tpr.2019.41>, 2019.

1644 Hüneke, T., Aderhold, O.-A., Bounin, J., Dorf, M., Gentry, E., Grossmann, K., Grooß, J.-U., Hoor, P., Jöckel, P.,  
1645 Kenntner, M., Knapp, M., Knecht, M., Lörks, D., Ludmann, S., Matthes, S., Raecke, R., Reichert, M., Weimar,  
1646 J., Werner, B., Zahn, A., Ziereis, H., and Pfeilsticker, K.: The novel HALO mini-DOAS instrument: inferring  
1647 trace gas concentrations from airborne UV/visible limb spectroscopy under all skies using the scaling method,  
1648 *Atmos. Meas. Tech.*, 10, 4209–4234, <https://doi.org/10.5194/amt-10-4209-2017>, 2017.

1649 Huijnen, V., Williams, J., van Weele, M., van Noije, T., Krol, M., Dentener, F., Segers, A., Houweling, S.,  
1650 Peters, W., de Laat, J., Boersma, F., Bergamaschi, P., van Velthoven, P., Le Sager, P., Eskes, H., Alkemade, F.,  
1651 Scheele, R., Nédélec, P., and Pätz, H.-W.: The global chemistry transport model TM5: description and  
1652 evaluation of the tropospheric chemistry version 3.0, *Geosci. Model Dev.*, 3, 445–473,  
1653 <https://doi.org/10.5194/gmd-3-445-2010>, 2010.

1654 Huntrieser, H., and H. Schlager: Air Pollution Export from and Import to Europe: Experimental Evidence, In:  
1655 *The Handbook of Environmental Chemistry, Vol. 4 Air Pollution: Intercontinental Transport of Air Pollution*  
1656 (Ed. A. Stohl), Springer Verlag, pp. 69–98. 2004.

1657 Huntrieser, H., Heland, J., Schlager, H., Forster, C., Stohl, A., Aufmhoff, H., Arnold, F. Scheel, H.E., Campana,  
1658 M., Gilge, S., Eixmann, R., and Cooper O. : Intercontinental air pollution transport from North America to  
1659 Europe: Experimental evidence from airborne measurements and surface observations, *J. Geophys. Res.*, 110,  
1660 D01305, doi:10.1029/2004JD005045, 2005.

1661 Im, U., Markakis, K., Koçak, M., Gerasopoulos, E., Daskalakis, N., Mihalopoulos, N., Poupkou, A., Kindap, T.,  
1662 Unal, A., and Kanakidou, M.: Summertime aerosol chemical composition in the Eastern Mediterranean and its  
1663 sensitivity to temperature, *Atmos. Environ.*, 50, 164–173, <https://doi.org/10.1016/j.atmosenv.2011.12.044>, 2012.

1664 Inness, A., Blechschmidt, A.-M., Bouarar, I., Chabrillat, S., Crepulja, M., Engelen, R. J., Eskes, H., Flemming,  
1665 J., Gaudel, A., Hendrick, F., Huijnen, V., Jones, L., Kapsomenakis, J., Katragkou, E., Keppens, A., Langerock,  
1666 B., de Mazière, M., Melas, D., Parrington, M., Peuch, V. H., Razinger, M., Richter, A., Schultz, M. G., Suttie,  
1667 M., Thouret, V., Vrekoussis, M., Wagner, A., and Zerefos, C.: Data assimilation of satellite-retrieved ozone,  
1668 carbon monoxide and nitrogen dioxide with ECMWF's Composition-IFS, *Atmos. Chem. Phys.*, 15, 5275–5303,  
1669 doi:10.5194/acp-15-5275-2015, 2015.

1670 IPCC, 2014: Climate Change 2014: Synthesis Report. Contribution of Working Groups I, II and III to the Fifth  
 1671 Assessment Report of the Intergovernmental Panel on Climate Change (Core Writing Team, R.K. Pachauri and  
 1672 L.A. Meyer (eds.)). IPCC, Geneva, Switzerland, 151 pp. 2014.

1673 Jacob, D.J., and Winner, D.A.: Effect of climate change on air quality, *Atmospheric Environment*, 43, 51-63,  
 1674 doi:10.1016/j.atmosenv.2008.09.051, 2009.

1675 Jöckel, P., Kerkweg, A., Pozzer, A., Sander, R., Tost, H., Riede, H., Baumgaertner, A., Gromov, S., & Kern, B.:  
 1676 Development cycle 2 of the Modular Earth Submodel System (MESSy2), *Geoscientific Model Development*, 3,  
 1677 717–752, doi: 10.5194/gmd-3-717-2010, URL <http://www.geosci-model-dev.net/3/717/2010/>, 2010

1678 Jonson, J. E., Schulz, M., Emmons, L., Flemming, J., Henze, D., Sudo, K., Tronstad Lund, M., Lin, M.,  
 1679 Benedictow, A., Koffi, B., Dentener, F., Keating, T., Kivi, R., and Davila, Y., The effect of intercontinental  
 1680 emission sources on European air pollution levels. *Atmos. Chem. Phys.*, 18, 13655–13672,  
 1681 <https://doi.org/10.5194/acp-18-13655-2018>, 2018.

1682 Kaiser, J. W., Heil, A., Andreae, M. O., Benedetti, A., Chubarova, N., Jones, L., Morcrette, J.-J., Razinger, M.,  
 1683 Schultz, M. G., Suttie, M., and van der Werf, G. R.: Biomass burning emissions estimated with a global fire  
 1684 assimilation system based on observed fire radiative power, *Biogeosciences*, 9, 527–554,  
 1685 <https://doi.org/10.5194/bg-9-527-2012>, 2012.

1686 Kaiser, J., Wolfe, G. M., Min, K. E., Brown, S. S., Miller, C. C., Jacob, D. J., de Gouw, J. A., Graus, M.,  
 1687 Hanisco, T. F., Holloway, J., Peischl, J., Pollack, I. B., Ryerson, T. B., Warneke, C., Washenfelder, R. A., and  
 1688 Keutsch, F. N.: Reassessing the ratio of glyoxal to formaldehyde as an indicator of hydrocarbon precursor  
 1689 speciation, *Atmos. Chem. Phys.*, 15, 7571–7583, <https://doi.org/10.5194/acp-15-7571-2015>, 2015.

1690 Kalivitis, N., Gerasopoulos, E., Vrekoussis, M., Kouvarakis, G., Kubilay, N., Hatzianastassiou, N., Vardavas, I.  
 1691 and Mihalopoulos, N, Dust transport over the eastern Mediterranean derived from Total Ozone Mapping  
 1692 Spectrometer, Aerosol Robotic Network, and surface measurements, *Journal of Geophysical Research-*  
 1693 *Atmospheres* 112(D3), 2007.

1694 Kalnay, E., Kanamitsu, M., Kistler, R., Collins, W., Deaven, D., Gandin, L., Iredell, M., Saha, S., White, G.,  
 1695 Woollen, J., Zhu, Y., Leetmaa, A., Reynolds, B., Chelliah, M., Ebisuzaki, W., Higgins, W., Janowiak, J., Mo, K.  
 1696 C., Ropelewski, C., Wang, J., Jenne, R., and Joseph, D. : The NCEP/NCAR 40-year reanalysis project, *Bull.*  
 1697 *Amer. Meteor. Soc.*, 77, 437-470, 1996.

1698 Kanakidou, M., Mihalopoulos, N., Kindap, T., Im, U., Vrekoussis, M., Gerasopoulos, E., Dermizaki, E., Unal,  
 1699 A., Koçak, M., Markakis, K., Melas, D., Kouvarakis, G., Youssef, A.F., Richter, A., Hatzianastassiou, N.,  
 1700 Hilboll, A., Ebojie, F., Wittrock, F., von Savigny, C., Burrows, J.P., Ladstaetter-Weissenmayer, A., Moubasher,  
 1701 H.: Megacities as hot spots of air pollution in the East Mediterranean, *Atmospheric Environment*, 45, 1223-  
 1702 1235, 2011.

1703 Kerkweg, A. & Jöckel, P.: The 1-way on-line coupled atmospheric chemistry model system MECO(n) – Part 2:  
 1704 On-line coupling with the Multi-Model-Driver (MMD), *Geoscientific Model Development*, 5, 111–128, doi:  
 1705 10.5194/gmd-5-111-2012, URL <http://www.geosci-model-dev.net/5/111/2012/>, 2012

1706 Kluge, F., Hüneke, T., Knecht, M., Lichtenstern, M., Rotermund, M., Schlager, H., Schreiner, B., and  
 1707 Pfeilsticker, K.: Profiling of formaldehyde, glyoxal, methylglyoxal, and CO over the Amazon: normalized  
 1708 excess mixing ratios and related emission factors in biomass burning plumes, *Atmos. Chem. Phys.*, 20, 12363–  
 1709 12389, <https://doi.org/10.5194/acp-20-12363-2020>, 2020.

1710 Klausner, T. M., Aircraft-based in situ measurements of CH<sub>4</sub> and CO<sub>2</sub> downstream of European and Asian urban  
 1711 centres at local to synoptic scales. Dissertation, LMU München: Fakultät für Physik, doi: 10.5282/edoc.26983,  
 1712 2020.

1713 Klausner, T., Mertens, M., Huntrieser, H., Galkowski, M., Kuhlmann, G., Baumann, R., Fiehn, A., Jöckel P.,  
 1714 Pühl, M., and Roitger, A.: Urban greenhouse gas emissions from the Berlin area: A case study using airborne  
 1715 CO<sub>2</sub> and CH<sub>4</sub> in situ observations in summer 2018. *Elem Sci Anth*, 8: 15, [doi.org/10.1525/elementa.411](https://doi.org/10.1525/elementa.411), 2020.

1716 [Krüger, O. O., Holanda, B. A., Chowdhury, S., Pozzer, A., Walter, D., Pöhlker, C., Andrés Hernández, M. D.,](#)  
1717 [Burrows, J. P., Voigt, C., Lelieveld, J., Quaas, J., Pöschl, U., and Pöhlker, M. L.: Black carbon aerosol](#)  
1718 [reductions during COVID-19 confinement quantified by aircraft measurements over Europe, Atmos. Chem.](#)  
1719 [Phys. Discuss. \[preprint\], <https://doi.org/10.5194/acp-2021-1100>, in review, 2022.](#)

1720 Kuc, T., Rozanski, K., Zimnoch, M., Necki, J.M., and Korus, A.: Anthropogenic emissions of CO<sub>2</sub> and CH<sub>4</sub> in  
1721 an urban environment, *Applied Energy*, 75 (3-4), 193–203. DOI: 10.1016/S0306-2619(03)00032-1, 2003.

1722 Kunkel, D., M. G. Lawrence, H. Tost, A. Kerkweg, P. Jöckel, and Borrmann S.: Urban emission hot spots as  
1723 sources for remote aerosol deposition, *Geophys. Res. Lett.*, 39, L01808, doi: 10.1029/2011GL049634, 2012.

1724 Laborde, M., Crippa, M., Tritscher, T., Jurányi, Z., Decarlo, P. F., Temime-Roussel, B., Marchand, N., Eckhardt,  
1725 S., Stohl, A., Baltensperger, U., Prévôt, A. S. H., Weingartner, E., and Gysel, M.: Black carbon physical  
1726 properties and mixing state in the European megacity Paris, *Atmos. Chem. Phys.*, 13, 5831–5856,  
1727 <https://doi.org/10.5194/acp-13-5831-2013>, 2013.

1728 Lai, C., Liu, Y., Ma, J., Ma, Q., He, H.: Degradation kinetics of levoglucosan initiated by hydroxyl radical under  
1729 different environmental conditions, *Atmospheric Environment*, 91, 32–39,  
1730 [doi.org/10.1016/j.atmosenv.2014.03.054](https://doi.org/10.1016/j.atmosenv.2014.03.054), 2014.

1731 Lambe, A. T., Onasch, T. B., Massoli, P., Croasdale, D. R., Wright, J. P., Ahern, A. T., Williams, L. R.,  
1732 Worsnop, D. R., Brune, W. H., and Davidovits, P.: Laboratory studies of the chemical composition and cloud  
1733 condensation nuclei (CCN) activity of secondary organic aerosol (SOA) and oxidized primary organic aerosol  
1734 (OPOA), *Atmos. Chem. Phys.*, 11, 8913–8928, doi.org/10.5194/acp-11-8913-2011, 2011.

1735 Lawrence, M.G., Butler, T.M., Steinkamp, J., Gurjar, B.R., and J. Lelieveld: Regional pollution potentials of  
1736 megacities and other major population centers, *Atmos. Chem. Phys.*, 7, 3969–3987, doi:10.5194/acp-7-3969-  
1737 2007, 2007.

1738 Lawrence, M.G., and Lelieveld, J.: Atmospheric pollutant outflow from southern Asia:  
1739 a review, *Atmos. Chem. Phys.*, 10, 11017–11096, doi:10.5194/acp-10-11017-2010, 2010.

1740 Lelieveld, J., Berresheim, H., Borrmann, S., Crutzen, P.J., Dentener, F.J., Fischer,  
1741 H., et al.: Global air pollution crossroads over the Mediterranean. *Science* 298, 794,  
1742 doi: 10.1126/science.1075457, 2002.

1743 Lelieveld, J., Evans, J., Fnais, M., Giannadaki, D., and Pozzer, A.: The Contribution of Outdoor Air Pollution  
1744 Sources to Premature Mortality on a Global Scale, *Nature*, vol. 525, pp. 367–371, 2015.

1745 Lelieveld, J., Klingmüller, K., Pozzer, A., Burnett, R. T., Haines, A., and Ramanathan, V.: Effects of fossil fuel  
1746 and total anthropogenic emission removal on public health and climate, *P. Natl. Acad. Sci. USA*, 116, 7192–  
1747 7197, <https://doi.org/10.1073/pnas.1819989116>, 2019.

1748 Lelieveld, J., Pozzer, A., Pöschl, U., Fnais, M., Haines, A., and Münzel, T.: Loss of life expectancy from air  
1749 pollution compared to other risk factors: a worldwide perspective, *Cardiovascular Research*, 116, 1910–1917,  
1750 doi: 10.1093/cvr/cvaa025, 2020.

1751 Leung, D. M., Tai, A. P. K., Mickley, L. J., Moch, J. M., Van Donkelaar, A., Shen, L. and Martin, R. V.,  
1752 Synoptic meteorological modes of variability for fine particulate matter (PM<sub>2.5</sub>) air quality in major  
1753 metropolitan regions of China, *Atmospheric Chemistry and Physics*, 18(9), pp. 6733–6748. doi: 10.5194/acp-18-  
1754 6733-2018, 2018.

1755 Lian, J., Bréon, F.-M., Broquet, G., Zaccheo, T.S., Dobler, J., Ramonet, M., Staufer, J., Santaren, D., Xueref-  
1756 Remy, I., and Ciais, P.: Analysis of temporal and spatial variability of atmospheric CO<sub>2</sub> concentration within  
1757 Paris from the GreenLITE TM laser imaging experiment, *Atmos. Chem. Phys. Discuss.*  
1758 <https://doi.org/10.5194/acp-2019-547>, 2019.

1759 Liu, D., Allan, J. D., Young, D. E., Coe, H., Beddows, D., Fleming, Z. L., Flynn, M. J., Gallagher, M. W.,  
1760 Harrison, R. M., Lee, J., Prevot, A. S. H., Taylor, J. W., Yin, J., Williams, P. I., and Zotter, P.: Size distribution,  
1761 mixing state and source apportionment of black carbon aerosol in London during wintertime, *Atmos. Chem.*  
1762 *Phys.*, 14, 10061–10084, <https://doi.org/10.5194/acp-14-10061-2014>, 2014.

1763 Mallaun, C., Giez, A. and Baumann, R.: Calibration of 3-D wind measurements on a single engine research  
1764 aircraft *Atmos. Meas. Tech.*, 8, 3177-3196, doi: 10.5194/amt-8-3177-2015, 2015.

1765 Mar, K.A., Putting the brakes on climate change – it's about more than just CO<sub>2</sub>., *Climanosco Research Articles*  
1766 3, <https://doi.org/10.37207/CRA.3.1>, 2021.

1767 Mayer, M., Wang, C., Webster, M., and Prinn, R. G.: Linking local air pollution to global chemistry and climate,  
1768 *J. Geophys. Res.*, 105, 22869–22896, 2000.

1769 Mei, L. L., Rozanov, V., Vountas, M., Burrows, J., Levy, R., Lotz, W., Retrieval of aerosol optical properties  
1770 using MERIS observations: algorithm and some first results, *Remote Sensing of Environment*, doi:10.1016/  
1771 j.rse.2016.11.015, 197, 125-140, 2017a

1772 Mei, L. L., Rozanov, V., Vountas, M., Burrows, J., Levy, R., Lotz, W., A Cloud masking algorithm for the  
1773 XBAER aerosol retrieval using MERIS data, *Remote Sensing of Environment* doi.:  
1774 10.1016/j.rse.2016.11.016,197, 141-160, 2017b

1775 Melchiorri, M.; Florczyk, A.J.; Freire, S.; Ehrlich, D.; Schiavina, M.; Pesaresi, M.; Kemper, T. Megacities  
1776 Spatiotemporal Dynamics Monitored with the Global Human Settlement Layer. In *Proceedings of the REAL*  
1777 *CORP 2018 Expanding Cities—Diminishing Space*, Wien, Austria, 4–6 April 2018; Schrenk, M., Popovisch,  
1778 V.V., Zeile, P., Elisei, P., Beyer, C., Navratil, G., Eds.; CORP: Wien, Austria, 2018; pp. 285–294, 2018.

1779 Mertens, M., Kerkweg, A., Jöckel, P., Tost, H., & Hofmann, C.: The 1-way on-line coupled model system  
1780 MECO(n) – Part 4: Chemical evaluation (based on MESSy v2.52), *Geoscientific Model Development*, 9, 3545–  
1781 3567, doi: 10.5194/gmd-9-3545-2016, URL <http://www.geosci-model-dev.net/9/3545/2016/>, 2016.

1782 Mertens, M., Kerkweg, A., Grewe, V., Jöckel, P., & Sausen, R.: Attributing ozone and its precursors to land  
1783 transport emissions in Europe and Germany, *Atmospheric Chemistry and Physics*, 20, 7843–7873, doi:  
1784 10.5194/acp-20-7843-2020, URL <https://www.atmos-chem-phys.net/20/7843/2020/>, 2020.

1785 Mertens, M., Kerkweg, A., Grewe, V., Jöckel, P., & Sausen, R.: Are contributions of emissions to ozone a matter  
1786 of scale? – a study using MECO(n) (MESSy v2.50), *Geoscientific Model Development*, 13, 363–383, doi:  
1787 10.5194/gmd-13-363-2020, URL <https://www.geosci-model-dev.net/13/363/2020/>, 2020.

1788 Millán, M.M., Salvador, R., Mantilla, E., Kallos, G.: Photooxidant dynamics in the Mediterranean basin in  
1789 summer: Results from European research projects, *Journal of Geophysical Research*, 102, N0. D7, 8811-8823,  
1790 1997.

1791 Millán, M. M., Mantilla, E., Salvador, R., Carratalá, A., Sanz, M. J., Alonso, L., Gangoiti, G., and Navazo, M.:  
1792 Ozone Cycles in the Western Mediterranean Basin: Interpretation of Monitoring Data in Complex Coastal  
1793 Terrain. *Journal of Applied Meteorology*, 39: 487-508. 2000.

1794 Monks, P. S., Granier, C., Fuzzi, S., Stohl, A., Williams, M. L., Akimoto, H., Amann, M., Baklanov, A.,  
1795 Baltensperger, U., Bey, I., Blake, N., Blake, R. S., Carslaw, K., Cooper, O. R., Dentener, F., Fowler, D.,  
1796 Fragkou, E., Frost, G. J., Generoso, S., Ginoux, P., Grewe, V., Guenther, A., Hansson, H. C., Henne, S., Hjorth,  
1797 J., Hofzumahaus, A., Huntrieser, H., Isaksen, I. S. A., Jenkin, M. E., Kaiser, J., Kanakidou, M., Klimont, Z.,  
1798 Kulmala, M., Laj, P., Lawrence, M. G., Lee, J. D., Liousse, C., Maione, M., McFiggans, G., Metzger, A.,  
1799 Mieville, A., Moussiopoulos, N., Orlando, J. J., O'Dowd, C. D., Palmer, P. I., Parrish, D. D., Petzold, A., Platt,  
1800 U., Pöschl, U., Prévôt, A. S. H., Reeves, C. E., Reimann, S., Rudich, Y., Sellegri, K., Steinbrecher, R., Simpson,  
1801 D., ten Brink, H., Theloke, J., van der Werf, G. R., Vautard, R., Vestreng, V., Vlachokostas, Ch., von Glasow, R.:  
1802 Atmospheric composition change-global and regional air quality, *Atmospheric Environment*, 43, 5268–5350,  
1803 doi:10.1016/j.atmosenv.2009.08.021, 2009.

1804 Myriokefalitakis, S., Vrekoussis, M., Tsigaridis, K., Wittrock, F., Richter, A., Brühl, C., Volkamer, R., Burrows,  
1805 J.P., and Kanakidou, M: Influence of natural and anthropogenic secondary sources on the glyoxal global  
1806 distribution, *Atmos. Chem. Phys.*, 8, 4965-4981, 2008.

1807 Ng, N. L., Canagaratna, M. R., Zhang, Q., Jimenez, J. L., Tian, J., Ulbrich, I. M., Kroll, J. H., Docherty, K. S.,  
1808 Chhabra, P. S., Bahreini, R., Murphy, S. M., Seinfeld, J. H., Hildebrandt, L., Donahue, N. M., DeCarlo, P. F.,  
1809 Lanz, V. A., Prévôt, A. S. H., Dinar, E., Rudich, Y., and Worsnop, D. R.: Organic aerosol components observed



1810 in Northern Hemispheric datasets from Aerosol Mass Spectrometry, *Atmos. Chem. Phys.*, 10, 4625–4641,  
1811 doi.org/10.5194/acp-10-4625-2010, 2010.

1812 Ng, N. L., Canagaratna, M. R., Jimenez, J. L., Chhabra, P. S., Seinfeld, J. H., and Worsnop, D. R.: Changes in  
1813 organic aerosol composition with aging inferred from aerosol mass spectra, *Atmos. Chem. Phys.*, 11, 6465–  
1814 6474, doi.org/10.5194/acp-11-6465-2011, 2011.

1815 Odendahl, C., Springford, J., Johnson, S. and J. Murray: The big European sort? The diverging fortunes of  
1816 Europe's regions, Centre for European Reform, [www.cer.eu](http://www.cer.eu); 2019.

1817 O'Shea, S.J., Allen, G., Fleming, Z.L., Bauguutte, S.J.-B., Percival, C.J., Gallagher, M.W., Lee, J., Helfter, C.,  
1818 and Nemitz, E.: Area fluxes of carbon dioxide, methane, and carbon monoxide derived from airborne  
1819 measurements around Greater London: A case study during summer 2012, *J. Geophys. Res.* 119 (8), 4940–4952.  
1820 doi: 10.1002/2013JD021269, 2014.

1821 Paulot, F., Wunch, D., Crounse, J. D., Toon, G. C., Millet, D. B., DeCarlo, P. F., Vigouroux, C., Deutscher, N.  
1822 M., González Abad, G., Notholt, J., Warneke, T., Hannigan, J. W., Warneke, C., de Gouw, J. A., Dunlea, E. J.,  
1823 De Mazière, M., Griffith, D. W. T., Bernath, P., Jimenez, J. L., and Wennberg, P. O.: Importance of secondary  
1824 sources in the atmospheric budgets of formic and acetic acids, *Atmos. Chem. Phys.*, 11, 1989–2013,  
1825 <https://doi.org/10.5194/acp-11-1989-2011>, 2011.

1826 Pappalardo et al., EARLINET: towards an advanced sustainable European aerosol lidar network, *Atmos. Meas.*  
1827 *Tech.*, 7, 2389–2409, doi:10.5194/amt-7-2389-2014, 2014.

1828 Paz, S., Goldstein, P., Kordova-Biezuner, L. et al. Differences in Benzene Patterns Among Traffic and Industrial  
1829 Areas and a Prediction Model for Benzene Rates Based on NO<sub>x</sub> Values. *Water Air Soil Pollut* 226, 161,  
1830 doi.org/10.1007/s11270-015-2406-6, 2015.

1831 Pey, J., Querol, X., Alastuey, A., Forastiere, F., and Stafoggia, M.: African dust outbreaks over the  
1832 Mediterranean Basin during 2001–2011: PM<sub>10</sub> concentrations, phenomenology and trends, and its relation with  
1833 synoptic and mesoscale meteorology, *Atmos. Chem. Phys.*, 13, 1395–1410, doi:10.5194/acp-13-1395-2013,  
1834 2013.

1835 Pikridas, M., Vrekoussis, M., Sciare, J., Mihalopoulos, N., Kleanthous, S., and Savvidis, C, Spatial and temporal  
1836 (short and long-term) variability of submicron, fine and sub-10 µm particulate matter (PM<sub>1</sub>, PM<sub>2.5</sub>, PM<sub>10</sub>) in  
1837 Cyprus, *Atmos. Environ.*, 191:79–93, 2018. doi:10.1016/j.atmosenv.2018.07.048, 2018.

1838 Pitt, J.R., Allen, G., Bauguutte, S.J.-B., Gallagher, M.W., Lee, J.D., Drysdale, W., Nelson, B., Manning, A.J., and  
1839 Palmer, P.I.: Assessing London CO<sub>2</sub>, CH<sub>4</sub> and CO emissions using aircraft measurements and dispersion  
1840 modelling, *Atmos. Chem. Phys.* 2019, 19 (13), 8931–8945. DOI: 10.5194/acp-19-8931-2019.

1841 Pöhlker, M. L., Pöhlker, C., Ditas, F., Klimach, T., Hrabě de Angelis, I., Araújo, A., Brito, J., Carbone, S.,  
1842 Cheng, Y., Chi, X., Ditz, R., Gunthe, S. S., Kesselmeier, J., Könemann, T., Lavrič, J. V., Martin, S. T.,  
1843 Mikhailov, E., Moran-Zuloaga, D., Rose, D., Saturno, J., Su, H., Thalman, R., Walter, D., Wang, J., Wolff, S.,  
1844 Barbosa, H. M. J., Artaxo, P., Andreae, M. O., and Pöschl, U.: Long-term observations of cloud condensation  
1845 nuclei in the Amazon rain forest – Part 1: Aerosol size distribution, hygroscopicity, and new model  
1846 parametrizations for CCN prediction, *Atmos. Chem. Phys.*, 2016.

1847 Pöhlker, M. L., Ditas, F., Saturno, J., Klimach, T., Hrabě de Angelis, I., Araújo, A. C., Brito, J., Carbone, S.,  
1848 Cheng, Y., Chi, X., Ditz, R., Gunthe, S. S., Holanda, B. A., Kandler, K., Kesselmeier, J., Könemann, T., Krüger,  
1849 O. O., Lavrič, J. V., Martin, S. T., Mikhailov, E., Moran-Zuloaga, D., Rizzo, L. V., Rose, D., Su, H., Thalman,  
1850 R., Walter, D., Wang, J., Wolff, S., Barbosa, H. M. J., Artaxo, P., Andreae, M. O., Pöschl, U., and Pöhlker, C.:  
1851 Long-term observations of cloud condensation nuclei over the Amazon rain forest – Part 2: Variability and  
1852 characteristics of biomass burning, long-range transport, and pristine rain forest aerosols, *Atmos. Chem. Phys.*,  
1853 2018.

1854 Pöhlker, C., Walter, D., Paulsen, H., Könemann, T., Rodríguez-Caballero, E., Moran-Zuloaga, D., Brito, J.,  
1855 Carbone, S., Degrendele, C., Després, V. R., Ditas, F., Holanda, B. A., Kaiser, J. W., Lammel, G., Lavrič, J. V.,  
1856 Ming, J., Pickersgill, D., Pöhlker, M. L., Praß, M., Löbs, N., Saturno, J., Sörgel, M., Wang, Q., Weber, B.,  
1857 Wolff, S., Artaxo, P., Pöschl, U., and Andreae, M. O.: Land cover and its transformation in the backward

1858 trajectory footprint region of the Amazon Tall Tower Observatory, *Atmos. Chem. Phys.*, 19, 8425–8470,  
1859 <https://doi.org/10.5194/acp-19-8425-2019>, 2019.

1860 Pöschl, U.: Atmospheric aerosols: Composition, transformation, climate and health effects, *Angew. Chem. Int.*  
1861 *Ed.*, 44(46), 7520–7540, doi:10.1002/anie.200501122, doi: 10.1002/anie.200501122, 2005.

1862 Ramanathan V., Crutzen P. J., Kiehl J. T., Rosenfeld D.: Aerosols, climate, and the hydrological cycle. *Science*  
1863 294:2119–2124, DOI: 10.1126/science.1064034, 2001.

1864 Reddington, C.L., McMeeking G., Mann, G.W. Coe, H., Frontoso M. G, Liu, D., Flynn,  
1865 M., Spracklen, D.V., and Carslaw, K.S.: The mass and number size distributions of  
1866 black carbon aerosol over Europe, *Atmos. Chem. Phys.*, 13, 4917–4939, 2013.

1867 Rautenhaus, M., G. Bauer, and A. Dörnbrack,: A web service based tool to plan atmospheric research flights.  
1868 *Geosci. Model Dev.*, 5, 55–71, doi.org/10.5194/gmd-5-55-2012. 2012.

1869 Ren, Yu, Schlager, H., Martin D.: The Application of TD/GC/NICI–MS with an Al<sub>2</sub>O<sub>3</sub>-PLOT-S Column for the  
1870 Determination of Perfluoroalkylcycloalkanes in the Atmosphere. *Chromatographia*, 77, pp 309–316. doi:  
1871 10.1007/s10337-013-2584-6., 2013.

1872 Ren, Y., Baumann, R., Schlager, H.: An airborne perfluorocarbon tracer system and its first application for a  
1873 Lagrangian experiment. *Atmos. Meas. Tech.*, 8, 69–80. doi: 10.5194/amt-8-69-2015, 2015.

1874 Richter, A., Burrows, J. P., Nüß, H., Granier, C, Niemeier, U., Increase in tropospheric nitrogen dioxide over  
1875 China observed from space, *Nature*, 437, 129–132, doi: 10.1038/nature04092, 2005.

1876 Richter, A., Begoin, M., Hilboll, A., and Burrows, J. P.: An improved NO<sub>2</sub> retrieval for the GOME-2 satellite  
1877 instrument, *Atmos. Meas. Tech.*, 4, 1147–1159, doi:10.5194/amt-4-1147-2011, 2011.

1878 Roiger, A., Aufmhoff, H., Stock, P., Arnold, F., Schlager, H.: An aircraft-borne chemical ionization – ion trap  
1879 mass spectrometer (CI-ITMS) for fast PAN and PPN measurements. *Atmos. Meas. Tech.*, 4, 173–188. DOI:  
1880 10.5194/amt-4-173-2011, 2011.

1881 Rolph, G., Stein, A., and Stunder, B.: Real-time Environmental Applications and Display sYstem: READY.  
1882 *Environmental Modelling & Software*, 95, 210–228, <https://doi.org/10.1016/j.envsoft.2017.06>, 2017.

1883 Rosenfeld, D., Lohmann, U., Raga, G. B., O'Dowd, C. D., Kulmala, M., Fuzzi, S., Reissell, A., and Andreae, M.  
1884 O.: Flood or drought: How do aerosols affect precipitation?, *Science*, 321, 1309–1313, 10.1126/science.1160606,  
1885 2008.

1886 Rudolph, J., Czuba, E., and Huang, L.: The stable carbon isotope fractionation for reactions of selected  
1887 hydrocarbons with OH-radicals and its relevance for atmospheric chemistry, *J. Geophys. Res.*, 105, 29329–  
1888 29346, doi:10.1029/2000JD900447, 2000.

1889 Schneider, J., Weimer, S., Drewnick, F., Borrmann, S., Helas, G., Gwaze, P., Schmid, O., Andreae, M. O. and  
1890 Kirchner, U.: Massspectrometric analysis and aerodynamic properties of various types of combustion-related  
1891 aerosol particles, *Int. J. Mass. Spec.*, 258, 37–49, doi.org/10.1016/j.ijms.2006.07.008, 2006.

1892 Schroder, J. C., Campuzano-Jost, P., Day, D. A., Shah, V., Larson, K., Sommers, J. M., et al: Sources and  
1893 secondary production of organic aerosols in the northeastern United States during WINTER. *Journal of*  
1894 *Geophysical Research: Atmospheres*, 123, 7771– 7796. doi.org/10.1029/2018JD028475, 2018.

1895 Schulz, C., Schneider, J., Holanda, B. A., Appel, O., Costa, A., de Sá, S.S., Dreiling, V. Fütterer, D., Jurkat-  
1896 Witschas, T., Klimach, T., Knote, C., Krämer, M., Martin, S.T., Mertes, S., Pöhlker, M.L., Sauer, D., Voigt, C.,  
1897 Walser, A., Weinzierl, A.B., Ziereis, H., Zöger, M., Andreae, M.O., Artaxo, P., Machado, L-A.T., Pöschl, U.,  
1898 Wendisch, M., and S. Borrmann, Aircraft-based observations of isoprene-epoxydiol-derived secondary organic  
1899 aerosol (IEPOX-SOA) in the tropical upper troposphere over the Amazon region. *Atmos. Chem. Phys.*, 18,  
1900 14979–15001, [doi.org/10.5194/acp-18-14979-2018](https://doi.org/10.5194/acp-18-14979-2018), 2018.

1901 Schumann, U.: Measurement and model data comparisons for the HALO-FAAM formation flight during  
1902 EMERG on 17 July 2017, DLR FB 2020-48, doi.:10.5281/zenodo.4427965, 2020.

1903 Schwarz, J. P., Gao, R.S., Spackman, J.R., Watts, L.A., Thomson, D.S., Fahey, D.W., Ryerson, T.B., Peischl, J.,  
 1904 Holloway, J.S., Trainer, M., Frost, G.J., Baynard, T., Lack, D.A., de Gouw, J.A., Warneke, C., and Del Negro,  
 1905 L.A.: Measurement of the mixing state, mass, and optical size of individual black carbon particles in urban and  
 1906 biomass burning emissions, *Geophys. Res. Lett.*, 35, L13810, doi:10.1029/2008GL033968, 2008.

1907 Shaw, M. D., Lee, J. D., Davison, B., Vaughan, A., Purvis, R. M., Harvey, A., Lewis, A. C., and Hewitt, C. N.:  
 1908 Airborne determination of the tempo-spatial distribution of benzene, toluene, nitrogen oxides and ozone in the  
 1909 boundary layer across Greater London, UK, *Atmos. Chem. Phys.*, 15, 5083–5097, doi.org/10.5194/acp-15-5083-  
 1910 2015, 2015.

1911 Silver, B., Reddington, C.L., Arnold, S.R., and Spracklen: Substantial changes in air pollution across China  
 1912 during 2015–2017, *Environ. Res. Lett.* 13, 114012, 2018.

1913 Simpson, I. J., Akagi, S. K., Barletta, B., Blake, N. J., Choi, Y., Diskin, G. S., Fried, A., Fuelberg, H. E.,  
 1914 Meinardi, S., Rowland, F. S., Vay, S. A., Weinheimer, A. J., Wennberg, P. O., Wiebring, P., Wisthaler, A.,  
 1915 Yang, M., Yokelson, R. J., and Blake, D. R.: Boreal forest fire emissions in fresh Canadian smoke plumes: C1-  
 1916 C10 volatile organic compounds (VOCs), CO<sub>2</sub>, CO, NO<sub>2</sub>, NO, HCN and CH<sub>3</sub>CN, *Atmos. Chem. Phys.*, 11,  
 1917 6445–6463, <https://doi.org/10.5194/acp-11-6445-2011>, 2011.

1918 Speidel, M., Nau, R., Arnold, F., Schlager, H., A. Stohl, Sulfur dioxide measurements in the lower, middle and  
 1919 upper troposphere: Deployment of an aircraft-based chemical ionization mass spectrometer with permanent in-  
 1920 flight calibration, *Atmospheric Environment*, 41, 2427–2437, doi:10.1016/j.atmosenv.2006.07.047. 2007.

1921 Stein, A.F., Draxler, R.R., Rolph, G.D., Stunder, B.J.B., Cohen, M.D., and Ngan, F.: NOAA's HYSPLIT  
 1922 atmospheric transport and dispersion modeling system, *Bull. Amer. Meteor. Soc.*, 96, 2059–2077,  
 1923 doi.org/10.1175/BAMS-D-14-00110.1, 2015.

1924 Stohl, A., Wotawa, G. Seibert, P. and Kromp-Kolb H.: Interpolation errors in wind fields as a function of spatial  
 1925 and temporal resolution and their impact on different types of kinematic trajectories. *J. Appl. Meteor.* 34, p.  
 1926 2149–2165, 1995.

1927 Stohl, A., Haimberger, L., Scheele, M.P. and Wernli, H.: An intercomparison of results from three trajectory  
 1928 models. *Meteorol. Applications* 8, 127–135, 1999.

1929 Stohl, A., Eckhardt, S., Forster, C., James, P., and Spichtinger, N.: On the pathways and timescales of  
 1930 intercontinental air pollution transport. *J. Geophys. Res.*, 107(D23), 4684, doi:10.1029/2001JD001396, 2002.

1931 Stohl, A., Forster, C., Eckhardt, S., Spichtinger, N., Huntrieser, H., Heland, J., Schlager, H., Wilhelm, S.,  
 1932 Arnold, F., and Cooper, O.: A backward modeling study of intercontinental pollution transport using aircraft  
 1933 measurements. *J. Geophys. Res.*, 108(D12), 4370, doi:10.1029/2002JD002862, 2003.

1934 Tan, Z., Fuchs, H., Lu, K., Hofzumahaus, A., Bohn, B., Broch, S., Dong, H., Gomm, S., Häseler, R., He, L.,  
 1935 Holland, F., Li, X., Liu, Y., Lu, S., Rohrer, F., Shao, M., Wang, B., Wang, M., Wu, Y., Zeng, L., Zhang, Y.,  
 1936 Wahner, A., and Zhang, Y.: Radical chemistry at a rural site (Wangdu) in the North China Plain: observation and  
 1937 model calculations of OH, HO<sub>2</sub> and RO<sub>2</sub> radicals, *Atmos. Chem. Phys.*, 17, 663–690,  
 1938 <https://doi.org/10.5194/acp-17-663-2017>, 2017.

1939 Taraborrelli, D., Cabrera-Perez, D., Bacer, S., Gromov, S., Lelieveld, J., Sander, R., and Pozzer, A.: Influence of  
 1940 aromatics on tropospheric gas-phase composition, *Atmos. Chem. Phys. Discuss.*, [https://doi.org/10.5194/acp-](https://doi.org/10.5194/acp-2020-461)  
 1941 2020-461, 2020.

1942 Thieuleux, F., Moulin, C., Bréon, F. M., Maignan, F., Poitou, J., and Tanré, D.: Remote Sensing of Aerosols  
 1943 over the oceans using MSG/SEVIRI Imagery, *Ann. Geophys.*, 23, 3561–3568, doi:10.5194/angeo-23-3561-2005,  
 1944 2005.

1945 Titos, G., Ealo, M., Román, R., Cazorla, A., Sola, Y., Dubovik, O., Alastuey, A., Pandolfi, M.: Retrieval of  
 1946 aerosol properties from ceilometer and photometer measurements: long-term evaluation with in situ data and  
 1947 statistical analysis at Montsec (southern Pyrenees), *Atmos. Meas. Tech.*, [https://doi.org/10.5194/amt-12-3255-](https://doi.org/10.5194/amt-12-3255-2019)  
 1948 2019.

1949 Turco, M. et al., : Exacerbated Fires in Mediterranean Europe Due to Anthropogenic Warming Projected with  
1950 Non-Stationary Climate-Fire Models, *Nature Communications* 9, no. 1, 3821, [https://doi.org/10.1038/s41467-](https://doi.org/10.1038/s41467-018-06358-z)  
1951 018-06358-z, 2018.

1952 United Nations, Department of Economic and Social Affairs, Population Division World Urbanization  
1953 Prospects: The 2018 Revision (ST/ESA/SER.A/420). New York: United Nations, 2019.

1954 United Nations Environment Programme (UNEP), World Meteorological Organization (WMO), Integrated  
1955 Assessment of Black Carbon and Tropospheric Ozone, ISBN:92-807-3141-6, 2011.

1956 Viidanoja, J., Reiner, T. and Arnold, F: Laboratory investigations of negative ion molecule reactions of formic  
1957 and acetic acids: Implications for atmospheric measurements by Ion Molecule Reaction Mass Spectrometry, *Int.*  
1958 *J. Mass Spectrom.*, 181, 31-41, 1998.

1959 Volz-Thomas, A., Xueref, I., and Schmitt, R.: Automatic gas chromatograph and calibration system for ambient  
1960 measurements of PAN and PPN, *Environ. Sci. Poll. Res.*, 9, 72-76, 2001.

1961 von der Weiden-Reinmüller, S.-L., Drewnick, F., Zhang, Q. J., Freutel, F., Beekmann, M., and Borrmann, S.:  
1962 Megacity emission plume characteristics in summer and winter investigated by mobile aerosol and trace gas  
1963 measurements: the Paris metropolitan area, *Atmos. Chem. Phys.*, 14, 12931–12950, [https://doi.org/10.5194/acp-](https://doi.org/10.5194/acp-14-12931-2014)  
1964 14-12931-2014, 2014.

1965 Vrekoussis, M., Wittrock, F., Richter, A., Burrows, J.P: Temporal and spatial variability of glyoxal as observed  
1966 from space” *Atmos. Chem. Phys.*, 9, 4485-4504, 2009.

1967 Vrekoussis, M., Richter, A., Hilboll, A., Burrows, J. P., Gerasopoulos, E., Lelieveld, J., Barrie, L., Zerefos, C.,  
1968 and Mihalopoulos, N. Economic crisis detected from space: Air quality observations over Athens/Greece,  
1969 *Geophys. Res. Lett.*, 40, 458– 463, doi:10.1002/grl.50118. 2013.

1970 Whalley, L. K., Stone, D., Dunmore, R., Hamilton, J., Hopkins, J. R., Lee, J. D., Lewis, A. C., Williams, P.,  
1971 Kleffmann, J., Laufs, S., Woodward-Massey, R., and Heard, D. E.: Understanding in situ ozone production in  
1972 the summertime through radical observations and modelling studies during the Clean air for London project  
1973 (ClearfLo), *Atmos. Chem. Phys.*, 18, 2547–2571, <https://doi.org/10.5194/acp-18-2547-2018>, 2018.

1974 Whalley, L. K., Slater, E. J., Woodward-Massey, R., Ye, C., Lee, J. D., Squires, F., Hopkins, J. R., Dunmore, R.  
1975 E., Shaw, M., Hamilton, J. F., Lewis, A. C., Mehra, A., Worrall, S. D., Bacak, A., Bannan, T. J., Coe, H.,  
1976 Percival, C. J., Ouyang, B., Jones, R. L., Crilley, L. R., Kramer, L. J., Bloss, W. J., Vu, T., Kotthaus, S.,  
1977 Grimmond, S., Sun, Y., Xu, W., Yue, S., Ren, L., Acton, W. J. F., Hewitt, C. N., Wang, X., Fu, P., and Heard,  
1978 D. E.: Evaluating the sensitivity of radical chemistry and ozone formation to ambient VOCs and NO<sub>x</sub> in Beijing,  
1979 *Atmos. Chem. Phys.*, 21, 2125–2147, <https://doi.org/10.5194/acp-21-2125-2021>, 2021.

1980 Warneke, C., van der Veen, C., Luxembourg, S., de Gouw, J.A., Kok A.: Measurements of benzene and toluene  
1981 in ambient air using proton-transfer-reaction mass spectrometry: calibration, humidity dependence, and field  
1982 intercomparison, *International Journal of Mass Spectrometry*, Volume 207, Issue 3, doi.org/10.1016/S1387-  
1983 3806(01)00366-9, 2001.

1984 Warneke, C., McKeen, S. A., de Gouw, J. A., Goldan, P. D., Kuster, W. C., Holloway, J. S., Williams, E. J.,  
1985 Lerner, B. M., Parrish, D. D., Trainer, M., Fehsenfeld, F. C., Kato, S., Atlas, E. L, Baker, A, and Blak, D. R.:  
1986 Determination of urban volatile organic compound emission ratios and comparison with an emissions database,  
1987 *J. Geophys. Res.*, 112, D10S47, doi:10.1029/2006JD007930, 2007.

1988 Warneke, C., Froyd, K. D., Brioude, J., Bahreini, R., Brock, C. A., Cozic, J. , de Gouw, J. A., Fahey, D. W.,  
1989 Ferrare, R., Holloway, J. S., Middlebrook, A. M., Miller, L., Montzka, S., Schwarz, J. P., Sodemann, H.,  
1990 Spackman, J. R., and Stohl, A.: An important contribution to springtime Arctic aerosol from biomass burning in  
1991 Russia, *Geophys. Res. Lett.*, 37, L01801, doi:10.1029/2009GL041816, 2010.

1992 Wendisch, M., et al.: The ACRIDICON-CHUVA campaign: Studying tropical deep convective clouds and  
1993 precipitation over Amazonia using the new German research aircraft HALO, *Bull. Amer. Meteorol. Soc.*, 97,  
1994 1885-1908, doi: 10.1175/BAMS-D-14-00255, 2016.

1995 Wennberg, P. O., Bates, K. H., Crounse, J. D., Dodson, L. G., Mc-Vay, R. C., Mertens, L. A., Nguyen, T. B.,  
1996 Praske, E., Schwantes, R. H., Smarte, M. D., St Clair, J. M., Teng, A. P., Zhang, X., and Seinfeld, J. H.: Gas-  
1997 Phase Reactions of Isoprene and Its Major Oxidation Products, *Chem. Rev.*, 118, 3337–3390,  
1998 doi:10.1021/acs.chemrev.7b00439, 2018.

1999 Winkler J., Blank, P., Glaser, K., Gomes, J.A.G., Habram, M., Jambert, C., Jaeschke, W., Konrad, S.,  
2000 Kurtenbach, R., Lenschow, P., Lörzer, J.C., Perros, P.E., Pesch, M., Prümke, H.J., Rappenglück, B., Schmitz,  
2001 Th., Slemr, F., Volz-Thomas, A., and Wickert, B.: Ground-Based and Airborne Measurements of Nonmethane  
2002 Hydrocarbons in BERLIOZ: Analysis and Selected Results, *Journal of Atmospheric Chemistry* 42: 465–492,  
2003 2002.

2004 Wintel, J., Hösen, E., Koppmann, R., Krebsbach, M., Hofzumahaus, A., and Rohrer, F.: Stable carbon isotope  
2005 ratios of toluene in the boundary layer and the lower free troposphere, *Atmos. Chem. Phys.*, 13, 11059–11071,  
2006 doi:10.5194/acp-13-11059-2013, 2013.

2007 World Health Organization (WHO), Review of evidence on health aspects of air pollution – REVIHAPP Project.  
2008 WHO Regional Office for Europe, Copenhagen, Denmark, 2013.

2009 Zahn, A., Weppner, J., Widmann, H., Schlote-Holubek, K., Burger, B., Kühner, T., Franke, H.: A fast and  
2010 precise chemiluminescence ozone detector for eddy flux and airborne application, *Atmos. Meas. Tech.*, 5 (2),  
2011 363–375. doi:10.5194/amt-5-363-2012, 2012.

2012 Zhang, Y. H., Su, H., Zhong, L. J., Cheng, Y. F., Zeng, L. M., Wang, X. S., Xiang, Y. R., Wang, J. L., Gao, D.  
2013 F., Shao, M., Fan, S. J., and Liu, S. C.: Regional ozone pollution and observation-based approach for analyzing  
2014 ozone–precursor relationship during the PRIDE-PRD2004 campaign, *Atmos. Environ.*, 42, 6203–6218,  
2015 <https://doi.org/10.1016/j.atmosenv.2008.05.002>, 2008.

2016 Zhu, T., Melamed, M., Parrish, D. Gauss, M., Gallardo Klenner, L., Lawrence, M., Konare, A. and Liousse, C.:  
2017 Impacts of Megacities on air pollution and climate, WMO/ IGAC, GAW Report No.205, 2012.

2018 Ziereis, H., Minikin, A., Schlager, H., Gayet, J.F., Auriol, F., Stock, P., Baehr, J., Petzold, A., Schumann, U.,  
2019 Weinheimer, A., Ridley, B., and Ström, J.: Uptake of reactive nitrogen on cirrus cloud particles during INCA,  
2020 *Geophys. Res. Lett.*, 31(5), 2004.

2021 Zimnoch, M., Necki, J., Chmura, L., Jasek, A., Jelen, D., Galkowski, M., Kuc, T., Gorczyca, Z., Bartyzel, J., and  
2022 Rozanski, K.: Quantification of carbon dioxide and methane emissions in urban areas: Source apportionment  
2023 based on atmospheric observations, *Mitig Adapt Strateg Glob Change*, 24 (6), 1051–1071. DOI:  
2024 10.1007/s11027-018-9821-0, 2019.